Multi-Objective Trajectory Optimization for a Scaled Vehicle

How drifting improves the vehicle maneuverability in a dynamic cornering scenario.

M.D. Goldschmeding

Master of Science Thesis

TU Delft Delft University of Technology

Delft Center for Systems and Control

Multi-Objective Trajectory Optimization for a Scaled Vehicle

How drifting improves the vehicle maneuverability in a dynamic cornering scenario.

Master of Science Thesis

For the degree of Master of Science in Systems and Control
at Delft University of Technology

Marcel Dirk Goldschmeding

September 10, 2019

Faculty of Mechanical, Maritime and Materials Engineering (3mE)
Delft University of Technology

POLITECNICO
MILANO 1863

The work in this thesis was supported by Politecnico di Milano. Their cooperation is hereby gratefully acknowledged.

TU Delft Delft University of Technology

DCSC

Delft University of Technology
Department of
Delft Center for Systems and Control (dcsc)

The undersigned hereby certify that they have read and recommend to the Faculty of Mechanical, Maritime and Materials Engineering (3mE) for acceptance a thesis entitled

Multi-Objective Trajectory Optimization for a Scaled Vehicle

by

M.D. Goldschmeding

in partial fulfillment of the requirements for the degree of

Master of Science Systems and Control

Dated: September 10, 2019

Supervisor(s):

prof.dr.ir. J. Hellendoorn

prof.dr. M. Corno

Reader(s):

dr. R. Ferrari

dr. L. Ferranti

Y. Zheng MSc.

Abstract

The introduction of control systems in the automotive industry has significantly increased safety. Improved control over the vehicle dynamics has been shown to contribute to substantial reductions in the number of deaths and serious injuries resulting from road traffic crashes [41]. The introduction of Electronic Stability Control (ESC) yielded impressive improvement in vehicle stability. A meta-analysis revealed that a 49% reduction of single-vehicle accidents is realized [13]. Recent research continues the development of a fully autonomously operating vehicle. The vehicle requires the ability to operate in all situations safely, in order to reach the highest level of automation. Vehicle performance should be guaranteed within, at and beyond the limits of friction. Previous research revealed that the unstable drift motion could enlarge the operating envelope of a vehicle. An extensive amount of research is dedicated to controlling a drift. The results show that control systems are increasingly capable of stabilizing a steady-state cornering scenario. The main limitation of these studies is that only a portion of the vehicle motion that is observed in reality can be considered to be steady-state motion.

This thesis presents a multi-objective trajectory optimization which extends the steady-state analysis to a dynamic driving scenario. Based on experimental data obtained with a 1:10 scaled vehicle, accurate vehicle and tire models are derived. It is validated that the models closely mimic the dynamics of the scaled vehicle. In order to justify the use of drifting, the differences between stable and unstable driving equilibria are studied. The stability and controllability are assessed through the construction of the phase portraits and the computation of the Controllability Grammian. The findings, obtained under the assumption of steady-state conditions, are then validated in the dynamic driving scenario. A two-step optimization approach is presented. Spline optimization based on a simplified model is used to obtain initial conditions for a high fidelity model-based optimization. The scope is limited to a single corner, which is optimized under varying velocities and friction conditions.

Under the assumption of steady-state conditions, it is found that the drift motion imposes various benefits over normal driving. Higher cornering velocities and therewith yaw rates can be achieved in a drift. Besides, the principles of tire saturation and force coupling allow for controlling the lateral and yaw dynamics of the vehicle through the rear longitudinal tire force. This increases the maneuverability of the vehicle. The results of the dynamic optimization

extend the findings of the steady-state analysis. In the dynamic maneuvers, drifting is found to improve vehicle maneuverability at high velocities and in scenarios of low friction. The approach presented in this work forms a basis for studying the effects that drifting could have on vehicle motion in reality. The relevant aspects of vehicle motion are translated into a multi-objective optimization. The methods that are developed in this work release the simplifying assumption of steady-state driving conditions. As a result, the drift motion can be studied in a more realistic driving scenario. It is expected that through further improving the optimization algorithm, the full operation envelope of the vehicle can be explored.

Table of Contents

List of Figures

List of Tables

Preface

The completion of this research marks the end of an extraordinary period. Looking back, I have encountered many challenges, which were not all related to the thesis. It has been a unique experience from which I learned a lot.

I am grateful for the possibility of carrying out this specific research. It provided me with the opportunity to combine two subjects that have always fascinated me; cars and engineering. The fact that a part of the work could be done at the Politecnico di Milano made it into an unforgettable project.

First of all, I would like to thank Matteo Corno for supervising me over the past months. I have been inspired by his critical and rational view. I highly appreciated the fact that he was always available to discuss what was on my mind.

This project would not be possible without Hans Hellendoorn. I want to thank him for the opportunity to go abroad and represent the Delft University of Technology. Furthermore, I appreciate the open conversations we had about the challenges I was facing.

Then there are the people that helped me to complete this journey. I want to thank my parents for always supporting me and believing in me. Thanks to my sister Marije, for the numerous times that you welcomed me with a cup of coffee, cooked dinner for me, and let me work at your dinner table. Furthermore, I want to thank Valerie, who realized how important this project was to me and who did anything to support me. Special appreciation for my friends. You made this period of hard-working a lot more joyful. Last but not least, a special thanks to Marianne, who was always willing to read the sections I wrote and returned so much valuable feedback.

This thesis is dedicated to my father, who's unremitting perseverance has been an unique inspiration to me.

Chapter 1

Introduction

1-1 Project Context

Over the past decades, driver assistance systems helped to increase vehicle control and therewith reduce the number of traffic accidents. Technological advances in the automotive industry have led to an increase in the use of automation in human-controlled vehicles. The world is gradually preparing for fully autonomous vehicles. Numerous control systems have been developed and implemented in road cars. Early examples are Anti-Lock Brakes (ABS) and Electronic Stability Program (ESP). More recently, road cars have been more frequently equipped with Active Cruise Control (ACC) and lane-keeping systems. In 2014, the Society of Automotive Engineers (SAE) introduced a method to score vehicles (and the control systems) based on levels of autonomous driving, on a scale from 0 to 5 [30]. The extent to which an autonomous driving system performs the driving task determines the level of automation. The highest level describes a situation of full driving automation, in which vehicles will operate without any interference of a human driver. For now, this view of mobility remains a future perspective. Most modern production vehicles show the ability to reach SAE automation level 3 or 4. Although the autonomous driving systems can perform the driving task, the interference of a human driver is still required in cases of emergency. Besides, in some cases, the use of these systems is restricted to motorways only.

Another essential aspect to consider in the transition towards full autonomous mobility is the road infrastructure. The construction of roads in civilized areas expanded rapidly over the past century. People are used to the reality that for almost any destination, there is a road that leads there. However, there remain rural areas where almost no infrastructure is present. In order to reach the level of fully autonomous mobility, the vehicle needs to be capable of driving on varying road surfaces. Besides high friction surface such as asphalt, also terrains that offer less friction needs to be considered. Previous studies have explored the effect of the type of terrain on the vehicle dynamics [34]. The analysis is based on the relative angle between the heading of the vehicle and the direction of the resultant velocity vector. This so-called side-slip angle can be computed from the longitudinal (V_x) and lateral velocity (V_y) of the vehicle (1-1).

$$\beta = \tan^{-1}\left(\frac{V_y}{V_x}\right) \tag{1-1}$$

The side-slip angle indicates to which degree the vehicle is sliding. When driving through a corner at a high friction surface such as asphalt, positive side-slip angles (Figure 1-1a) or angles close to zero are observed (Figure 1-1b). When driving on a low-friction surface, the maneuver is characterized by negative side-slip angles (Figure 1-1a). This type of maneuvering is called drifting (Figure 1-1c).

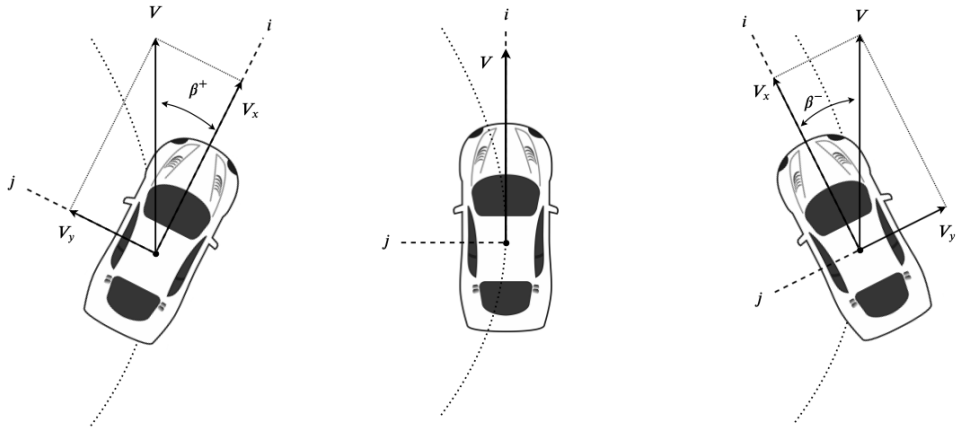

(a) $\beta > 0$ **(b)** $\beta = 0$ **(c)** $\beta < 0$

Figure 1-1: Comparison of different types of vehicle motion based on the side-slip angle β.

Classical vehicle stability systems such as ESP are based on the concept of controlling the vehicle through minimizing the side-slip angle [4]. These systems are typically designed for high-grip surfaces. The application in off-road conditions leads to unsatisfactory results [22]. The assumption of pure longitudinal motion (without sliding) limits the applicability of current stability systems on low friction surfaces. In order to achieve maximum vehicle controllability, future autonomous driving systems need to be developed with the ability to control the vehicle under non-ideal and varying grip conditions through stabilization of large side-slip angles [21]. This includes drifting, a topic that has increasingly been studied over the past decades.

Research into the nature of the drift motion yielded promising advantages on vehicle maneuverability. As part of a study revolving around the usability of a drift control as an Advanced Driver Assitance System (ADAS), Acosta *et al.* made a comparison between a drift control ADAS and a low side-slip stability control system [2]. It is concluded that corners can be negotiated at a higher velocity while drifting. The fact that high cornering velocities are associated with large side-slip angles was previously observed by Velenis *et al.* [40]. Besides, it was found that higher yaw rates can be generated [3]. A study based on the centripetal acceleration, the acceleration towards the center of the corner, was presented in [38]. Especially for small cornering radii, centripetal acceleration increases significantly with increasing side-slip angle. Consequently, large side-slip maneuvering has the potential to negotiate a corner at smaller radii. It is concluded that drifting allows to operate the vehicle at the limits of the operating envelope.

Most of the aforementioned studies rely on the assumption of steady-state conditions. The longitudinal, the lateral, and the yaw acceleration are considered to be zero, resulting in steady-state motion. In reality, it is challenging to maintain steady-state motion, as the forces acting on the vehicle are continuously varying. Less is known about the advantages of drift maneuvers when the assumption of steady-state conditions is released.

The purpose of this thesis is to study the drift motion in a dynamical cornering situation. Through trajectory optimization under varying conditions, it is investigated how negative side-slip motion can be used to improve vehicle maneuverability. The dynamic cornering scenario is written into a multi-objective trajectory optimization. The cost-function terms are chosen and weighted such that the dynamic motion resembles the steady-state equilibria as close as possible. The aim of this approach is to bridge the gap between the available knowledge (obtained under steady-state conditions) and the real-life driving scenarios. In doing so, this work attempts to take a step towards the implementation of drift control in production vehicles and therewith towards fully autonomous vehicles.

1-2 Research Questions

This thesis explores whether the steady-state benefits of drifting becomes apparent in a dynamical driving scenario. Based on this goal, three research questions are formulated.

1. What are the modeling requirements to describe the drift maneuver accurately?
2. What are the advantages of drift equilibria compared to normal driving under the assumption of steady-state conditions?
3. What are the advantages of the drift motion in a dynamic driving scenario, when the assumption of steady-state cornering conditions is released?

By answering the research questions, it is expected that the author can conclude on the benefits of drifting and that recommendations for further research can be formulated.

1-3 Project Goals

The research questions are translated into project goals to create a guideline for the activities to be performed in this thesis work.

1. Define a model that accurately can describe the drift motion.
2. Identify and validate the unknown model parameters based on the available experimental data.
3. Compute the system equilibria and perform an analysis of the stability and controllability.
4. Design a dynamic driving scenario and translate this into a multi-objective trajectory optimization.

5. Execute the trajectory optimization for different cornering velocities and under varying friction.

1-4 Project Boundaries

In order to correctly interpret the results in this work, it is vital to define the scope of the project clearly. This section briefly discusses the relevant boundaries that are considered.

Forces acting on the vehicle
In the field of vehicle dynamics, various forces that act on the moving vehicle can be taken into account. It is essential to define the boundaries clearly. This work focuses on the forces that are generated at the tires and how these forces influence the dynamics of the vehicle.

Impact on the human driver
One of the first questions that come to mind when thinking about the drift motion is: what would the impact be on a human driver. For example, would the physical impact on the human body cause motion sickness? Another critical question is how a human driver can be informed and prepared for a drift that is about to be initiated by the control system. Both aspects are relevant when considering the implementation of drift control. At the same time, it is strongly associated with the currently existing view on vehicle mobility. By the time that autonomous driving is fully embedded in our daily life, vehicles transporting anything other than persons might not include a driver at all. The implementation of a drift control system, however, is out of the scope of this research. The effect that the drift motion could have on a human body will not be addressed in this work.

Road infrastructure
Drifting on a public road seems unrealistic. The current road infrastructure is characterized by tight lanes and sometimes two-way roads. However, consider the idea that the road infrastructure could significantly change, only structuring traffic in the city but allowing a vehicle to navigate freely in rural areas. Under varying friction coefficients, the vehicle then needs to plan the trajectory, possibly not limited by road boundaries.

Reduced scale
As will be discussed in the following chapters, the analysis of this work focuses on a small-scaled vehicle. The direct applications of methods that are derived for scaled vehicles on full-size vehicles can be subjected to issues due to scaling effects. A study into the scaling effect is not included and is left for further research.

1-5 Report Structure

The thesis is structured in the following way. Chapter 2 discusses the models that are used to describe the dynamics of the vehicle and the tires. Preprocessing of the experimental data is discussed in chapter 3. The process of parameter identification is described in chapter 4. Chapter 5 contains a steady-state analysis of vehicle motion. It explains system equilibria and therewith analyzes the unstable nature of the drift motion. Then, the assumption of steady-state conditions is released. Chapter 6 present a dynamic driving scenario and explains how it is formulated as an optimization problem. The optimization algorithm is discussed in the

following two chapters. The method that is used to initialize the search based on spline optimization is presented in chapter 7. The simulation-based optimization of the driving scenario is included in chapter 8. The thesis ends with the conclusions in chapter 9 and the recommendations in chapter 10.

At the end of the thesis, appendices are included that contain material that is not directly discussed in the thesis, but that provides relevant background or additional insights.

1-6 Politecnico di Milano

This thesis is performed as part of a collaboration between the Delft University of Technology and the Politecnico di Milano. As a result of this cooperation, research has been carried out at the Dipartimento di Elettronica, Informazione e Bioingegneria. This department is involved in research in various fields related to control system science and engineering, industrial automation, robotics, systems theory, environmental systems, ecology, and operations research.

Chapter 2

Modeling

The introduction of this work (Chapter 1) stated the relevance of obtaining a deeper understanding of the effect that the drift motion has on vehicle maneuverability. A common approach to study the dynamic behavior of a vehicle is to define a model that describes the dynamics. The system of interest is written in mathematical form, the model, which can then be used for computation or simulation. In this way, time and money can be saved since the experiments are not executed with the real system. In the ideal world, one can construct a model that describes the vehicle without any simplification. The model, in this case, would be a perfect mathematical description of the real vehicle. In reality, however, this is not possible and not needed. Such a model would be too large, using the model for simulations would require too much computational power. Assumptions are made to build a model that is detailed enough to describe the dominant dynamics of the vehicle while having a minimal computational load. This chapter addresses this issue and elaborates on the modeling choices that have been made.

Before discussing the models that are used in this work, section 2-1 provides an overview of relevant reference frames. Section 2-2 revolves around tire modelling. Section 2-3 continues with an explanation of the vehicle model. Finally, conclusions are drawn in section 2-4.

2-1 Reference Systems

In this work, two different reference frames will be used; both are displayed in Figure 2-1. The inertial reference frame defines the motion of the vehicle in terms of the fixed coordinate frame ($x_{inertial}$, $y_{inertial}$). The velocities in each direction are denoted by $V_{x,inertial}$ and $V_{y,inertial}$, respectively. The body orientated frame considers the center of the vehicle as the origin, with the x-axis belonging the longitudinal direction and the y-axis to the lateral direction of the vehicle. The velocities are defined as u and v. The angle between the inertial and body orientated reference frame is denoted by ψ. For a heading angle ψ equal to zero, the longitudinal axis x is parallel to the inertial axis $x_{inertial}$.

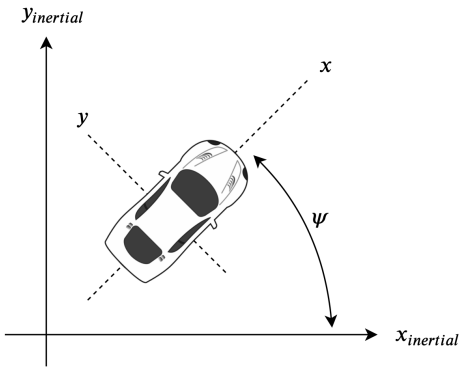

Figure 2-1: Schematic representation of the inertial and the body-orientated reference frame.

The dynamics of the vehicle expressed in the body orientated coordinate frame can be written into the inertial reference frame using the equations below.

$$V_{inertial,x} = \quad u\cos(\psi) - v\sin(\psi) \tag{2-1}$$
$$V_{inertial,y} = \quad u\sin(\psi) + v\cos(\psi) \tag{2-2}$$

The resultant velocity of the vehicle V will be equal for both reference frames.

$$V = \sqrt{V_x^2 + V_y^2} = \sqrt{u^2 + v^2} \tag{2-3}$$

In the remainder of the thesis, the notation $x_{inertial}$ and $y_{inertial}$ is used to indicate the position of the vehicle in the inertial frame. Without any further specification, the symbols x and y are used to indicate the longitudinal and lateral direction of the vehicle or the tire.

2-2 Tire Modeling

Vehicles can follow a trajectory due to the forces generated between the tires and the road surface. In the absence of tire forces, one is not able to change the motion of any vehicle. Similar conclusions can be derived from Newton's second law of motion. The forces acting on a body, divided by the mass, equal the acceleration exerted on the body. Studying the generation of tire forces thus is the starting point for modeling the dynamics of the vehicle.

In the literature, wheel moments are often neglected, and the dynamics of the tire are described only by the forces acting on the wheel. Nguyen *et al.* [26] provided a mathematical representation (2-4). The total tire force F_{wheel}, is considered to be a function of four variables: the tire-road friction coefficient μ, the slip angle α, the longitudinal slip ratio λ and the normal load on the tire F_z.

$$F_{wheel} = f\Big(\mu, \alpha, \lambda, F_z\Big) \tag{2-4}$$

The longitudinal slip ratio (or slip ratio) represents the relative motion of the tire and the ground (2-5). Longitudinal slip is generated when the translational and radial velocities are unequal. The lateral slip angle (or slip angle) is defined as the tangent of the ratio between the lateral and longitudinal tire velocity (2-6). To clarify the concepts of tire slip, a schematic representation of longitudinal and lateral slip is displayed in Figure 2-2a and Figure 2-2b. Here, r_{wheel} represents the wheel radius, ω_{wheel} is the angular wheel velocity, $V_{x,wheel}$ is the longitudinal velocity of the wheel and $V_{y,wheel}$ is the velocity in the lateral direction.

$$\lambda = \frac{\left|r_{wheel}\cdot\omega_{wheel} - V_{x,wheel}\right|}{\max(r_{wheel}\cdot\omega, V_{x,wheel})} \tag{2-5}$$

$$\alpha = \tan^{-1}\left(\frac{V_{y,wheel}}{V_{x,wheel}}\right) \tag{2-6}$$

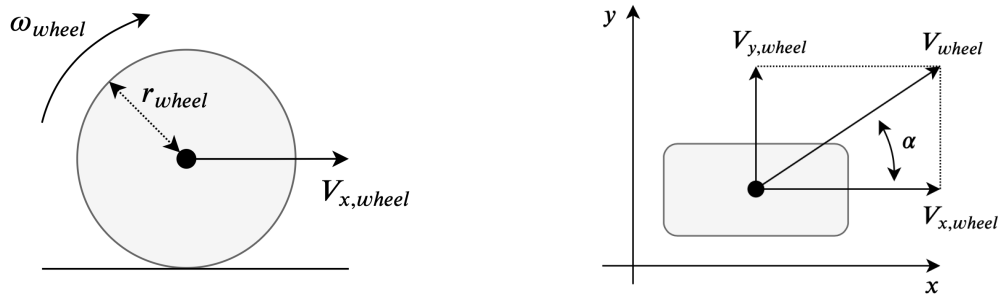

(a) Side view **(b)** Top view

Figure 2-2: Schematic representation of a single tire to clarify the principles of longitudinal slip ratio λ and lateral slip angle α.

Equation 2-4 provides an expression for the resultant tire forces. It is often more convenient to split the resultant force and consider the acting forces along the longitudinal and lateral direction. Consider the left graph of Figure 2-3, which envisages the lateral tire dynamics. The lateral force F_y is plotted against the slip angle α. The first observation from the curve is that lateral forces are only generated for non-zero slip angles. A linear region can be identified, up to approximately 8°, in which an increase in slip angle results in a proportional increase in lateral tire force. This relationship no longer holds for high slip values; in this region, the tire is considered to be saturated. The different lines correspond to a different value of the longitudinal slip ratio, in the graph denoted as brake slip κ instead of the conventional notation λ. It is observed that increased slip ratio's yield lower side forces, over the complete range of lateral slip angles. This effect is known as force coupling. It is caused by the fact that the friction available from the road surface is limited. There is a maximum amount of tire force that can be generated. Longitudinal slip results in longitudinal tire force, therewith decreasing the maximum attainable side force of the tire.

The observations of the lateral tire dynamics also apply to the behavior in the longitudinal direction, displayed in the middle graph of Figure 2-3. The longitudinal force depends mainly on the slip ratio κ and through force coupling also on the slip angle α. The right graph shows a quarter of the so-called friction ellipse. This is a graphical representation of the maximum longitudinal and lateral tire forces that can be obtained under a particular operating condition.

The conditions are expressed in terms of the directional slip values, the pair (κ, α). In the graph, only the effect of the latter is displayed. In the remainder of this work, the longitudinal slip is denoted by λ.

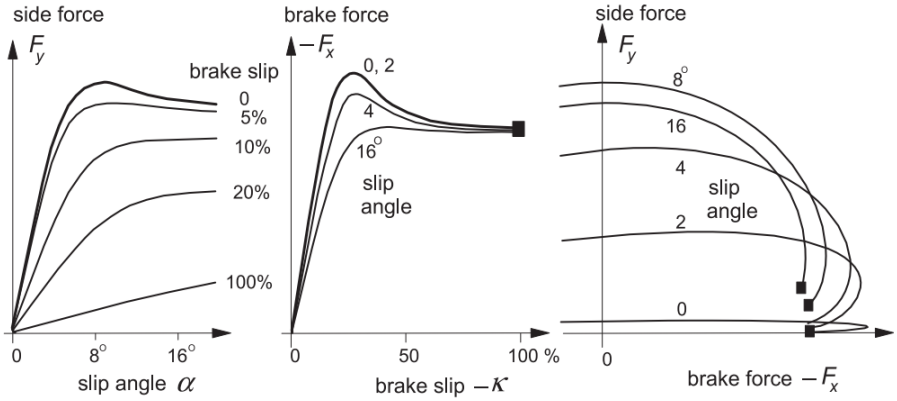

Figure 2-3: Tire characteristics under combined slip conditions. Left graph: lateral tire dynamics, F_y against α. Middle graph: longitudinal tire dynamics, F_x against λ. Right graph: portion of the friction ellipse, F_y versus F_x for different slip angles [27].

It is essential to know the forces that act on a tire in order to control the dynamics of a vehicle [1]. Forces and moments from the road act on each tire and strongly influence the dynamics of the vehicle [29]. A typical tire is not a rigid structure. It deforms during operation, and because of that, the contact patch with the road changes [33]. Within the limits of handling, the longitudinal and lateral tire forces have been proved to be proportional to respectively the slip ratio and the slip angle. However, at and beyond the limits of handling this relationship becomes nonlinear. This makes it challenging to model tire-road interaction. The methods proposed in the literature can be divided into two groups: analytic and empirical models.

Analytic tire modeling aims to understand and describe the physical mechanism that is generating the tire forces. The force generation remains a challenging subject. Different concepts describe this phenomenon, for which each analytic tire model comes with different expressions. Examples of analytic tire models that are applied in recent studies are the Fiala Tire Model [20], the Dugoff Tire Model [10, 11], or the LuGre Tire Model [39, 42]. Empiric tire models differ from the analytic approaches as these models do not try to include or describe the physical phenomena behind tire dynamics. Empiric expressions for tire forces often result from attempts of curve fitting or regression. The most common empiric tire model is the Magic Formula which describes tire behavior by fitting a polynomial to experimental data [27].

It is evident that tire models are a necessity for studying vehicle dynamics. The main issue is which one to choose. For studying cases of pure longitudinal and lateral force generation, the analytic models are intuitive and appear to be quite realistic [29]. The Dugoff Model and the Magic Formula are among the most commonly used models in the literature. Both models have been compared [7, 8], and the force estimations are found to be quick and close to experimental data. Simulations are performed under longitudinal, lateral, and combined slip conditions. The Magic Formula yielded slightly more accurate results, at the cost of an

increased computational load. Both models are found to be valid for vehicle dynamics analysis and simulation. The Dugoff Model is selected in this work since it has fewer parameters to estimate. Besides, the fact that the model is derived from the physics behind the tire-road interaction is expected to make it more intuitive to adjust the model to get a closer match with the validation data.

The Dugoff model provides for the calculation of forces under combined lateral and longitudinal tire force generation. It assumes a uniform vertical pressure distribution on the tire's contact patch [29]. The longitudinal and lateral tire forces are, according to the first publication [10], described as:

$$F_x = C_\lambda \frac{\lambda}{1+\lambda} f(\zeta), \tag{2-7}$$

$$F_y = C_\alpha \frac{\tan(\alpha)}{1+\lambda} f(\zeta), \tag{2-8}$$

$$f(\zeta) = \begin{cases} (2-\zeta)\zeta & \text{, if } \zeta < 1 \\ 1 & \text{, if } \zeta \leq 1 \end{cases}, \tag{2-9}$$

$$\zeta = \frac{\mu_{max} F_z (1+\lambda)}{2\sqrt{(C_\lambda \lambda)^2 + (C_\alpha \tan\alpha)^2}}. \tag{2-10}$$

Where C_λ and C_α are the longitudinal and lateral cornering stiffness, respectively. The slip ratio is denoted as λ, α is the slip angle, μ the friction coefficient, and F_z represents the normal load on the tire. The function $f(\zeta)$ accounts for the effect of force coupling, based on the normal load on the tire and the slip conditions.

2-3 Vehicle Modeling

Vehicle models are used to describe the motion that results from system inputs. The physical meaning of these inputs may differ. In general, the inputs affect the heading and the velocity of the vehicle. The available vehicle models can be categorized into two groups, kinematic and dynamic models. Both approaches are discussed in this section.

2-3-1 Kinematic Approach

Kinematic vehicle models are purely based on the position and velocity of the systems without considering the forces and moments that cause them [29]. Under the assumption of planar motion, the motion of a vehicle can be described by the position in two directions together with the heading. Figure 2-4 shows a schematic representation. In this specific figure, the inertial coordinate frame is denoted by (X, Y). Although both wheels are steered in this example, this report limits the analysis to front-wheel steering only. A crucial assumption of the kinematic model is the absence of wheel slip. This allows for deriving the equations of motions from geometrical relationships. A reference point on the vehicle needs to be selected, for example, the center of the front or rear axle. Based on this reference point, the kinematics are described. In this case, the Center of Gravity (COG) is selected. The position and heading of this point with respect to a fixed coordinate frame now describe the motion (2-11).

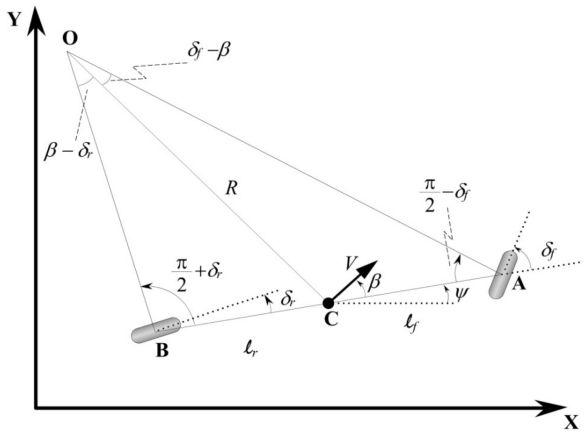

Figure 2-4: Schematic representation of the kinematic vehicle model, expressed in the inertial reference frame [29].

$$\dot{x} = V\cos(\psi+\beta) \tag{2-11}$$

$$\dot{y} = V\sin(\psi+\beta) \tag{2-12}$$

$$\dot{\psi} = \frac{V\cos(\beta)}{l_F+l_R}\tan\Big(\delta_f\Big) \tag{2-13}$$

$$\beta = \tan^{-1}\left(\frac{l_R\tan\delta_f}{l_F+l_R}\right) \tag{2-14}$$

Here, V is the velocity in the reference points, β is the side-slip angle, ψ is the angle between the heading of the vehicle and the fixed reference frame, δ_f is the steering angle and finally l_F and l_R represent the distances between COG and the corresponding axles.

2-3-2 Dynamic Approach

Although the kinematic model successfully describes vehicle motion, it is limited by the assumption that the wheel slip is zero. At high velocity this no longer holds, and the predicted motion becomes an inaccurate description of reality. Dynamic modeling accounts for slip conditions since it considers the forces and moments that cause the motion. Using Newton's second law of motion, accelerations in each direction of the coordinate system are calculated. Different physical models are available in the literature. Selecting an appropriate vehicle model is a trade-off between ease of computation and model fidelity. High complexity vehicle models might have the ability to describe vehicle motion more accurately. On the other hand, the time it takes to solve them increases with the complexity. This section describes two of the most common physical models: the single-track (Figure 2-5a) and double-track model (Figure 2-5b). The first is a simplification of the latter; for each axis, the wheels are lumped together.

The equations of motion belonging to the dynamic model are displayed in (2-15), (2-16) and (2-17). The dynamics are expressed in terms of the longitudinal velocity u, the lateral velocity v and the yaw rate r. The latter is the time derivative of the heading angle ψ. The directional accelerations are a function of the acting tire forces and the steering angle δ. Furthermore, m

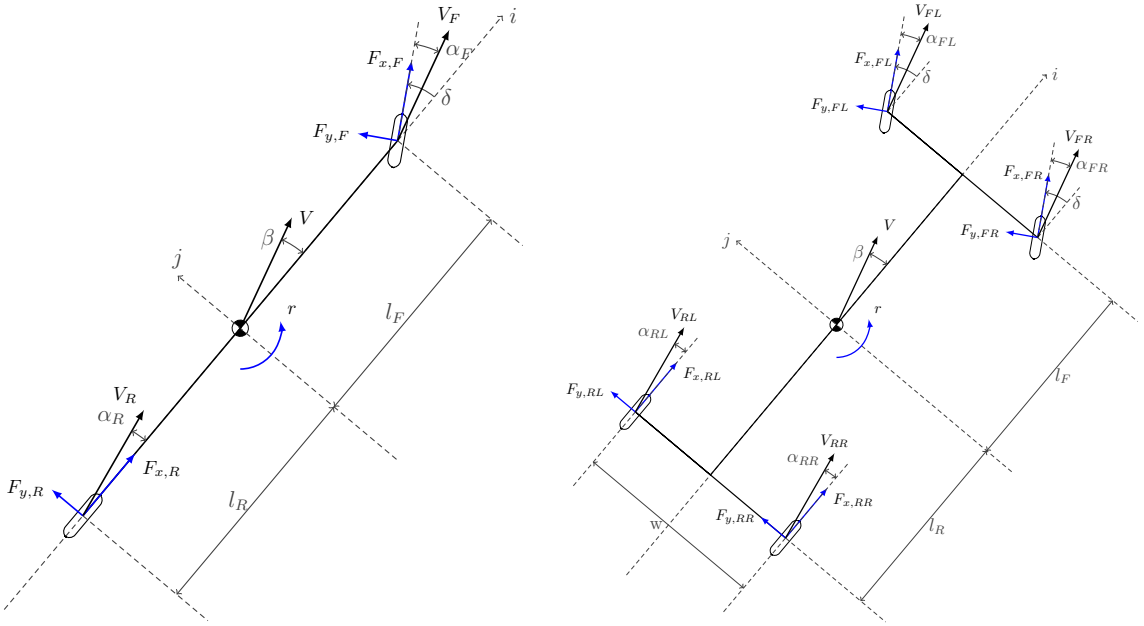

(a) The single-track Model **(b)** The double-track Model

Figure 2-5: Overview of the most common physical vehicle representations in the body orientated frame.

is the mass of the vehicle, I_z is the yaw inertia. In the expression of the yaw dynamics (2-17), $\sum M_z$ represents the sum of the moments acting on the COG. Since the single-track model effectively has a track width equal to zero, the sum of the moment only depend on the front ($F_{y,F}$) and rear ($F_{y,R}$) lateral forces and the distance from center of gravity to the front (l_F) and rear axle (l_R). The double-track model has track-width w. Therefore the longitudinal force of the front ($F_{x,F}$) and rear ($F_{x,R}$) tires will also appear in the expression.

$$ma_x = m\left(\dot{u} - vr\right) = \sum F_{x,F}\cos\delta - \sum F_{y,F}\sin\delta + \sum F_{x,R} \tag{2-15}$$

$$ma_y = m\left(\dot{v} + ur\right) = \sum F_{x,F}\sin\delta + \sum F_{y,F}\cos\delta + \sum F_{y,R} \tag{2-16}$$

$$I_z\dot{r} = \sum M_z \tag{2-17}$$

Although the double-track model provides a more accurate description of the vehicle dynamics, the increased complexity makes it less suitable for optimization purposes. Therefore, most studies rely on the single-track model for control design.

When considering a suitable vehicle model to study autonomous drifting, it is essential that the model can account for wheel slip. This makes the kinematic model less favorable, shifting the preference towards a physical model. The primary consideration in choosing between either the single-track model or the double-track model is the computational load. The goal of this thesis is to study the behavior of a vehicle along a curved trajectory. Simulations will be executed to optimize the path of the vehicle. In an attempt to reduce the required solving time, the single-track model will be selected. The single-track model is described by the states: the longitudinal velocity u, the lateral velocity v and the yaw rate r. The state derivatives are described as:

$$\dot{u} = \frac{1}{m}\left(-2F_{y,F}\sin\delta + 2F_{x,R}\right) + vr, \tag{2-18}$$
$$\dot{v} = \frac{1}{m}\left(2F_{y,F}\cos\delta + 2F_{y,R}\right) - ur, \tag{2-19}$$
$$\dot{r} = \frac{1}{I_z}\left(2l_F F_{y,F}\cos\delta - 2l_R F_{y,R}\right). \tag{2-20}$$

The single-track model can be simplified by assuming that the steering angle δ is significantly small to approximate $\cos\delta \approx 1$ and $\sin\delta \approx 0$. This assumption impacts the expression of the single-track model in two ways. The longitudinal component of the front lateral tire force is no longer affecting the longitudinal dynamics (2-21). Furthermore, the front tire lateral force is not decreases as of the steering angle becomes larger (2-22), (2-23).

$$\dot{u} = \frac{1}{m}\left(2F_{x,R}\right) + vr \tag{2-21}$$
$$\dot{v} = \frac{1}{m}\left(2F_{y,F} + 2F_{y,R}\right) - ur \tag{2-22}$$
$$\dot{r} = \frac{1}{I_z}\left(2l_F F_{y,F} - 2l_R F_{y,R}\right) \tag{2-23}$$

The introduction explained that different types of vehicle motion can be expressed by the side-slip angle β. In order to differentiate based on the side-slip angle, the state derivatives can be rewritten such that β becomes one of the states [19].

$$\dot{u} = \frac{1}{m}\left(2F_{x,R}\right) + ru\beta \tag{2-24}$$
$$\dot{\beta} = \frac{1}{mu}\left(2F_{y,F} + 2F_{y,R}\right) - r \tag{2-25}$$
$$\dot{r} = \frac{1}{I}\left(2l_F F_{y,F} - 2l_R F_{y,R}\right) \tag{2-26}$$

Again, these expressions are based on the approximation that the steering and side-slip angles are significantly small to assume $\cos(\delta) \approx 1$, $\beta \approx v/u$ and $\dot{\beta} \approx \dot{v}/u$. Hindiyeh *et al.* computed that the small side-slip angle assumption introduces an 4.3% error for $|\beta| \leq 0.35$ rad, for steering angles $|\delta| \leq 0.4$ rad an 8.6% error is obtained [19]. It is concluded that the error is significantly small to justify the use of the single-track model that are derived under the assumption. When the single-track model is used in the following chapters, there will be a reference to this chapter to indicate with expression is considered.

Assumptions

It is already mentioned that modeling is a trade-off between accuracy and minimizing the complexity of the model. In this research, the following assumptions are made:

- *Vertical dynamics of the vehicle are neglected*
  All roads have irregularities which result in vertical movement of the vehicle. Accounting for vertical dynamics introduces complexity to the vehicle model, making it potentially more difficult to solve the optimization. Although vertical motion could influence the normal tire load and therewith the friction limits, it is considered to be out of the scope of this research.

- *Load transfer is neglected*
  The maximum force that can be generated at each wheel depends on the acting normal load. Load transfer due to vehicle dynamics could increase and decrease these normal loads. It is assumed that load transfer changes the time instance at which the tires reach the saturation limit, but that it does not fundamentally change the maneuver itself.

- *Motor dynamics are neglected*
  In this work, the rear longitudinal tire force is considered to be one of the inputs. This implies that motor dynamics are not included. For implementation purposes, the torque supplied by the motor would be a convenient input. However, since this work focuses mainly on lateral dynamics, it is assumed that the longitudinal tire force can be controlled directly.

2-4 Conclusions

This chapter provides an overview of the existing modeling approaches relating to vehicle dynamics. The aim was to assess the available vehicle and tire models. There exists a trade-off between model complexity and accuracy. The goal is to find the simplest model that can describe all relevant dynamics. Based on the analysis in this chapter, the main conclusions are listed below.

- The Dugoff tire model was selected since it accounts for tire saturation and force coupling while offering low computational load.
- The single-track model is preferred over the double-track model. Although the latter is a more accurate description of reality, the single-track model is capable of describing relevant vehicle dynamics. The reduced computation time due to the lower model complexity outweighs the limitations of lower model fidelity.
- Assumptions are made to define the boundaries of the dynamics that are considered in this work. The vertical dynamics of the vehicle are neglected. Furthermore, load transfer is not taken into account. The rear longitudinal tire force is selected as a control input, implying that also the motor dynamics are neglected.

The selected models will be used throughout the remainder of this work. The main limitations lie in the fact that models will always be a simplification of reality. It is assumed, however, that the model fidelity is sufficiently high to study the nature of the drifting maneuver.

Chapter 3

Data Preprocessing

A set of experimental data is available from previous research. The signals describe the dynamics of the scaled-vehicle during varying maneuvers. It can be used to identify the unknown model parameters. However, it is vital to preprocess the data before proceeding to this identification step. The sensory data generally have different sampling frequencies. Furthermore, the data can be subjected to sensor noise. This chapter discusses the data that is available and explores the preprocessing that is required to prepare the data for the parameter identification.

Section 3-1 starts with a description of the data that is available from conducted experiments. The steps of filtering, re-sampling, and aligning the data signals is discussed in section 3-2. At the end of the chapter, in section 3-3, the conclusions are summarized.

3-1 Data Collection

The experimental data can be divided into two groups: signals resulting from the Motion Capture System (MCS) and signals resulting from the on-board sensors of the Berkeley Autonomous Race Car (BARC). The configuration of the BARC that was used to perform the experiments is depicted in Figure 3-1.

3-1-1 BARC Signals

Appendix A presents a schematic overview of the components that are installed on the BARC. This section discusses how the data signals are retrieved from these components. The vehicle that was available at the Politenico di Milano was equipped with an Internal Measuring Unit (IMU), two wheel encoders, and an Electronic Control Unit (ECU).

Figure 3-1: The BARC that is used to perform the experiments at the Politecnico di Milano [37].

Internal Measurement Unit

The IMU is considered to be located at to the Center of Gravity (COG) of the vehicle and provides the acceleration and angular velocity in three directions (Figure 3-2). The component consists of a triple-axis gyroscope and a triple-axis accelerometer. Since the IMU is mounted backward on the vehicle, the signals need to be converted to obtain the acceleration and angular velocities in the correct signs (3-1).

$$
\begin{aligned}
a_{x,BARC} &= -a_{x,IMU} && \text{(3-1)}\\
a_{y,BARC} &= -a_{y,IMU} && \text{(3-2)}\\
a_{z,BARC} &= a_{z,IMU} && \text{(3-3)}\\
\omega_{x,BARC} &= -\omega_{x,IMU} && \text{(3-4)}\\
\omega_{y,BARC} &= -\omega_{y,IMU} && \text{(3-5)}\\
\omega_{z,BARC} &= \omega_{z,IMU} && \text{(3-6)}\\
& && \text{(3-7)}
\end{aligned}
$$

Wheel Encoders

The wheel encoders provide information on the velocity of the wheels. Individual sensors are placed at both the front and rear axle. The sensor is constructed from placing magnets on a plastic disc that is fixed to the wheel axle. A hall effect sensor is used to check if a magnet passes by as a result on the angular wheel velocity ω_{wheel}. A schematic representation of the wheel encoder is displayed in Figure 3-3. The hall effect sensor, displayed in grey and located at the top of the disk, measures the magnetic flux density. When it is larger than the predefined threshold, the binary output signal is switched on. When the magnetic flux density falls below the threshold, the output returns to off.

The frequency of the magnets passing by can be derived from the binary Hall sensor signals. The time between two magnets, combined with the circumference of the disk, allows for computing the wheel velocity (3-8).

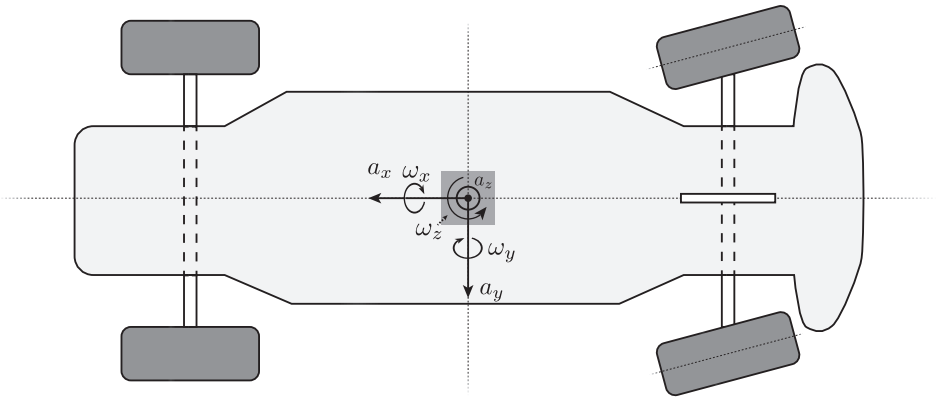

Figure 3-2: Overview of the IMU reference frame. As it is mounted backward on the scaled-vehicle, the longitudinal axis is in opposite direction [37].

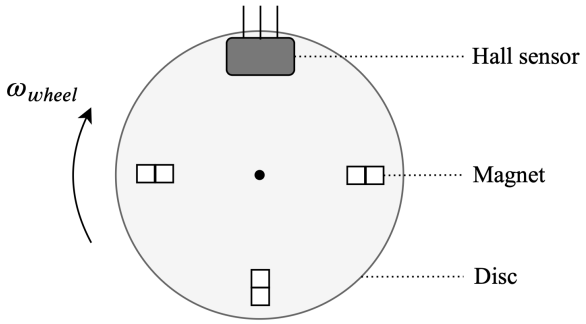

Figure 3-3: Schematic representation of the wheel encoder.

$$V_{enc,i} \approx \frac{\Delta s}{\Delta t} = \frac{2\pi r_{wheel}}{N\left(t_k - t_{k-2}\right)}, \qquad i = \{F, R\} \tag{3-8}$$

In this expression Δs is the distance between two magnets, Δt the required time to travel that distance, r_{wheel} is the wheel radius, N is the number of magnets on the disc. The hall sensor measures a difference in magnetic flux, meaning that the output is triggered when a magnet enters and leaves the proximity of the sensor. The time between two magnets is therefore defined as the difference $t_k - t_{k-2}$, where t_k denotes the time at instance k. Note that $V_{enc,i}$ denotes the velocity of the wheel and not the angular velocity ω_{wheel}.

Electronic Control Unit

The ECU provides information about the control signals that are sent to the motor and the steering servo. Although current is the direct input to the actuators, the available signals from the ECU are not. Instead, numerical signals with values between 70 and 110 are sent to the ECU. The motor controller translates the input to a pulse-width modulated signal that controls the motor power. The input of 90 corresponds to zero motor power, 70 to full backward power, 110 to maximum power in the forward direction. In case of the steering servo, a similar pulse-width modulated signal is generated. The identified neutral point of

the steering mechanism is found to correspond to an input of 90.88. Any input value smaller than the neutral point result in a left corner, larger values correspond to a right corner.

3-1-2 Motion Capture System

The MCS system returns information on the three-directional position and rotation of the vehicle. From this data also the velocity and the acceleration of the vehicle can be computed. Experiments are performed with the BARC in an arena that is equipped with multiple cameras. Each camera records the movement of the vehicle from a different angle. The cameras send infrared light to the ground, which is reflected by a set of markers on the vehicle. Based on the reflection of the markers, the cameras can locate the vehicle with 1 mm accuracy.

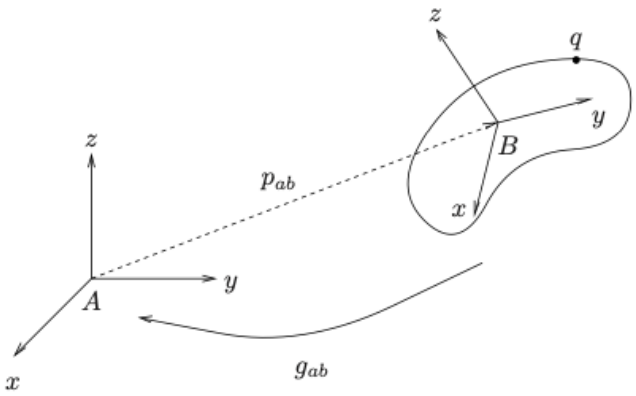

Figure 3-4: Coordinate frame transformation g_{ab} from body orientated coordinate system B to inertial frame A [24].

The velocity and acceleration of the vehicle are obtained through state transformation (Figure 3-4), with inertial coordinate system A and body orientated coordinate frame B [24]. The position of point q in inertial coordinates is expressed as a function of the location of the center of gravity p_{ab} and the rotation matrix R_{ab} (3-9).

$$q_a = p_{ab} + R_{ab} q_b \tag{3-9}$$

The transformation matrix R_{ab} is the product of the matrices describing rotations around the x-, y-, and z-axis (3-10).

$$R_x = \begin{bmatrix} 1 & 0 & 0 \\ 0 & \cos\phi & -\sin\phi \\ 0 & \sin\phi & cos\phi \end{bmatrix}, \quad R_y = \begin{bmatrix} \cos\theta & 0 & \sin\theta \\ 0 & 1 & 0 \\ -\sin\theta & 0 & \cos\theta \end{bmatrix}, \quad R_z = \begin{bmatrix} \cos\psi & -\sin\psi & 0 \\ \sin\psi & \cos\psi & 0 \\ 0 & 0 & 1 \end{bmatrix} \tag{3-10}$$

$$R_{ab} = R_x \cdot R_y \cdot R_z \tag{3-11}$$

The velocity v_{q_a} of point q in coordinate frame A is defined by that same transformation matrix, the time derivative, and an angular offset matrix $\dot{p}_{ab}$ (3-12).

$$v_{q_a} = \frac{\mathrm{d}}{\mathrm{d}t} q_a = \left(R_{ab}^T \dot{R}_{ab} \right) \times q_b + R_{ab}^T \dot{p}_{ab} \tag{3-12}$$

When the velocities of the vehicle (V_x and V_y) are obtained from the coordinate frame transformation, the accelerations can be calculated using the equations below.

$$a_x = \dot{V}_x + \omega_z V_y \tag{3-13}$$
$$a_y = \dot{V}_y - \omega_z V_x \tag{3-14}$$

The set of reflectors was placed on top of the BARC, with the center around 0.04 m above the COG of the vehicle. In $x-y-z$ sequence the position offset vector p_{ab} is $\begin{bmatrix} 0 & 0 & -0.04 \end{bmatrix}$. The rotational offset is tuned in two steps. As can be seen in the figure below, the rotational offset in each direction affect the velocities that are obtained. Consider Figure 3-5a; it can be observed that due to the offset ϕ_e the vector in the y' direction can be split into a component of the y and z axes. In the case of the MCS signals, rotational offsets in the reflectors cause lower velocities then were achieved during the experiment. Besides, velocity components on other axes could be observed. The MCS signals, therefore, require calibration.

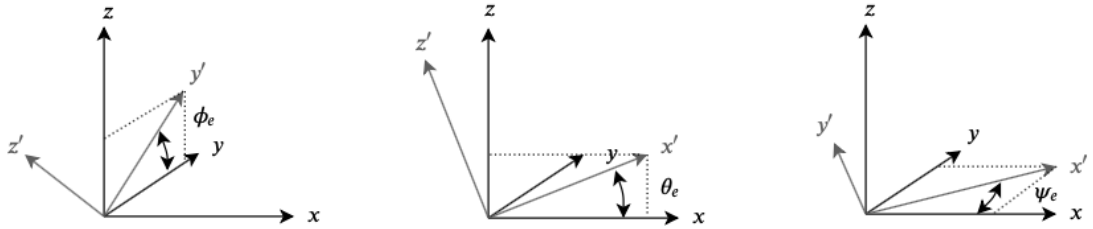

(a) Offset around the x-axis **(b)** Offset around the y-axis **(c)** Offset around the z-axis

Figure 3-5: Overview of the rotational offsets that can exist in each direction.

It is found that only the rotational offset in the z-direction is significant. As a result of the rotational offset ψ_e, the longitudinal velocity has a lateral component. When the vehicle is driving in a straight line, lateral velocity is observed. In order to verify the neutral steering position, the MCS position data of the straight line experiment (with neutral steering input) is studied. A small offset in the lateral direction is observed, the displacement is approximately 2% of the longitudinal displacement. This is considered significantly small to assume that the vehicle is driving in a straight line when the steering angle is in a neutral position.

Then the velocity signals belonging to the straight line experiment are analyzed. Although the lateral velocity is expected to be equal to zero, an offset is observed. For straight-line driving, the lateral velocity is much bigger than could result from the small lateral displacement observed from the position signals. Through an iterative process, the angular offset matrix $\dot{p}_{ab}$ is adjusted until the lateral velocity remains zero for neutral steering input. It is found that the offset varied over the two test days. Figure 3-6 shows lateral that was measured from two identical experiments conducted on different days. In the experiment, a sine wave was applied to the steering servo. At the start of the experiment, the steering is in the neutral position, and the lateral velocity should be approximately zero. On the first day, the offset ψ_e is 0.040 rad (Figure 3-6a), on the second day ψ_e equals 0.024 rad (Figure 3-6b).

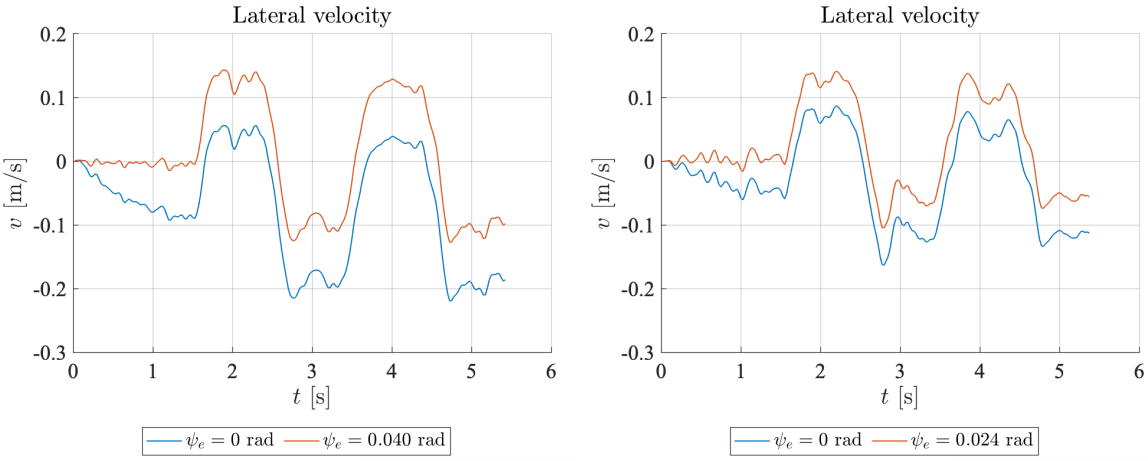

(a) Experiment 125 (day 1) **(b)** Experiment 145 (day 2)

Figure 3-6: Calibration of rotational offset ψ_e of the MCS in the z-direction: lateral velocity signals resulting from identical experiments performed on two different test days.

3-2 Data Processing

Data processing is a crucial part of system identification. The data that is used later on in the process first needs to be put in the right form. This section describes the modifications that have been made to the raw sensor data.

3-2-1 Filtering

Filtering of the raw signals is required to remove sensor noise. Continuing on the work that was presented in [37], the signals are filtered using the second-order Infinite Impulse Response Butterworth filter. The primary motivation for this type of filter is that it offers a relatively small phase delay at high frequencies. The cut-off frequency is set to be 15 Hz. The frequency response of the Butterworth filter is displayed in Figure 3-7.

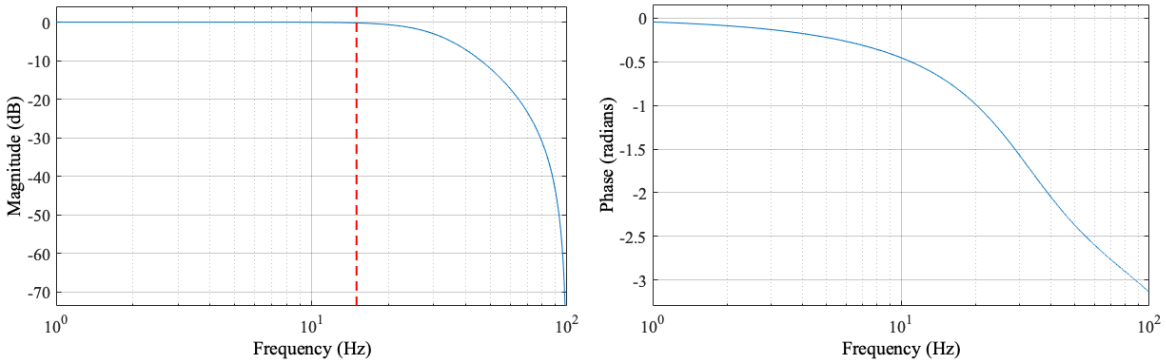

(a) Magnitude response **(b)** Phase response

Figure 3-7: Frequency response of the Infinite Impulse Response Butterworth filter.

3-2-2 Re-sampling

The measurement signals all have different frequencies. For the identification process, it is relevant that the signals have an equal amount of data points. Therefore, re-sampling of the signals is needed.

Table 3-1: List of available data signals and the corresponding sampling frequencies.

Component	Signals	Frequency
IMU	a_x, a_y, a_z, ω_x, ω_y, ω_z	100 Hz
ECU	$u_{throttle}$, u_{steer}	100 Hz
Encoders	$V_{wheel,F}$, $V_{wheel,R}$	50 Hz
MCS	x, y, z, ϕ, θ, ψ	120 Hz

To select a re-sampling frequency, the single-sided amplitude spectra are consulted (Figure 3-8). The data of experiment 125 is studied, in which a sine-wave steering input was applied to the vehicle. It is expected that the lateral accelerations will contain the highest frequencies. The signals of the MCS and IMU are studied. From the original sampling frequencies of the sensors (Table 3-1), it is concluded that no data extrapolation is required if the re-sampling frequency is lower than that of the encoders. This way, as much of the original data as possible can be maintained. In the amplitude spectra, the red dashed line represents a re-sampling frequency of 40 Hz. It is concluded that no vital information is lost with the proposed frequency. In the amplitude spectra of the lateral acceleration, frequencies up to approximately 10 Hz seem to be dominant for both the MCS and IMU signals.

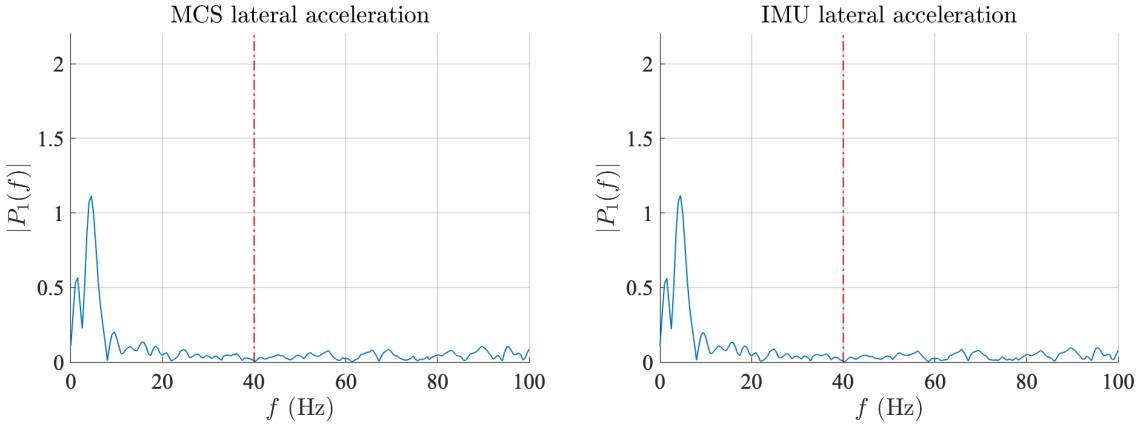

Figure 3-8: Single-sided amplitude spectrum of the filter sensor data of experiment 125.

3-2-3 Aligning

Aligning the data signals is required since each signal has a different starting point. The IMU gathers data as soon as the experiment begins, the MCS measurements are started manually. It is reasonable that differences in starting time result from this approach. The relative lag

between the IMU and MCS signals is calculated based on the cross-correlation of the yaw rate data signals.

To illustrate the phenomenon, an experiment is selected where the vehicle starts driving in a straight line (Figure 3-9). At approximately t = 13 seconds, the signals that are retrieved from the front axis encoder becomes larger than zero. The unaligned MCS signal of the longitudinal velocity is lagging the BARC approximately 1 second. The relative lag is calculated based on the yaw rate cross-correlation and is subtracted from the time signal. This process is defined as the first alignment step.

Although the lag is significantly reduced, there is still a small mismatch observable. To further improve the alignment of the signals, another iteration of lag calculation based on the cross-correlation is executed. This time the longitudinal accelerations are compared. The resulting second alignment accurate resembles the original encoder signal (Figure 3-9).

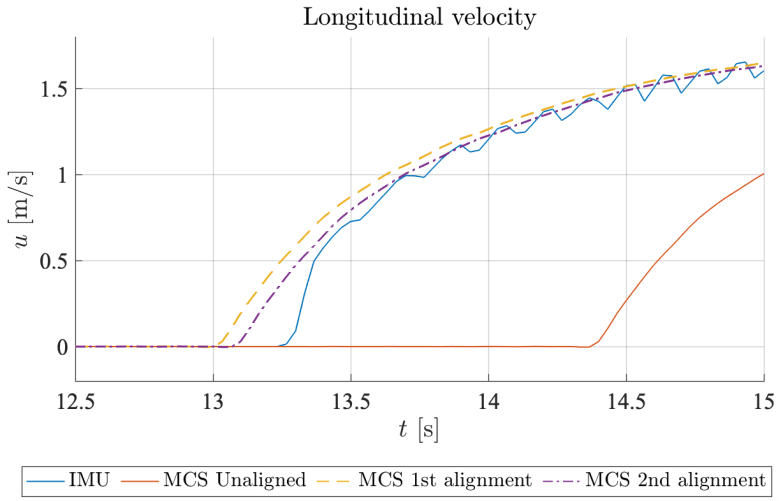

Figure 3-9: Comparison of the time delay between the IMU and MCS signals for a straight line driving experiment. Signals are aligned through computation of the cross-correlation between the signals.

3-3 Conclusions

This chapter discusses the sensory data that is available and elaborates on the required preprocessing which transform the raw data into the desired format. With regards to this goal, the following conclusions are formulated.

- Experimental data resulting from previously conducted experiments with a 1 : 10 scaled-vehicle are available. The data include signals from the Motion Capture System, the Internal Measurement Unit, and the Electronic Control Unit. The signals provide information about the position, the lateral and angular velocity, and the acceleration of the vehicle. Also, the angular velocities of the front and rear axles are obtained.

- The raw data signals consist of sensor noise and thus require filtering. The Butterworth filter is found to allow for low-pass filtering, practically without introducing any phase delay.
- The sensors all use different sampling frequencies. Therefore, re-sampling is required to transform all signals to the same format. Based on the single-side amplitude spectrum analysis, it is found that an appropriate sampling frequency is 40 Hz. No extrapolation of data is required in this case, while maintaining as much of the original data as possible.
- The starting time of the experiments is observed to vary for different sensors. In order to align the signals, a two-step approach is used. The time difference between two signals is computed based on the cross-correlation of the signals. First, the time delay based on the cross-correlation of the yaw rate is computed. Since a small delay remains, another adjustment based on the cross-correlation of the longitudinal acceleration signals is made.

After the presented approach, the data is considered to be in the correct format to be used for parameter identification purposes.

Chapter 4

Parameter Identification

After having processed the experimental data, the next step is the actual parameter identification. The models that are discussed in chapter 2 are general expressions, applicable to a wide variety of different vehicles. System-specific parameter identification is required to guarantee that the model is matching the dynamics of the vehicle of interest. The following chapter of this work determines the unknown model parameters which match the identified model to the dynamics of the scaled vehicle.

Section 4-1 provides an overview of the measurements and experiments that are carried out to find the model parameters. The chapter continues with the validation of the identified model in section 4-2. Section 4-3 proposes two modifications to the model that yields a better match between the simulated dynamics and the validation data. An overview of the most important findings is presented in 4-4.

4-1 Parameter Estimation

In the models that are presented in chapter 2, multiple variables appear that are unknown to this point. Consider the expression of the Dugoff tire model (2-7). In order to compute the tire forces, the longitudinal stiffness C_λ, the lateral stiffness C_α and the friction coefficient μ needs to be determined. Concerning the expression of the single-track model (2-21), it is vital to estimate the distances between the axles and the Center of Gravity (COG) (l_F, l_R), the mass of the vehicle (m), and the mass moment of inertia (I_z). Finally, the steering angle is present in both the tire model and the vehicle model. Only the input signal to the steering servo is available from the experimental data. Therefore, an accurate description of the input-output relationship of the steering mechanism needs to be determined.

This section elaborates on the process of estimating the above-described variables. The methodology is discussed, and the obtained values are presented.

4-1-1 Measurements

Multiple features of the Berkeley Autonomous Race Car (BARC) can be measured directly from the geometrical properties of the vehicle; no experimental data is required for this purpose. An overview is provided in Table 4-1.

Table 4-1: List of model parameters that are measured.

Symbol	Value	Description
m	1.986 kg	Vehicle mass
l_F	0.1265 m	Distance between the front axle and the COG
l_R	0.1335 m	Distance between the rear axle and the COG
L	0.26 m	Wheel base
w	0.165 m	Track width
r_{wheel}	0.00335 m	Wheel radius
m_{wheel}	0.04 kg	Mass of a single wheel

The parameters l_F and l_R logically depend on the location of the COG. The values are obtained from individually measuring the weights on both axles with weighing scales. The distance to the front and rear axle are calculated using (4-1). Here $F_{z,F}$ and $F_{z,R}$ denote the normal forces that act on the front and rear tire. The track-width is indicated by L.

$$l_f = L\frac{F_{z,R}}{F_{z,F}+F_{z,R}} \tag{4-1}$$

$$l_r = L - l_f \tag{4-2}$$

A parameter that can not be measured directly is the moment of inertia. An alternative method is described in [17]. The method derives an equation for the mass moment of inertia from studying the dynamics of a bifilar pendulum. When the BARC is suspended by two wires and rotated slightly around the z-axis, the motion when released can be described by

$$\ddot{\theta} + \left(\frac{K_p}{I}\dot{\theta}\left|\dot{\theta}\right| + \frac{C}{I}\dot{\theta}\right) + \left(\frac{mgD^2}{4Ih}\right)\frac{\sin\theta}{\sqrt{1-0.5\left(\frac{D}{h}\right)^2(1-\cos\theta)}} = 0. \tag{4-3}$$

This equation is simplified through the neglect of damping. For small rotation angles θ, the dynamics read as (4-4). The length of the wires are denoted by h, the distance between the wires is D, and finally, g is the gravitational acceleration.

$$\ddot{\theta} + \frac{mgD^2}{4hI}\theta = 0 \tag{4-4}$$

The movement of the suspended vehicle will be a sine wave with a particular natural frequency of oscillation ω_n. The moment of inertia can, therefore, be computed as:

$$I_{bp} = \frac{mgD^2}{4h\omega_n^2}. \tag{4-5}$$

The frequency of oscillation ω_n is calculated from measuring the time intervals between the maximum angles of rotation. The detailed estimation is described in appendix B. The aforementioned approach is validated by assuming that the BARC is a cuboid with length L and width w. The mass moment of inertia of a cuboid is defined by

$$I_c = \frac{m}{12}\left(L^2 + w^2\right). \tag{4-6}$$

The resulting moment of inertia, denoted by I_c, is within 21% of the value obtained with the bifilar pendulum method I_{bp} (Table 4-2). Although this is a significant difference, it is disputable which method provides the most accurate value. The bifilar pendulum method is based on more measurements. However, the maximum heading angle θ is approximately $\frac{\pi}{6}$ rad (30°). This is conflicting with the assumption that the rotation angles are small. However, it is calculated that this could yield an error of 4.3%. Given the fact that it is challenging to estimate the length and width of the cuboid accurately, would the BARC be considered as such, the bifilar pendulum method is considered to be the most accurate.

Table 4-2: Mass moment of inertia values resulting from the bifilar pendulum method (I_{bp}) and the cuboid method (I_c).

Symbol	Value	Description
I_{bp}	$2.25 \cdot 10^{-2}$ kg m^2	Moment of inertia resulting from bifilar pendulum method
I_c	$2.72 \cdot 10^{-2}$ kg m^2	Moment of inertia resulting from cuboid method

4-1-2 Steering Identification

The Electronic Control Unit (ECU) provides the input signal that was sent to the steering servo during the experiments. From the motion of the vehicle, the steering angle can be retrieved. An accurate estimation of the steering angle is relevance since this allows for determining the tire-related parameters. This will be addressed in section 4-1-3.

Multiple approaches can be applied to determine the relationship between the input of the steering servo and the actual angle of the front wheels. In this chapter, a dynamic approach is discussed based on the experimental data of the moving vehicle. The results are validated with a static identification method. The dynamic identification is considered to yield more accurate results, as it takes into account the force that acts on the steering mechanism during vehicle motion. A detailed description of the static steering identification is provided in appendix B-3.

In the dynamic identification, the relationship between the steering servo input and the front steering angle is estimated based on the experimental data. The experiments that are selected for the steering identification are those in which a ramp signal is applied to the steering servo (Table 4-3). It can be observed that there are significantly fewer experiments for right-hand corners (negative steering angles). This is motivated by the practical issue that the maximum steering angle for a right-hand corner is smaller compared to the opposite side. Making the right corner requires more space which was not available in the testing arena.

Table 4-3: List of experiments that are used for the dynamic steering identification.

Experiments	**Maneuver type**	**Steering range**	
110	Left corner	$[0, 0.087]$ rad	$[0, 5]^\circ$
113, 114	Left corner	$[0.087, 0.174]$ rad	$[5, 10]^\circ$
117, 155, 156, 158, 159, 161	Left corner	$[0.174, 0.262]$ rad	$[10, 15]^\circ$
120	Right corner	$[\frac{-\pi}{36}, 0]$ rad	$[-5, 0]^\circ$
119	Right corner	$[\frac{-\pi}{18}, \frac{-\pi}{38}]$ rad	$[-10, -5]^\circ$
122	Right corner	$[\frac{-\pi}{12}, \frac{-\pi}{18}]$ rad	$[-15, -10]^\circ$

Based on the Motion Capture System (MCS) signals, the steering angle is computed from the Ackermann steering expression:

$$\delta_{ackermann} = \frac{(l_F + l_R)\, r}{V_x}. \tag{4-7}$$

Nonlinear least-squares fitting is used to estimate the steering angle. The yaw rate r and longitudinal velocity V_x are obtained from the MCS data.

$$\hat{\delta}_{d,left} = \min\left(b_1, b_2\left(u_{servo} - 90.88\right)\right) \tag{4-8}$$

$$\hat{\delta}_{d,right} = \max\left(b_3, b_4\left(u_{servo} - 90.88\right)\right) \tag{4-9}$$

$$\tag{4-10}$$

The estimated steering angle $\hat{\delta}_d$ (subscript d indicates the dynamic approach) depends on steering servo input u_{servo} and the fitting coefficients (b_1, b_2, b_3, b_4), which are obtained from least-squares fitting.

$$\min_{b_1,b_2,b_3,b_4} \left\|e_\delta(b_1, b_2, b_3, b_4)\right\|_2^2 = \min_{b_1,b_2,b_3,b_4} \left\|\delta_{ackermann} - \hat{\delta}_d(b_1, b_2, b_3, b_4)\right\|_2^2 \tag{4-11}$$

Figure 4-1 displays the identified steering fit. For left cornering, i.e. positive steering angles, 8110 data points are available, and the root-mean-squared error of the fit is 0.018 rad (1.03°). For right cornering, indicated by negative steering angles, 1488 data points are available, and a fit with a root mean squared error of 0.017 rad (0.95°) is obtained.

Although it was already observed in practice that the maximum attainable steering angle for left-hand corners was larger than for right turns, the difference is significant. With maximum angles of 0.291 rad (16.7°) and −0.239 rad (−13.7°) for right and left side, the right-hand turn is almost 18% smaller.

Steering Delay

From square-steer experiments, it is observed that the steering dynamics introduces a time delay in the lateral velocity. Therefore a delay of 0.1 second is introduced in the steering

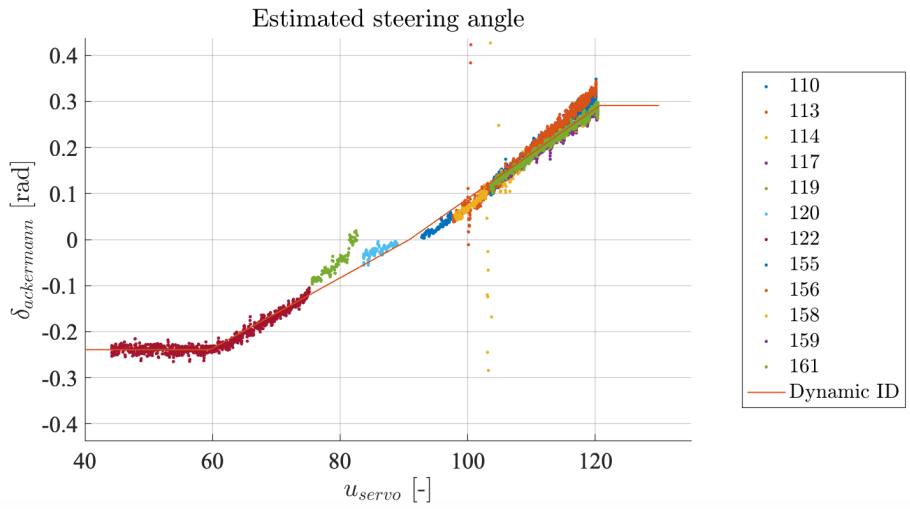

Figure 4-1: Dynamic steering identification based on the computed ackermann steering angle.

input. The yaw response for the square wave steering input is displayed in Figure 4-2. The validation data, in purple, is the yaw rate that was obtained from the MCS. The green line represents the yaw rate that is recorded by the Internal Measuring Unit (IMU) of the vehicle. The dashed line is the initial response, and the solid line is the response with the time delay. It is observed that the response of the simulation is more in line with the validation data when the delay is included

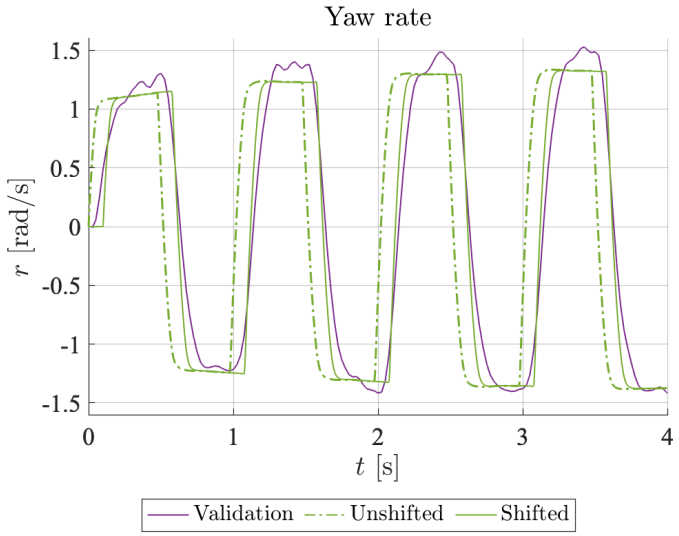

Figure 4-2: Comparison of yaw response between the validation data and the simulation with unshifted and shifted steering input.

4-1-3 Tire Identification

The next step towards being able to model the dynamics of the BARC accurately is the estimation of the tire-related parameters. In section 2-2 it is mentioned that the generated tire forces are fundamental for the vehicle dynamics. The Dugoff tire model is selected, which requires the estimation of the friction coefficient μ, the lateral cornering stiffness of the front and the rear tires; $C_{\alpha,F}$ and $C_{\alpha,R}$ respectively.

Due to the coupling of tire forces, tires can only generate a limited amount of force. Since this is the resultant of the directional tire forces, also the longitudinal tire stiffness is relevant. The availability of an accurate longitudinal slip signal is a necessity for this purpose (2-5). Given the fact that the vehicle's drive-train is a Rear Wheel Drive (RWD) configuration, only the rear wheels provide significant longitudinal slip values that allow for estimating the longitudinal tire stiffness.

For the tire identification, steady-state cornering (zero yaw acceleration) is assumed. From the equations of motion (2-21), the tire forces under steady-state cornering conditions can be calculated. The longitudinal acceleration is a result of the forces generated at the two rear wheels. The lateral dynamics are caused by the sum of the lateral forces generated at all tires. For a single front and a single rear tire, the steady-state (zero yaw acceleration) tire forces are expressed as:

$$F_{x,R,ss} = \frac{1}{2} m \left(\dot{u} - vr \right), \tag{4-12}$$

$$F_{y,F,ss} = \frac{1}{2} \frac{l_R}{l_F + l_R} m \left(\dot{v} + ur \right), \tag{4-13}$$

$$F_{y,R,ss} = \frac{l_F}{l_R} F_{y,F,ss}. \tag{4-14}$$

The equations described above are based on the assumption that the steering angle is significantly small such that $\cos(\delta) = 1$. The maximum steering angle during the experiments is found to be 0.288 rad (16.50°), which introduces an error of 4.12%. From (2-5) and (2-6), the steady-state longitudinal and lateral slip values are computed.

$$\alpha_{F,ss} = \hat{\delta} - \tan^{-1}\left(\frac{v + l_F r}{u} \right) \tag{4-15}$$

$$\alpha_{R,ss} = -\tan^{-1}\left(\frac{v - l_R r}{u} \right) \tag{4-16}$$

$$\lambda_{i,ss} = \frac{r_{wheel} \cdot \omega_{wheel,i} - u}{\max\left(r_{wheel} \cdot \omega_{wheel,i},\ u \right)} \quad i = \{F, R\} \tag{4-17}$$

Table 4-4: Overview of the experimental data that is used for the tire identification.

Experiments	Description
155, 158, 161, 163	Increasing steering angle, constant longitudinal velocity
165, 167	Constant steering angle, increasing longitudinal velocity
104, 105, 108	Vehicle accelerates in a straight line

Rear wheels

Since the BARC is rear-wheel driven, it is more convenient to use the rear axle to determine the friction coefficient μ. The longitudinal experiments are limited. Any slip at the driven wheels would be more visible at the rear wheels than at the front wheels.

The tire parameters are obtained using the nonlinear optimization toolbox of MATLAB. The tire forces calculated from (4-12). The steady-state values of the longitudinal and lateral slip are inputs to the Dugoff tire model. The friction coefficient μ and tire stiffness coefficient $C_{\lambda,R}$ and $C_{\alpha,R}$ result from the nonlinear least-squares fitting (4-18).

$$\min_x \left\|e_{F_R}(x)\right\|_2^2 = \min_x \left\| [F_{x,ss,R}, F_{y,ss,R}] - f_{Dugoff}\left(x_1, x_2, \lambda_R, \alpha_R, x_3, F_{z,R}\right)\right\|_2^2 \tag{4-18}$$

$$x_1 = C_{\lambda,R} \tag{4-19}$$

$$x_2 = C_{\alpha,R} \tag{4-20}$$

$$x_3 = \mu \tag{4-21}$$

With,

$$\lambda_R = \begin{bmatrix} \lambda_{R,ss}(1) \\ \vdots \\ \lambda_{R,ss}(N_{lon}) \\ 0 \\ \vdots \\ 0 \end{bmatrix}, \ \alpha_R = \begin{bmatrix} 0 \\ \vdots \\ 0 \\ \alpha_{R,ss}(1) \\ \vdots \\ \alpha_{R,ss}(N_{lat}) \end{bmatrix}, \ F_{x,R} = \begin{bmatrix} F_{x,R,ss}(1) \\ \vdots \\ F_{x,R,ss}(N_{lon}) \\ 0 \\ \vdots \\ 0 \end{bmatrix}, \ F_{y,R} = \begin{bmatrix} 0 \\ \vdots \\ 0 \\ F_{y,R,ss}(1) \\ \vdots \\ F_{y,R,ss}(N_{lat}) \end{bmatrix} \tag{4-22}$$

From the structure of the above described matrices it becomes apparent that the tire identification is performed under the assumption of pure longitudinal and lateral dynamics. The longitudinal experiments (100, 105, 108) provide N_{lon} data points. The lateral experiments (155, 158, 161, 163, 165, 167) together provide N_{lat} data points. Therefore, the vectors λ_R, α_R, $F_{x,R}$ and $F_{y,R}$ have dimension $\mathbb{R}^{(N_{lon}+N_{lat})\times 1}$.

The resulting coefficients are listed in Table 4-5. Based on 7176 data points, the root-mean squared error is 0.58 N. The fit of the tire curves are displayed in Figure 4-3

Table 4-5: Tire parameters resulting from the rear tire identification.

Symbol	Value	Description
μ	0.57	Tire-road friction coefficient
$C_{\lambda,R}$	19.57 $\mathrm{N\,rad^{-1}}$	Rear tire longitudinal tire stiffness
$C_{\alpha,R}$	39.65 $\mathrm{N\,rad^{-1}}$	Rear tire lateral cornering stiffness

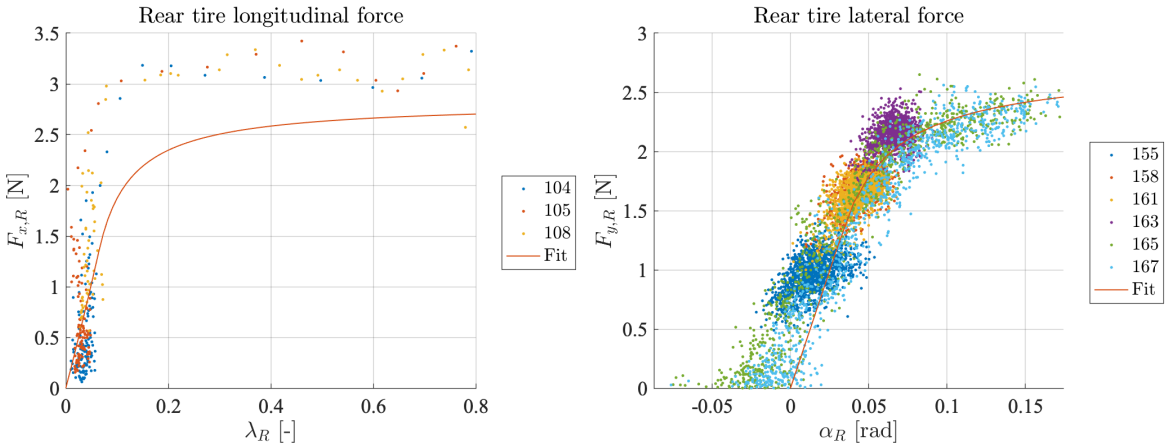

(a) Longitudinal direction **(b)** Lateral direction

Figure 4-3: Tyre identification fit of the rear wheels. Based on 7176 data points, the root-mean squared error is 0.58 N.

Front wheels

The friction coefficient μ that was obtained from the rear wheels are used to estimate the front wheel coefficients. Since the front wheels are non-driven, the longitudinal slip is marginal, which makes it more challenging to estimate a relationship between slip angles and the resulting longitudinal tire forces. Therefore, the rear longitudinal tire stiffness is also used for the front wheels.

The nonlinear least squares problem for the front tires is formulated as:

$$\min_x \|e_{F_F}(x)\|_2^2 = \min_x \left\| [F_{x,F}, F_{y,F}] - f_{Dugoff}\left(C_{\lambda,F}, x, \lambda_F, \alpha_F, \mu, F_{z,F}\right) \right\|_2^2 \tag{4-23}$$

$$x = C_{\alpha,F} \tag{4-24}$$

Where,

$$\lambda_F = \begin{bmatrix} 0 \\ \vdots \\ 0 \end{bmatrix}, \ \alpha_F = \begin{bmatrix} \alpha_{F,ss}(1) \\ \vdots \\ \alpha_{F,ss}(N_{lat}) \end{bmatrix}, \ F_{x,F} = \begin{bmatrix} 0 \\ \vdots \\ 0 \end{bmatrix}, \ F_{y,F} = \begin{bmatrix} F_{y,F,ss}(1) \\ \vdots \\ F_{y,F,ss}(N_{lat}) \end{bmatrix} \tag{4-25}$$

Since the longitudinal tire stiffness is not identified for the front tire, only the experiments that focus on the lateral dynamics are used. The vectors λ_F, α_F, $F_{x,F}$ and $F_{y,F}$ have dimension $\mathbb{R}^{N_{lat}\times 1}$. The resulting coefficients are listed in Table 4-6. Based on 6797 data points, the root-mean squared error is 0.17 N. The fit of the tire curve is displayed in Figure 4-4.

From Figure 4-4 unexpected results are observed for the experiments 165 and 167. Positive lateral tire forces are found to correspond with negative lateral slip angles. It is assumed that this is caused by offsets in the MCS measurements.

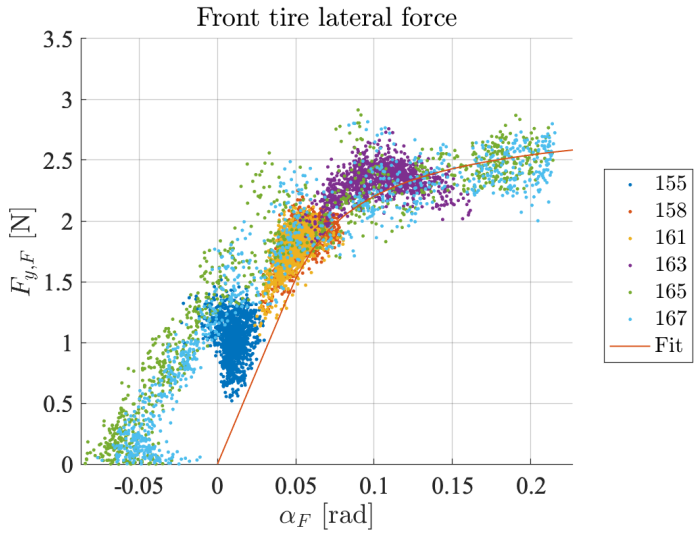

Figure 4-4: Tyre identification fit of the rear wheels. Based on 6797 data points, the root-mean squared error is 0.17 N.

Table 4-6: Tire parameters resulting from the front tire identification.

Symbol	Value	Description
$C_{\alpha,F}$	30.652 N rad^{-1}	Front tire lateral cornering stiffness

4-2 Model Validation

The identified model is validated based on three experiments. The primary motivation for selecting these specific experiments is that high motor power and large steering angles are combined (Table 4-7). This way, the tires are pushed towards the limits of friction. When the model can accurately describe the dynamics of the vehicle during these experiments, the model is considered to be suitable for optimization purposes. Although the tire identification was performed based on the tire forces, the dynamics of the vehicle are assessed to validate the identified model. If the model is capable of accurately describing the generation of tire force, it is expected that the motion that results from the forces is a match with the validation data.

Table 4-7: Overview of the experiments that are used for the validation of the identified model.

Code	Experiment	Description
A	Sine-steer	$F_{x,R}$ 2.25 N - δ sine with amplitude 0.44 rad (25°) and $f = 0.5$ Hz
B	Steer-ramp	$F_{x,R}$ 2.7 N - δ gradually increases $0.17 - 0.44$ rad $(10 - 25°)$
C	Force-ramp	$F_{x,R}$ gradually increases $1 - 3.75$ N - δ 0.26 rad (15°)

Experiment A: sine-steer maneuver

From Figure 4-5 it is concluded that the model accurately described the dynamics of the BARC for the sine-steer maneuver that is specified in Table 4-7. Although the peak values of the side-slip angle are not exactly matched, probably due to a small offset in lateral velocity, the yaw rate is followed more closely.

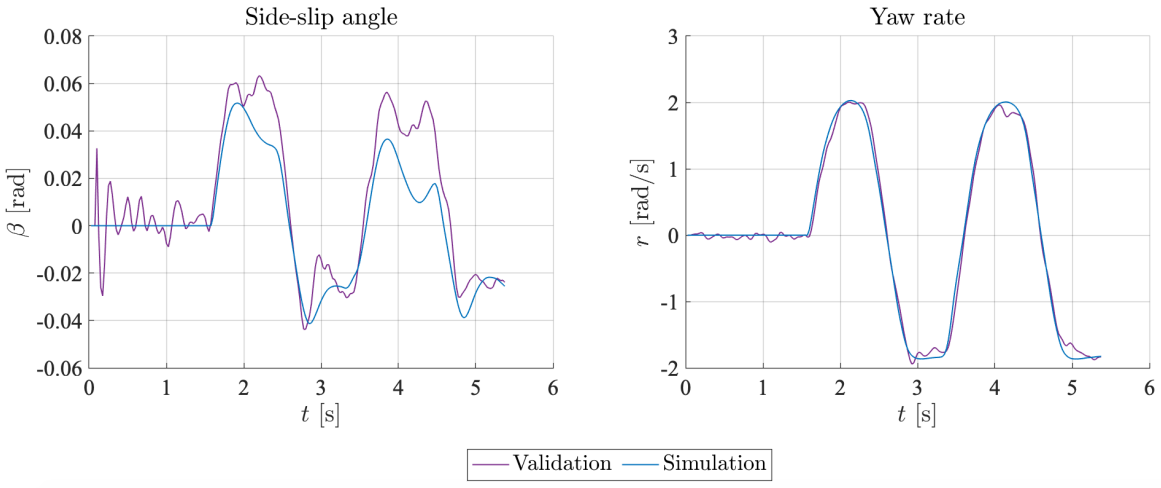

Figure 4-5: Experiment A: Comparison between the validation and simulation data based on the side-slip angle β and the yaw rate r.

Experiment B: steer-ramp maneuver

The comparison for the increasing steering angle maneuver is displayed in Figure 4-6. For this experiment, the side-slip angle resulting from the simulation is different from the validation data. Where the validation data shows a positive body side-slip angle as soon as the steering input is applied, the simulation side-slip angle becomes positive only 20 seconds later. In the right graph of Figure 4-6, a close match is observed for the yaw rate signals.

The tire side-slip angles are displayed in Figure 4-7. It is contradicting that the simulation slip angles are higher than the validation data since this would imply higher lateral tire forces, thus higher lateral velocity and therewith an increased body side-slip angle.

Experiment C: force-ramp maneuver

During the final experiment, both the body side-slip angle and yaw rate become oscillatory, unstable Figure 4-8. The cause is found in the longitudinal slip of the rear tire Figure 4-9.

Around $t = 23$ s, the longitudinal slip ratio becomes equal to 1, indicating that the rear tire starts spinning. The vehicle loses grip and spins out of control.

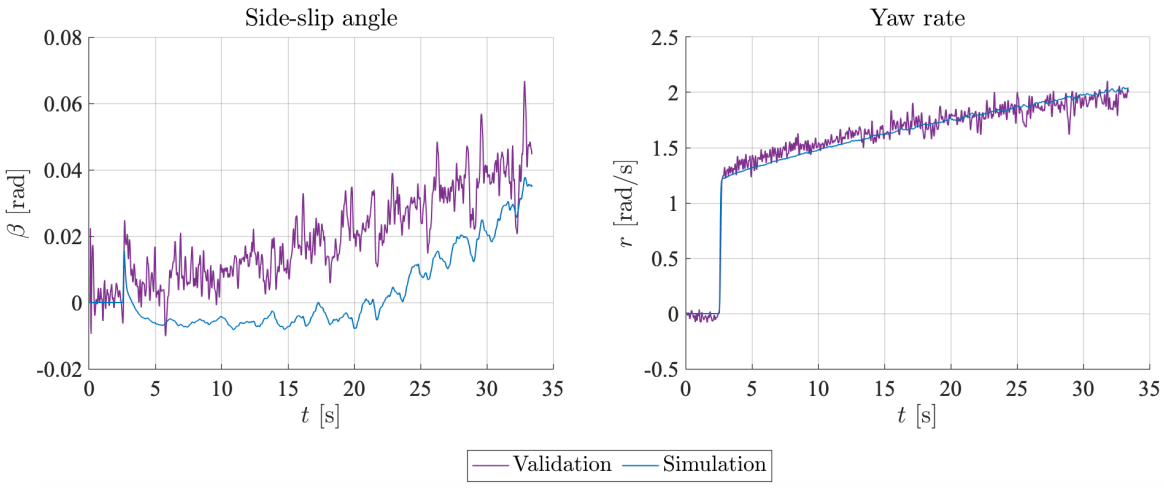

Figure 4-6: Experiment B: Comparison between the validation and simulation data based on the side-slip angle β and the yaw rate r.

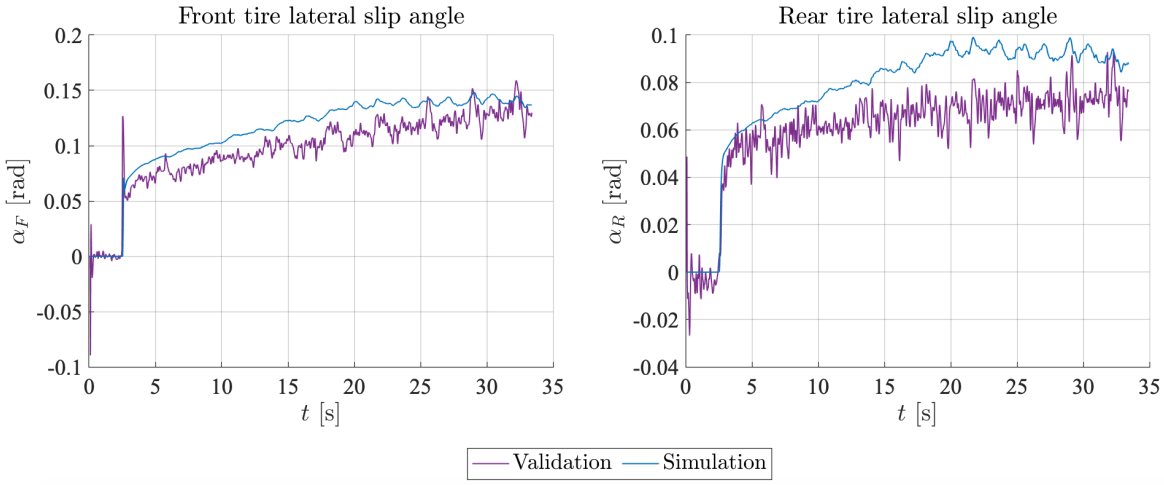

Figure 4-7: Experiment B: Comparison between the validation and simulation data based on the front α_F and rear lateral slip angle α_R.

Assessment of the fitting quality

Studying the comparison of the validation and simulation signals is one method to conclude on the quality of the identified model. A more value-based approach is to compute the Variance Accounted For (VAF) and Root Mean Squared Error (RMSE). For the three experiments, values are listed in Table 4-8.

Similar conclusions are drawn. Both the VAF and RMSE are decent for experiment A. For experiment B, the results are reasonable, but for experiment C, the model is not an accurate description of the validation data.

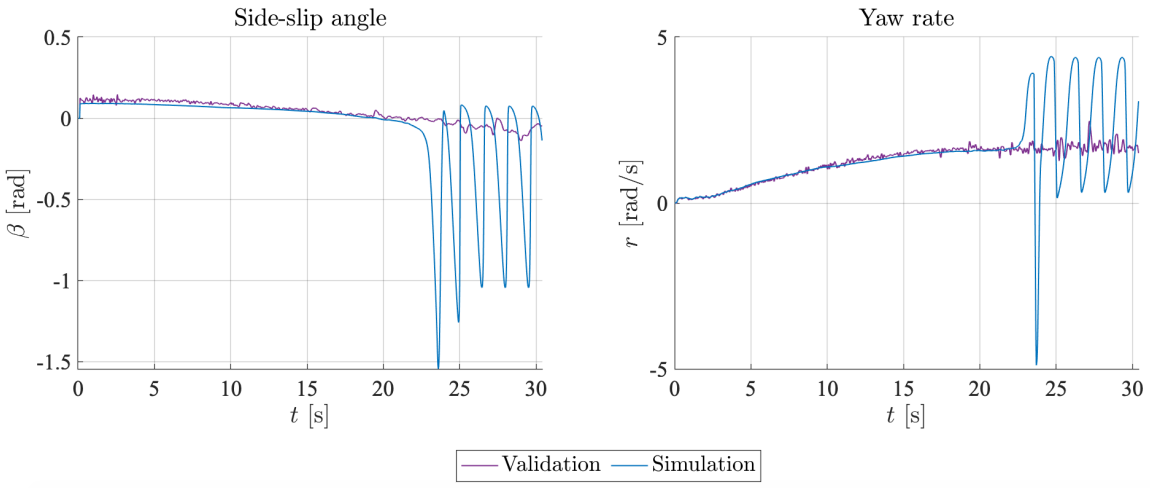

Figure 4-8: Experiment C: Comparison between the validation and simulation data based on the side-slip angle β and the yaw rate r.

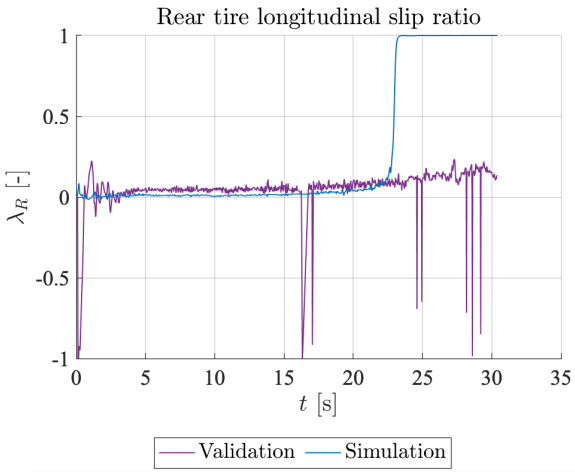

Figure 4-9: Experiment C: Comparison between the validation and simulation data based on the rear longitudinal slip ratio λ_R.

Table 4-8: Assessment of the fit between the validation and simulation data: VAF and RMSE for body sideslip angle and yaw rate signals.

Code	**VAF** β	**RMSE** β	**VAF** r	**RMSE** r
A	86.91%	0.014 rad (0.79°)	99.34%	0.103 rad (5.90°)
B	64.65%	0.018 rad (1.06°)	97.71%	0.076 rad (4.34°)
C	-1.55 $\cdot 10^3$%	0.280 rad (16.03°)	-220.26%	0.975 rad (55.88°)

4-3 Modifications to the Identified Model

Although the identified vehicle model yields accurate results for a great variety of experiments, two particular types of experiments are problematic. In these experiments (B & C of Table 4-

7), lateral maneuvers are executed with the highest motor torque. These conditions push the tires to the limit of friction, which is interesting with regards to drifting. In this section, modifications to the identified Dugoff model that increase the accuracy of the vehicle model in describing the BARC dynamics are discussed.

4-3-1 Increased Friction Coefficient

A deeper understanding of the tire-road interaction is required to understand why the dynamics resulting from the model are so different from the validation data. In figure Figure 4-10, the effect of the longitudinal slip on the lateral tire force is depicted. The dots correspond to the steady-state values that are computed from the experimental data (Section 4-1-3). The lateral tire forces F_y are plotted against the longitudinal slip ratio λ. The dots are categorized based on the value of the steady-state lateral slip angle α. The lines are obtained from the Dugoff tire model. For a specific lateral slip angle, the lateral tire forces are computed for varying slip ratios. The lines are referred to as constant-α lines. As the graphs show the lateral tire forces as a function of the slip conditions, it provides insight into the coupling effect of the tire model.

It is observed that the tire model does not accurately describe the force coupling. The blue dots denote slip angles between 0 and 0.1 rad, the red dots denote slip angle between 0.1 and 0.2 rad. With the current tire model, some of the data points obtained from the validation data do not lie within the corresponding region defined by the constant-α lines. Only 58.3% and 48.6% of the data points of the front and the rear wheel is in the correct region.

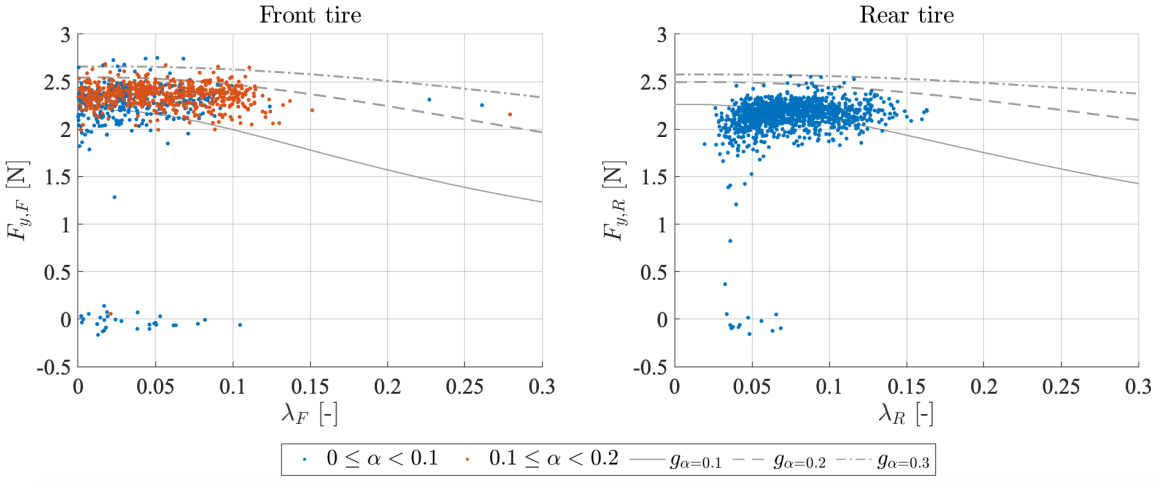

Figure 4-10: Coupling effect of the tires. Longitudinal slip λ versus lateral tire force F_y. Blue dots denote 0 rad $\leq \alpha <$ 0.1 rad, red dots denote 0.1 rad $\leq \alpha <$ 0.2 rad.

To solve this problem, the friction coefficient is increased. The result of this approach is displayed in Figure 4-11. The friction coefficient is increased by 10%. This value is the result of an iterative process. For higher values, the percentage of data points that fit decrease. With the increased friction coefficient, 59.4% and 84.0% of the data points of the front and rear validation data are in the correct range. The increase in friction is implemented by multiplying the friction coefficient in the Dugoff tire model (2-7) with the coefficient $e_\mu = 1.1$.

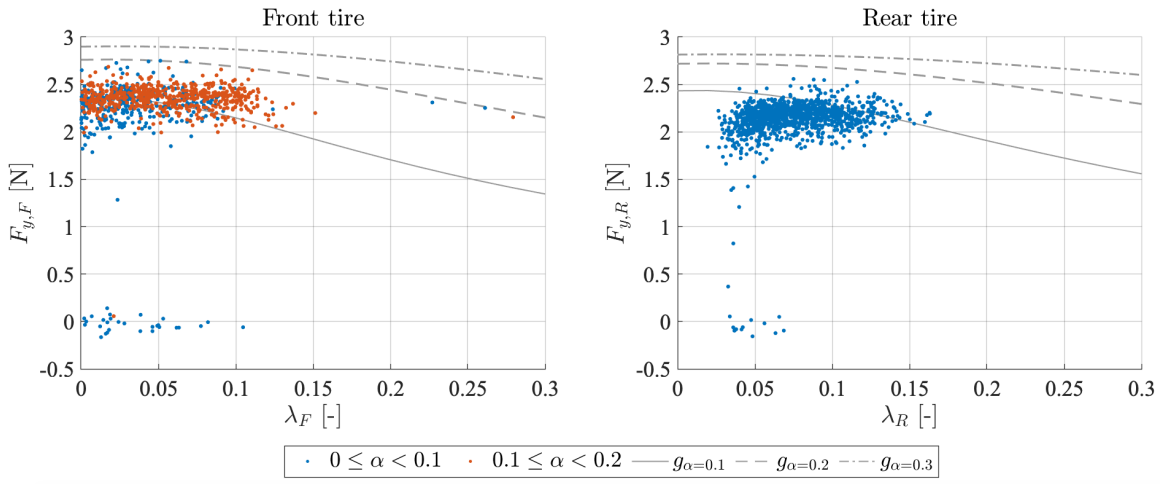

Figure 4-11: Coupling effect of the tires with increase friction coefficient. Longitudinal slip λ versus lateral tire force F_y. Blue dots denote 0 rad $\leq \alpha <$ 0.1 rad, red dots denote 0.1 rad $\leq \alpha <$ 0.2 rad.

The renewed comparison of the side-slip angle and yaw rate is shown in Figure 4-6. The simulated body side-slip angle more accurately matches the validation data. Although the signal is slightly lower than the validation data, the moment at which it becomes positive is approximately the same.

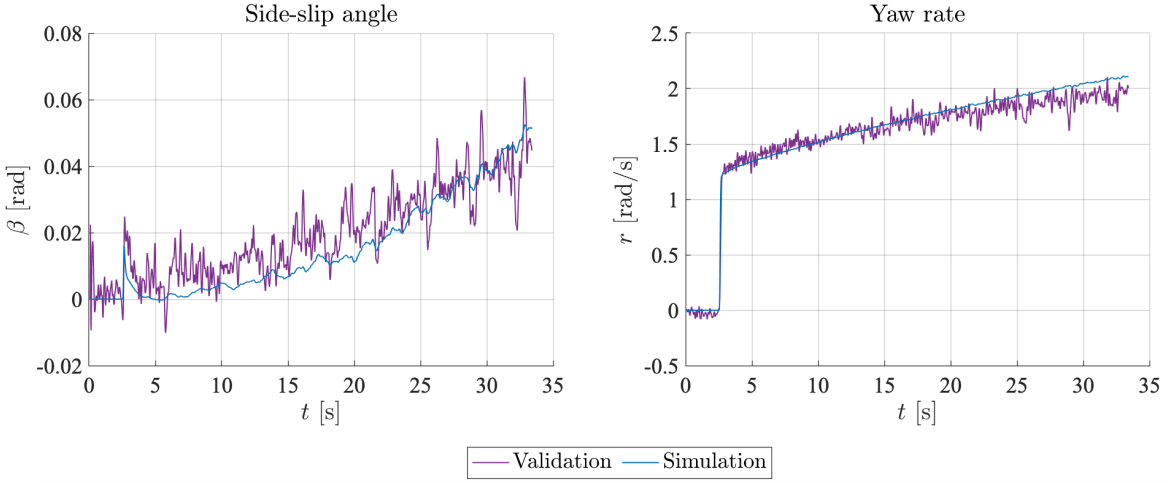

Figure 4-12: Experiment B with increased μ: Comparison between the validation and simulation data based on the side-slip angle β and the yaw rate r.

4-3-2 Modified Coupling Effect

The tire characteristics of experiment C are depicted in Figure 4-13. Again, it is observed that the constant-α lines are lower than the validation data points. Therefore increasing the friction coefficient would be the first improvement. It is increased with 10%, similar to the

previous section. Additionally, the coupling effect of the tires is too strong. For increasing longitudinal slip λ, the decrease in lateral force F_y of the lines is too steep compared to what is observed from the validation data.

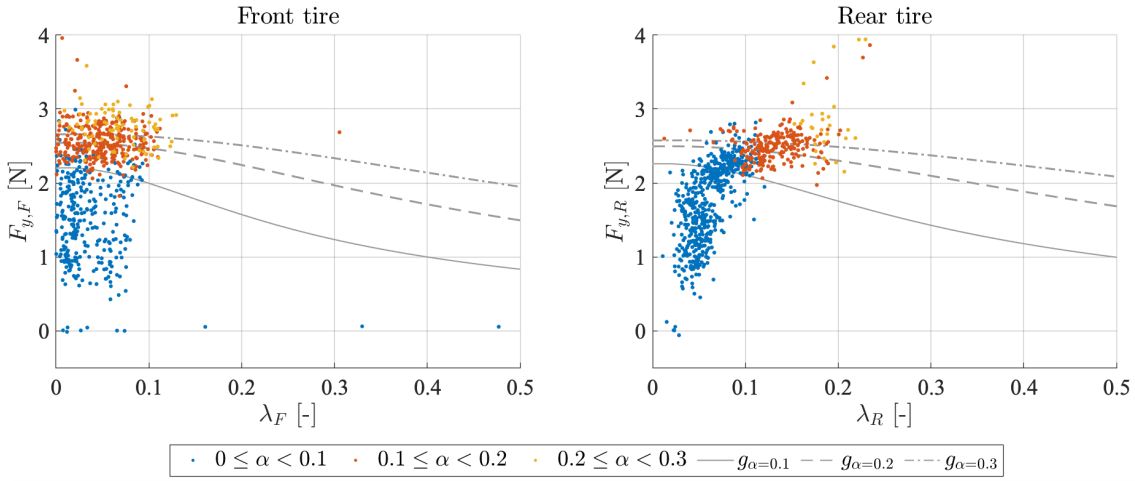

Figure 4-13: Coupling effect of the tires for experiment C. Longitudinal slip λ versus lateral tire force F_y. Blue dots denote 0 rad $\leq \alpha <$ 0.1 rad, red dots denote 0.1 rad $\leq \alpha <$ 0.2 rad, yellow dots denote 0.2 rad $\leq \alpha <$ 0.3 rad.

In order to solve this problem, the characteristics of the Dugoff model needs to be adjusted. A modification is proposed that weakens the coupling effect, by introducing a parameter $e_{coupled}$. The parameter is added to the original Dugoff model (2-7). The modified tire model reads as:

$$F_x = C_\lambda \frac{\lambda}{1+\lambda} f(\zeta), \tag{4-26}$$

$$F_y = C_\alpha \frac{\tan(\alpha)}{1+\lambda} f(\zeta), \tag{4-27}$$

$$f(\zeta) = \begin{cases} (2-\zeta)\zeta & \text{, if } \zeta < 1 \\ 1 & \text{, if } \zeta \leq 1 \end{cases}, \tag{4-28}$$

$$\zeta = \frac{\mu F_z (1+\lambda)}{2\sqrt{e_{coupled} \cdot (C_\lambda \lambda)^2 + (C_\alpha \tan\alpha)^2}}. \tag{4-29}$$

From an iterative process of varying the coupling factor and evaluating the percentage of data points that fit within the iso-lines result in Figure 4-14. The coupling factor $e_{coupled}$ equals 0.5. For the front and rear, the fit was previously 44.2% and 37.4%. With the combination of the reduced coupling coefficient and increased friction coefficient, this changes to 58.2% and 56.8%.

The newly obtained dynamics now better match the validation data. The simulated no longer becomes unstable; both signals are free from oscillations (Figure 4-15). The side-slip angle is not perfectly matched, but it must be noted that the validation data is obtained under the assumption of steady-state conditions. Especially on this experiment, which the highest motor power, this could introduce a mismatch between the simulation and validation data.

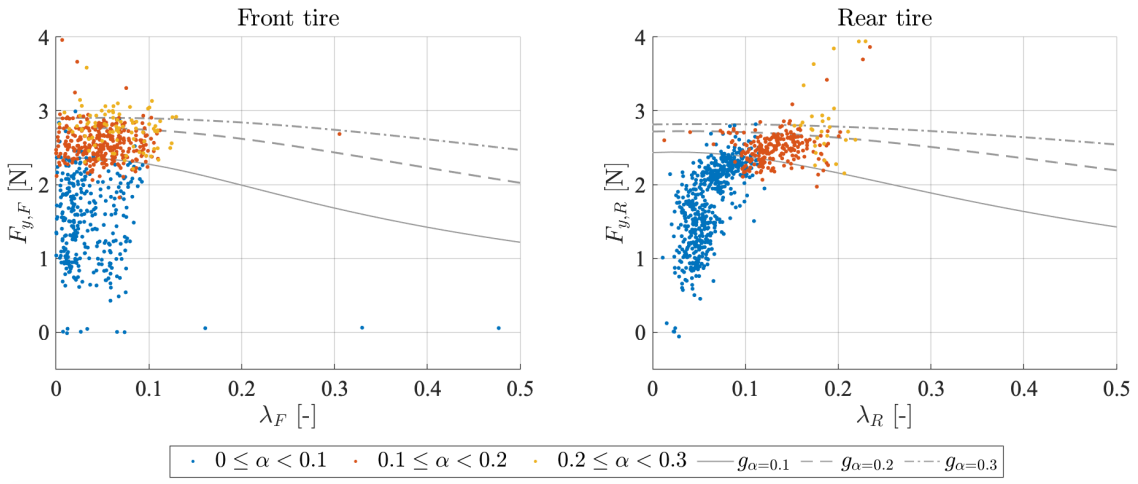

Figure 4-14: Coupling effect of the tires for experiment C with decreased $e_{coupled}$. Longitudinal slip λ versus lateral tire force F_y. Blue dots denote 0 rad $\leq \alpha < 0.1$ rad, red dots denote 0.1 rad $\leq \alpha < 0.2$ rad, yellow dots denote 0.2 rad $\leq \alpha < 0.3$ rad.

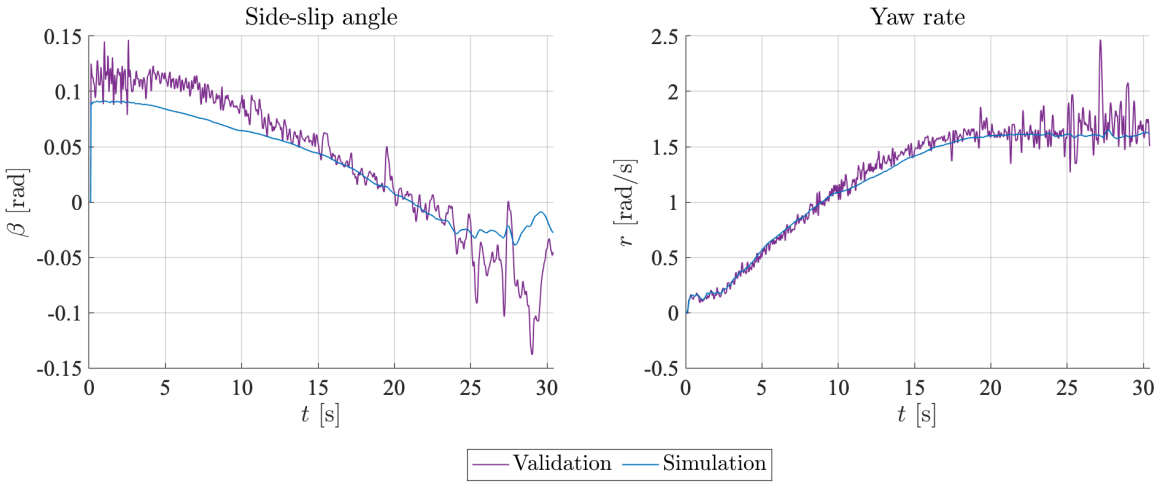

Figure 4-15: Experiment C with decreased $e_{coupled}$: Comparison between the validation and simulation data based on the side-slip angle β and the yaw rate r.

Selection of Tire Model Modification

In the previous sections, two different approaches are discussed that yield more accurate results for specific experiments. This section will evaluate the effect of these modifications on the three experiments. In addition to the comparison that is already made without any modification to the tire model, the following scenarios are considered.

1. Only the friction coefficient is increased $\left(e_\mu = 1.1, e_{coupled} = 1\right)$

2. Also the tire coupling effect is weakened $\left(e_\mu = 1.1, e_{coupled} = 0.5\right)$

For each scenario, the experiments are simulated with the corresponding modification to the

tire model. The VAF and RMSE are computed and listed in Table 4-9.

Increasing the friction coefficient (scenario 1) increases the VAF and decreases the RMSE values for all the experiments. For experiment C, however, the values are still unsatisfactory. As was previously concluded, the combination of the increased friction coefficient and the modified coupling parameter achieves satisfactory results. From Table 4-9 it is observed that even for experiment C_2 the VAF and RMSE values are now in of the same order of magnitude as the other experiments. Given the fact that the results of A_1 and B_1 are approximately equal to the values obtained in A_2 and B_2, this modification will be used throughout the remaining of the research.

Table 4-9: Assessment of the fit between the validation and simulation data for varying tire model modifications: VAF and RMSE for body sideslip angle and yaw rate signals with adjusted Dugoff model.

Code	VAF β	RMSE β	VAF r	RMSE r
A	86.91%	0.014 rad (0.77°)	99.34%	0.103 rad (5.90°)
A_1	92.15%	0.012 rad (0.67°)	98.98%	0.128 rad (7.35°)
A_2	92.18%	0.012 rad (0.67°)	98.98%	0.128 rad (7.32°)
B	64.65%	0.018 rad (1.06°)	97.71%	0.076 rad (4.34°)
B_1	77.76%	0.008 rad (0.44°)	97.19%	0.093 rad (5.32°)
B_2	76.15%	0.007 rad (0.41°)	97.32%	0.089 rad (5.07°)
C	-1.55e+03%	0.280 rad (16.03°)	-220.26%	0.975 rad (55.88°)
C_1	-939.54%	0.218 rad (12.48°)	-123.00%	0.808 rad (46.29°)
C_2	82.94%	0.027 rad (1.54°)	96.19%	0.112 rad (6.41°)

4-4 Conclusions

The purpose of this chapter is to determine the unknown model parameters such that the identified model matches the dynamics of the scaled vehicle. This is done either through direct measurements or through numerical parameter estimation. In this chapter, it is described that:

- Several model parameters are directly measured. This includes the mass of the vehicle, the location of the center of gravity, the mass moment of inertia, the wheel radius, and the mass of each wheel.
- The steering identification uses the experimental data in which the vehicle performed various maneuvers. The steer relation is identified based on the Ackermann steering angle with nonlinear least-squares fitting. For positive steering angles, 8110 data points are available, and the root-mean-squared error of the fit is 0.018 rad (1.03°). For negative steering angles, 1488 data points are available, and a fit with a root mean squared error of 0.017 rad (0.95°) is obtained.

- Nonlinear least-squares curve-fitting is applied to determine the directional tire stiffness of the front and rear tires, as well as the friction coefficient. The obtained root-mean-squared error for the rear wheels is 0.58 N, based on 7176 data points. The fit of the front wheel yield a root-mean-squared error is 0.17 N, based on 6797 data points.
- Based on the validation with experimental data, it is concluded that modifications to the tire model are required. Increasing the friction coefficient and decreasing the force coupling effect of the model yields an accurate description of validation data. With the proposed modification, the dynamics of the scaled vehicle are closely approximated.

Chapter 5

Steady-State Equilibrium Analysis

So far, the previous chapters have focused on establishing a model that accurately describes the dynamics of the scaled vehicle. This chapter studies the advantages of drifting over normal driving under steady-state conditions. The purpose of this chapter is to deepen the understanding of the differences between normal driving and drifting.

The equilibria of the system are discussed in 5-1. The stability of these points is analyzed through the construction of the phase portraits in section 5-2. In order to comment on the controllability of the equilibria, an analysis based on the Controllability Grammian is discussed in section 5-3. Section 5-4 concludes with an overview of the findings.

5-1 System Equilibria

Starting from the equations of motions, one can analyze the steady-state behavior of the system by setting the state derivatives equal to zero. The authors of [12] showed that this approach allows to find the steady-state cornering equilibria of a vehicle. Three types of cornering can be identified. As was discussed in the introduction (Chapter 1), vehicle motion can be categorized by the side-slip angle β. The analysis of this chapter considers two groups:

- $\beta \geq 0$ Normal driving equilibria
- $\beta < 0$ Drift equilibria

In order to differentiate based on the side-slip angle, the expression of the single-track model of (2-24) is used in this chapter.

$$\dot{u} = \frac{1}{m} 2F_{x,R} + ru\beta \tag{5-1}$$

$$\dot{\beta} = \frac{1}{mu} \left(\sum F_{y,F} + F_{y,R} \right) - r \tag{5-2}$$

$$\dot{r} = \frac{1}{I_z} \left(\sum l_F F_{y,F} - \sum l_R F_{y,R} \right) \tag{5-3}$$

To find the steady-state equilibria, the system inputs and side-slip angle that bring the state derivatives to zero need to be obtained. A nonlinear least-squares problem is formulated that is solved using the nonlinear optimization toolbox of MATLAB.

$$\min_{\delta, F_{x,R}, \beta} \left\| \begin{bmatrix} \dot{u} & \dot{\beta} & \dot{r} \end{bmatrix}^T \right\|_2^2 \tag{5-4}$$

The tire forces are computed using the identified Dugoff model of the previous chapter. The modifications that were proposed in section 4-3 is also incorporated. The nonlinear least squares problem (5-4) is solved for a range of cornering radii and velocities. In order to find the normal equilibria, the initial variables are defined as $\delta_0 = \frac{\pi}{18}$ rad (10°), $F_{x,R,0} = 0$ N, $\beta_0 = 0$ rad. The values corresponds to the motion that is expected for the normal equilibria; low tire forces and a positive steering angle. In case of the drift equilibria, negative side-slip angles combined with negative steering angles and tire saturation is expected. Therefore the initial values are in this case defined as: $\delta_0 = \frac{\pi}{18}$ rad (10°), $F_{x,R,0} = 2$ N, $\beta_0 = -\frac{\pi}{6}$ rad (−30°). Starting from the initial values, the non-linear least squares algorithm converges to the equilibria by minimizing (5-4).

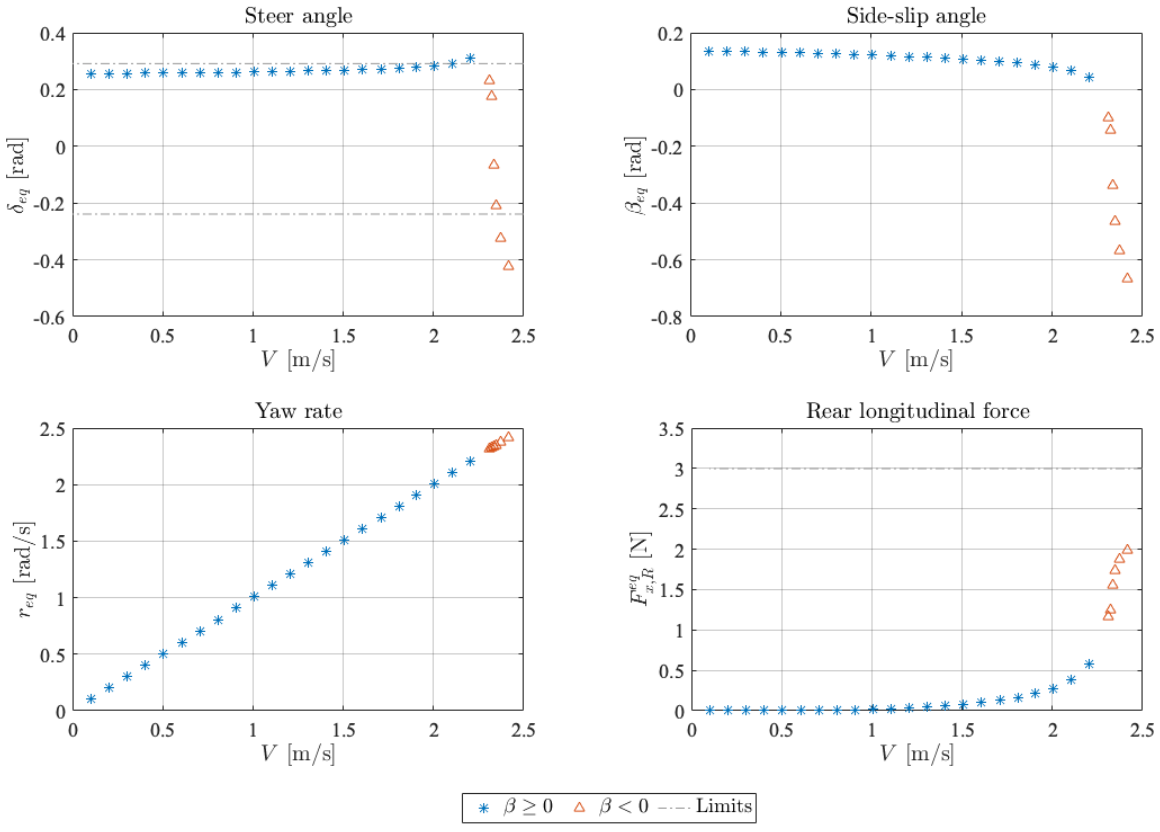

Figure 5-1: System equilibria for a 1-meter radius left-hand corner. Equilibria with a positive side-slip angle are indicated by the blue asterisks, the red triangles represent drift equilibria.

An overview of the equilibria for a 1-meter radius left-hand corner is displayed in Figure 5-1. The distinction is made between equilibria with a zero or positive body side-slip angle (blue

asterisks) and equilibria with a negative side-slip angle (red triangles). The equilibria are plotted for increasing velocity along the corner curvature, which is defined as:

$$V = \sqrt{(u)^2 + (v)^2}. \tag{5-5}$$

What stands out is the relationship between the cornering velocity and the steering angle. For velocities up to 2 m/s the steering angle gradually increases. After this point, the relationship is nonlinear. When the cornering velocity is further increased, the equilibrium steering angle decreases and eventually becomes negative. The vehicle is drifting at this point, indicated by the negative body side-slip angles and saturated rear tires. Interesting to note that the highest yaw rates can be obtained at the negative side-slip equilibria.

5-2 Phase Portraits

Finding the system equilibria is one, but it does not provide any information about the stability at and around these points. Insights into the stability of the equilibria can be obtained through the computation of the phase portraits. The system is linearized at an equilibrium, and the system responses following from small perturbations with respect to the equilibrium state values are analyzed. In the current form, the Dugoff tire model consists of a discontinuity (2-7). This prevents from directly linearizing the vehicle model. The discontinuity in $f(\zeta)$ is displayed in Figure 5-2. A continuous approximation of $f(\zeta)$ is constructed following the approach that is presented in [32].

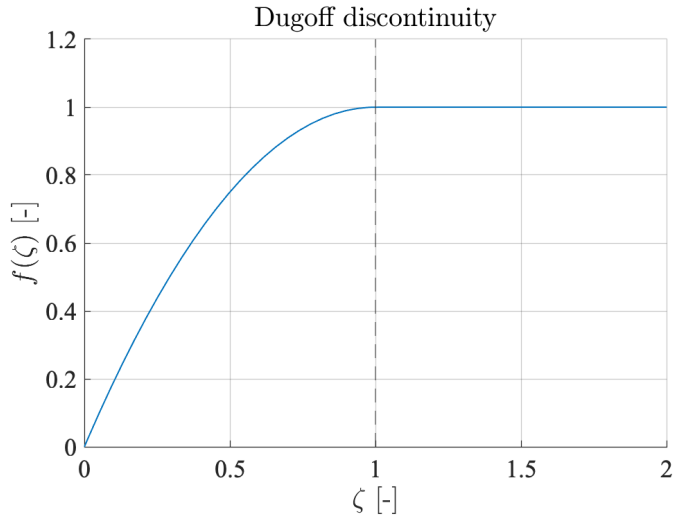

Figure 5-2: Discontinuity of the Dugoff Tire Model: $f(\zeta)$ versus ζ.

Following this method, the discontinuous function $f(\zeta)$, over the domain $\left[\zeta_0, \zeta_f\right]$, can be divided into two continuous functions Ψ_0 and Ψ_1.

$$\Psi_0 = \zeta\,(2 - \zeta) \tag{5-6}$$
$$\Psi_1 = 1 \tag{5-7}$$

The domain of $f(\zeta)$ is split into two partition domains by the discontinuity point $\zeta_1 = 1$. In the first partition interval $[\zeta_0, \zeta_1]$, $f(\zeta)$ is described by Ψ_0, in the second partition interval $\left[\zeta_1, \zeta_f\right]$ by Ψ_1. The approximation $\Omega(\zeta)$ of $f(\zeta)$ over the whole domain $\left[\zeta_0, \zeta_f\right]$ is formulated as:

$$\Omega(z) = F_0(\zeta) + F_1(\zeta)\chi(\zeta, \zeta_1), \tag{5-8}$$

where $\chi(y, \zeta_1)$ represents a connection function at the discontinuity point ζ_1.

$$\chi(\zeta, \zeta_1) = \tanh\left[\left[\left(\frac{\zeta - \zeta_0}{\zeta_f - \zeta_0}\right)^2 \left(\frac{\zeta - z_1}{\zeta_f - \zeta_0}\right)\left(\frac{\zeta_f - \zeta}{\zeta_f - \zeta_0}\right)^2\right]^{-1}\right] \tag{5-9}$$

Furthermore, $F_0(z)$ and $F_1(z)$ are auxiliary functions obtained from solving the linear system of equations:

$$\begin{bmatrix} S_{0,0} & S_{0,1} \\ S_{1,0} & S_{1,1} \end{bmatrix} \begin{bmatrix} F_0(\zeta) \\ F_1(\zeta) \end{bmatrix} = \begin{bmatrix} \Psi_0(\zeta) \\ \Psi_1(\zeta) \end{bmatrix}. \tag{5-10}$$

The coefficients $S_{0,1}$ and $S_{0,1}$ represent the average values of the connecting function χ over the partition intervals, $[\zeta_0, \zeta_1]$ and $\left[\zeta_1, \zeta_f\right]$ respectively.

$$S_{0,0} = 1 \tag{5-11}$$
$$S_{1,0} = 1 \tag{5-12}$$
$$S_{0,1} = \frac{1}{\zeta_1 - \zeta_0} \int_{\zeta_0}^{\zeta_1} \chi(\zeta, \zeta_1)\zeta \tag{5-13}$$
$$S_{1,1} = \frac{1}{\zeta_f - \zeta_1} \int_{\zeta_1}^{\zeta_f} \chi(\zeta, \zeta_1)\zeta \tag{5-14}$$

The resulting approximation is displayed in Figure 5-3. The Variance Accounted For (VAF) is 100% and the Root Mean Squared Error (RMSE) is 1.09e-16. It is concluded that the approach successfully constructs an continuous function $\Omega(\zeta)$ that approximates the Dugoff term $f(\zeta)$.

Now that the model can be linearized, two specific equilibria are studied for a 1-meter radius left-hand corner (Figure 5-4).

- Normal equilibrium
  The vehicle is driving at a cornering velocity of $V = 1.71$ m/s. The sideslip angle is positive ($\beta = 0.10$ rad), similar to the steering angle ($\delta = 0.27$ rad).
- Drift equilibrium
  The cornering velocity is increased to $V = 2.35$ m/s. The motion is now characterized by a negative side-slip angle ($\beta = -0.46$ rad) and and a negative steering angle ($\delta = -0.21$ rad).

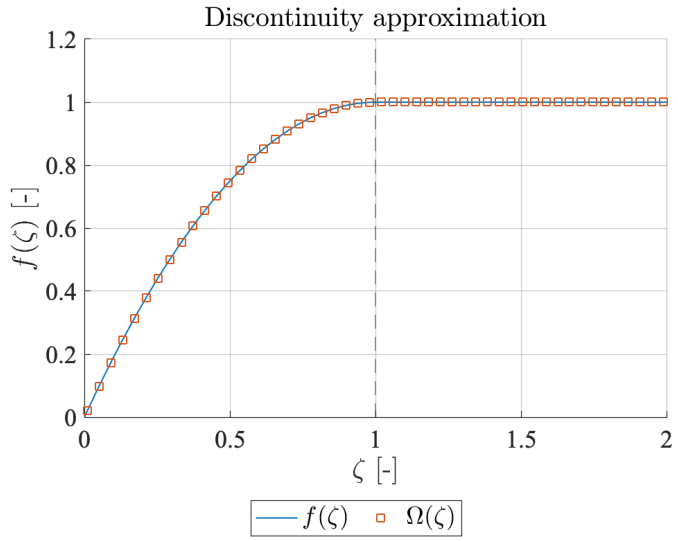

Figure 5-3: Comparison between the original the discontinuity of the Dugoff Tire Model $f(\zeta)$ and the approximation $\Omega(\zeta)$.

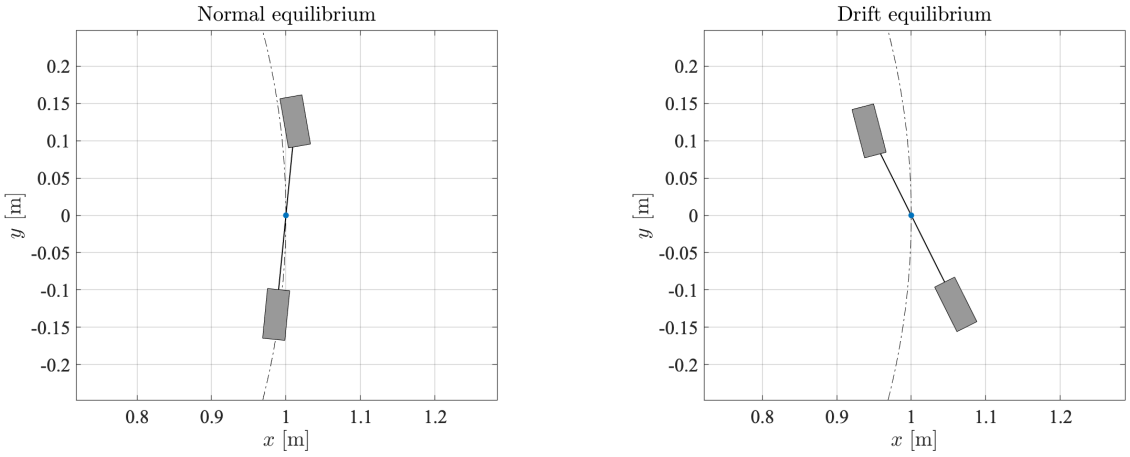

Figure 5-4: Bird-view perspective of two cornering equilibria for a 1-meter radius left-hand corner.

For both the equilibria, normal and drift, the phase portraits are constructed. The equilibrium values of the side-slip angle and raw rate are perturbed, and the response of the linearized system resulting from the perturbed states is computed. Combining all the responses for a range of perturbations results in the phase portraits of Figure 5-5.

From the phase portraits, it is observed that for the normal equilibrium, all the responses return to the calculated equilibria (indicated by the red dot). Where this equilibrium thus is a stable equilibrium, the drift corner is found to be an unstable saddle point. When perturbed, the state trajectories move away from the equilibrium.

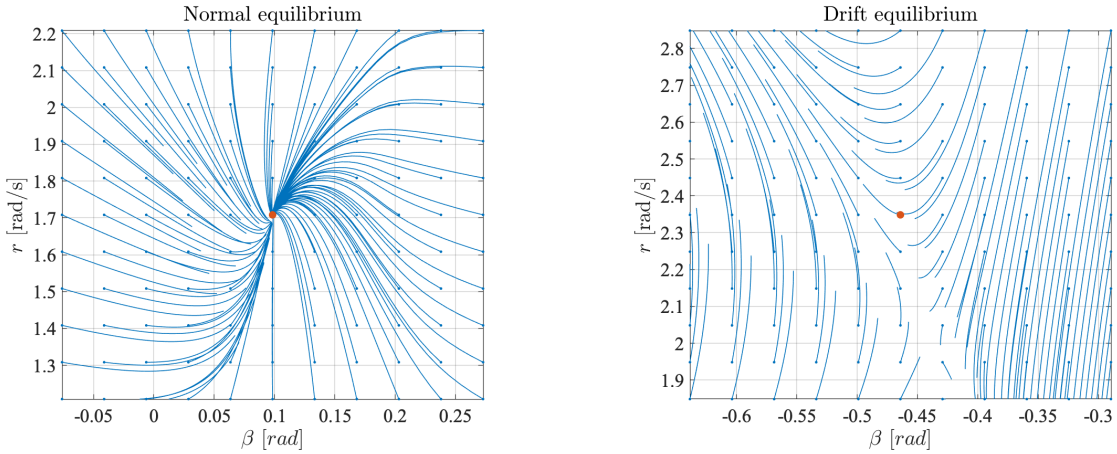

Figure 5-5: Phase portraits of two cornering equilibria for a 1-meter radius left-hand corner. The body side-slip angle and yaw rate are perturbed from β_{eq} and r_{eq}. The red dot indicates the equilibrium point.

5-3 Controllability Grammians

To obtain more information regarding the controllability of the equilibria, the controllability matrices are computed. All equilibria are found to be controllable, based on the observation that the controllability matrix has full row rank. To get a broader understanding, rather than the binary statement of controllability, an approach based on the Controllability Grammian is proposed.

If the linearized has an A-matrix that is Routh Hurwitz, the Controllability Grammian C_G is obtained from solving the following Lyapunov equation.

$$C_G = \int_0^\infty e^{At} B B^T e^{A^T t} dt \tag{5-15}$$

$$AC_G + C_G A^T = -BB^T \tag{5-16}$$

For the linearized systems where the A is non-Hurwitz, the Controllability Grammian is computed differently. Under the assumption that A has no eigenvalues on the imaginary axis, the transformation T is used to decouple the system [25].

$$\begin{bmatrix} TAT^{-1} & TB \\ CT^{-1} & 0 \end{bmatrix} = \begin{bmatrix} A_1 & 0 & B_1 \\ 0 & A_2 & B_2 \\ C_1 & C_2 & 0 \end{bmatrix} \tag{5-17}$$

In this decoupled system A_1 is stable and A_2 is anti-stable. Based on the structure of (5-17), two individual Lyapunov functions are solved (5-18). The Controllability Grammian C_G is now formed from the solutions to these Lypunoc equations and the transformation matrix T (5-20).

$$A_1P_1 + P_1A_1^T + B_1B_1^T = 0 \tag{5-18}$$
$$A_2P_2 + P_2A_2^T + B_2B_2^T = 0 \tag{5-19}$$

$$C_G = T^{-1}\begin{bmatrix} P_1 & 0 \\ 0 & P_2 \end{bmatrix}\left(T^{-1}\right)^T \tag{5-20}$$

The eigenvalues and eigenvectors of the Controllability Grammian contain information about the controllability. The eigenvectors corresponding to a normal and a drift equilibrium are displayed in Figure 5-6. The direction of the eigenvector ξ_i, corresponding to the largest eigenvalue λ_i, is the direction in which the system is most controllable [43].

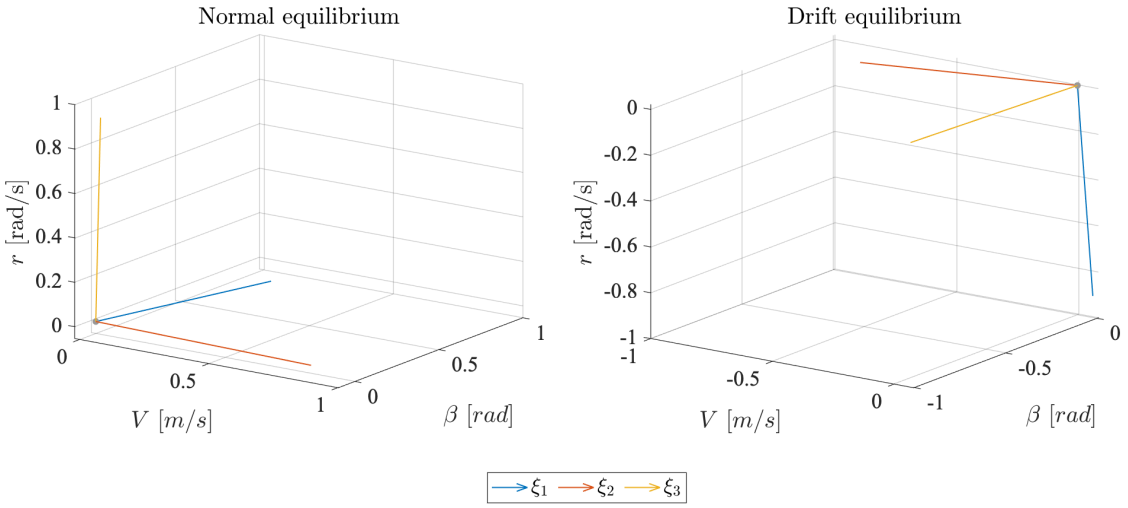

Figure 5-6: Eigenvectors of the Ccontrollability Grammian for a 1-meter radius left-hand corner.

The eigenvalue λ_i thus indicates how easy the system can be controlled in the corresponding direction ξ_i. When the eigenvalues are approximately the same size, it requires roughly the same input energy to control the system in the direction of each eigenvector. If there is a large difference in eigenvalues, the controllability in each of the directions varies significantly. Note that the system still can be steered in each direction; it merely will require more input energy to move into some directions.

Consider the example of a supermarket pushcart. Imagine that the caster wheels are fixed such that the cart can move freely in the longitudinal direction. In this situation, it is easy to move the vehicle longitudinally. However, the force that is required to move the cart in the lateral direction is significantly bigger. For a specified amount of force, the displacement that can be achieved in the longitudinal direction is larger than in the lateral direction. Furthermore, the ratio of the eigenvalues provides information about the robustness of the system. In the example of the pushcart, lateral movement can be achieved by applying a large force. When this force is applied with an offset (under a small angle), the longitudinal component of the force will yield large longitudinal displacement as a result of the difference

in resistance. When there is a dominant eigenvalue, the system can be subject to robustness issues in the direction of the other eigenvectors.

The ratio between the lowest and the highest eigenvalue of the controllability is computed. For a specific equilibrium, it indicates how close the degree of controllability in each direction is. The results for the left-hand, 1 meter radius corner are shown in Figure 5-7. The ration is defined as $\frac{\lambda_{min}}{\lambda_{max}}$. As smaller ratios are observed for normal equilibria, it is concluded that the difference between the eigenvalues is larger at these points. The degree to which there exist a dominant direction is lower for drift equilibria. It is assumed that, during a drift, it is easier to steer the system in the direction of each eigenvector ξ_i.

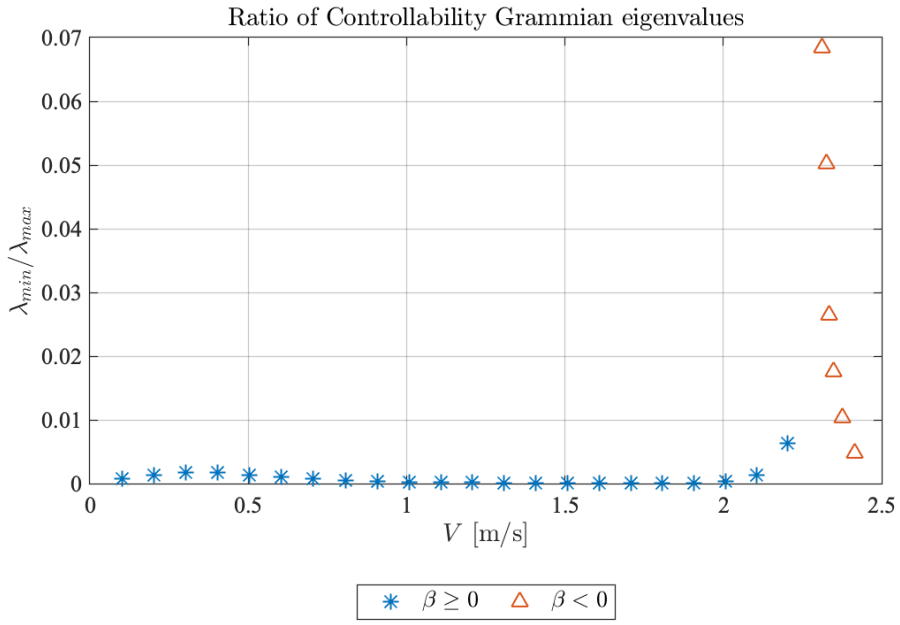

Figure 5-7: Visualization of the eigenvectors of the Controllability Grammian for two equilibria for a 1-meter radius left-hand corner.

5-4 Conclusions

This chapter studies the advantages that drifting poses on vehicle maneuverability under the assumption of steady-state conditions. The analysis specifically focuses on the identified model of the scaled vehicle. The most important findings are presented in this section.

- Compared to normal equilibria, drifting equilibria are characterized by higher cornering velocities and higher yaw rates. Additionally, the rear tires are at the saturation limit. The concept of force coupling implies increased controllability of the vehicle during a drift.
- From the phase portraits, it is concluded that drifting is an unstable equilibrium, normal equilibria are found to be stable. While the vehicle will converge towards a normal equilibrium, it is more challenging to maintain the drift motion.

- The Controllability Grammian revealed that during drifting, the ratio of the eigenvalues is smaller compared to normal equilibria. A small ratio indicates that there is a main direction of response, and other directions are subject to robustness issues.

Chapter 6

Dynamic Trajectory Optimization

In chapter 5, the benefits of drifting were derived under steady-state conditions. The remaining research question is whether the same benefits become apparent in a dynamic driving scenario. This chapter describes the driving scenario and explains how to formulate this scenario in an optimization problem.

Section 6-1 present the scenario and elaborates on the assumptions that are made. Section 6-2 explains how this driving scenario is written into a multi-objective optimization problem. Section 6-3 introduces the structure that is used to solve the optimization. The conclusions are formulated in Section 6-4.

6-1 Single Corner Scenario

The focus is narrowed to a single corner scenario. The vehicle should negotiate a $\frac{\pi}{2}$ rad (90°) corner. At the start and the end of the maneuver, the vehicle should be in a stable driving situation. A schematic overview of the maneuver is presented in Figure 6-1. The desired trajectory is an arc with constant radius R, and the center located at (x_c, y_c). The vehicle is initially driving in a straight line, with an initial velocity V_{init}. The initial steering angle is 0 rad, the yaw rate and side-slip rate at the start and end time should be equal to 0 rad/s

The single-corner scenario is selected since it captures the relevant aspects of driving. The maneuver starts with steady-state conditions. When the vehicle steers into the corner transient motion is observed, and eventually, steady-state cornering is reached. At the end of the corner, the vehicle returns to steady-state driving through another segment of transient motion. The advantage of this maneuver lies in the close resemblance with the identified cornering equilibria of chapter 5. The vehicle is expected to reach steady-state cornering along the corner. Through variation the desired cornering velocity, specific steady-state cornering equilibria can be matched.

Assumptions
Before the optimization problem can be formulated, the boundaries need to be defined. This

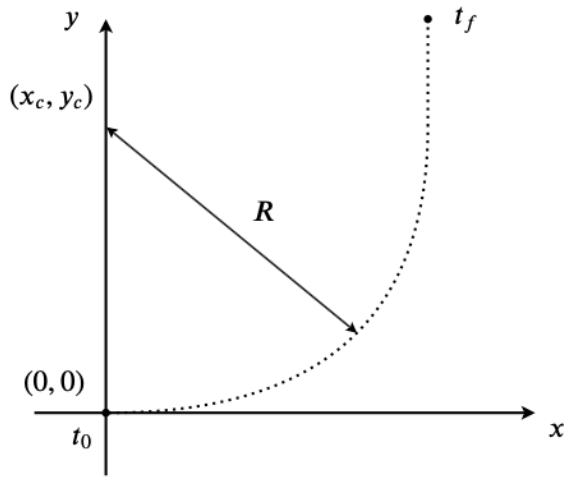

Figure 6-1: Schematic representation of the dynamic driving scenario.

section serves that purpose. Concerning the dynamic driving scenario, the following assumptions are made.

- *Constant μ is assumed during the maneuver*
  In reality, the amount of friction between the tire and the road surface will constantly change. Throughout the optimization, the friction (unless stated differently) will be equal to the value obtained in chapter 4. As this coefficient is estimated based on multiple experiments, it is considered to be an accurate estimation to simulate maneuvers that correspond to real-life experiments performed with the scaled vehicle.

- *Longitudinal wheel dynamics neglected*
  It is assumed that there is no longitudinal wheel slip since the main focus is to study the lateral dynamics. The rotational velocity of the tire is considered to be equal to the velocity of the wheel hub. The identified Dugoff model is slightly modified to account for this simplification. In the absence of longitudinal slip λ, the effect of tire force coupling is included through the use of derating factor η [20].

$$\eta = \frac{\sqrt{(\mu F_z)^2 - F_x^2}}{\mu F_z} \tag{6-1}$$

  As the longitudinal force increases, η decreases from 1 to 0. The scenario in which $\eta = 0$ corresponds to the situation where the total attainable tire force is applied in the longitudinal direction. The lateral tire force is then calculated as:

$$F_y = C_\alpha \tan(\alpha)\, f(\zeta) \tag{6-2}$$

$$f(\zeta) = \begin{cases} \zeta\,(2-\zeta) & \text{if } \zeta < 1 \\ 1 & \text{else} \end{cases} \tag{6-3}$$

$$\zeta = \eta \mu F_z \frac{1}{2\sqrt{\left(C_\alpha \tan(\alpha)\right)^2}}. \tag{6-4}$$

- *Limits are imposed on steering*
  To make sure that the result of the optimization is a close representation of the dynamics of the scaled vehicle, limits are imposed on the steering mechanism. It must be noted that the limits of the steering servo are not exactly copied. The vehicle is currently equipped with a standard steering servo. Better hardware is expected to yield larger steering range and rate. Therefore, some margin is incorporated in the limits. The maximum steering angle is $\frac{\pi}{6}$ rad (30°), the maximum steering rate is $\frac{10\pi}{3}$ rad/s (600°/s). This rate corresponds to a steering mechanism that is capable of moving from one end of the steering range to the other in 0.1 s.

$$-\frac{\pi}{6}\ \text{rad} \leq \delta \leq \frac{\pi}{6}\ \text{rad} \tag{6-5}$$

$$-\frac{10\pi}{3}\ \text{rad/s} \leq \dot{\delta} \leq \frac{10\pi}{3}\ \text{rad/s} \tag{6-6}$$

6-2 Formulation of the Multi-Objective Optimization Problem

The driving scenario is schematically displayed in Figure 6-2. The goal of the optimization is to find the inputs that make the vehicle track the dotted curved trajectory. In a standard vehicle, one can control the steering and the throttle. In this work, the steering rate $\dot{\delta}$ and the longitudinal force on the rear wheels $F_{x,R}$ are considered to be the input signals. The selection of the steering rate $\dot{\delta}$ is motivated by the practical benefit that it allows for defining limits on the steering rate. The optimization is solved for a fixed end time t_f. The time domain is discretized with the fixed time step $(t_{k-1} - t_k)$ of 0.05 s. Furthermore, the maneuver is divided into two segments. In the first segment $t_0 \leq t \leq t_1$, the vehicle negotiates the corner. The time instance t_1 is determined based on the satisfaction of the condition $\psi + \beta \geq \frac{\pi}{2}$ rad (90°). After that point, for $t_1 > t \geq t_f$, the cost-function is defined such that the vehicle drives a straight line.

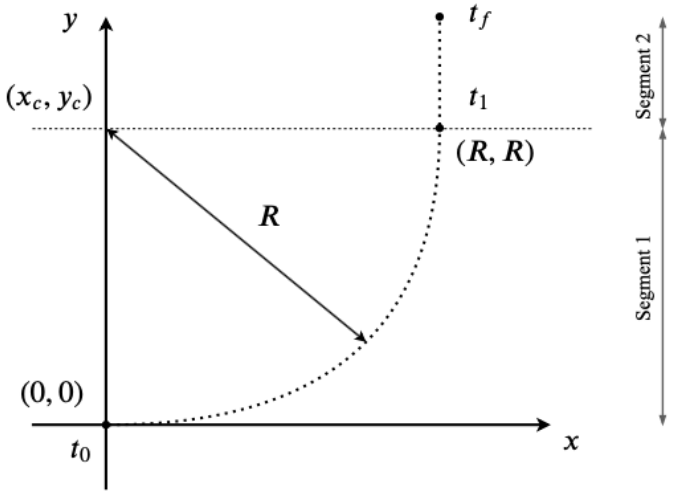

Figure 6-2: Schematic representation of the optimization. The maneuver is split into two segments: cornering ($t_0 \leq t \leq t_f$) and straight line driving ($t_1 \leq t \leq t_f$).

The performance of the vehicle is evaluated using on a cost-function. Based on the desired vehicle motion, four relevant terms are identified. The physical meaning of the cost-function terms varies. However, each term consists of a variable the quantifies the difference between the observed and desired motion. The time vector is described by the vector $\mathbf{t} \in \mathbb{R}^{N\times 1}$. As a result, the errors will be vectors that have the same dimension as the time vector, $\mathbf{e} \in \mathbb{R}^{N\times 1}$. Suppose that the time vector is divided into the segments $t_0 \leq t \leq t_1 \in \mathbb{R}^{n\times 1}$ and $t_1 < t \leq t_f \in \mathbb{R}^{(N-n)\times 1}$. A weight matrix $\mathbf{W}$ is constructed that contains the individual weights w_i (6-7). These weights determine the importance of the error at time step t_i to the total cost-function.

$$\mathbf{W} = \left[\begin{array}{ccccc:ccccc} w_1 & 0 & \dots & 0 & 0 & & & & & \\ 0 & w_2 & \dots & 0 & 0 & & & & & \\ \vdots & \vdots & \ddots & \vdots & \vdots & & & \mathbf{0} & & \\ 0 & 0 & \dots & w_{n-1} & 0 & & & & & \\ 0 & 0 & \dots & 0 & w_n & & & & & \\ \hdashline & & & & & w_{n+1} & 0 & \dots & 0 & 0 \\ & & & & & 0 & w_{n+2} & \dots & 0 & 0 \\ & & \mathbf{0} & & & \vdots & \vdots & \ddots & \vdots & \vdots \\ & & & & & 0 & 0 & \dots & w_{N-1} & 0 \\ & & & & & 0 & 0 & \dots & 0 & w_N \end{array}\right] \tag{6-7}$$

This section defines the cost-function of the optimization. For each of the cost-function terms, the relevance concerning the optimization goal is discussed. Furthermore, a brief description of how the terms depend on the available inputs is added. An extensive elaboration of this dependency, based on the dynamics of the model, can be found in appendix C. Finally, for each term, the mathematical expression will be derived.

Position

Based on the desired trajectory, the reference position of the vehicle at each time instance t_k can be computed. Any error from the desired position means that the vehicle is not negotiating the corner at the reference trajectory. The presented system equilibria (Chapter 5) are computed under the assumption of a constant cornering radius. In order to make a valid comparison with these equilibria, the curvature $\left(\kappa = \frac{1}{R}\right)$ of the vehicle must approximate the curvature of the equilibria as close as possible.

Before deriving the formula of the error signals, it is relevant to consider how the available input signals could influence the position of the vehicle. In this section, the position of the vehicle is defined in the inertial coordinate frame ($x_{inertial}$,$y_{inertial}$). The position of the vehicle in the inertial and the body-orientated reference frame are directly related to each other (2-1). Since it is more convenient to explain the vehicle dynamics in the body-orientated frame, the explanation will focus on the longitudinal and lateral position instead of the inertial position. Both inputs $\dot{\delta}$ and $F_{x,R}$ can alter the position of the vehicle. Changing the steering rate will yield in a different heading angle. The other input, the longitudinal force of the rear tire, obviously can change the position in the longitudinal direction of the vehicle. In the particular scenario of tire saturation, the longitudinal force can also change the lateral force

that is generated. This allows for changing the lateral position of the vehicle through $F_{x,R}$ as well.

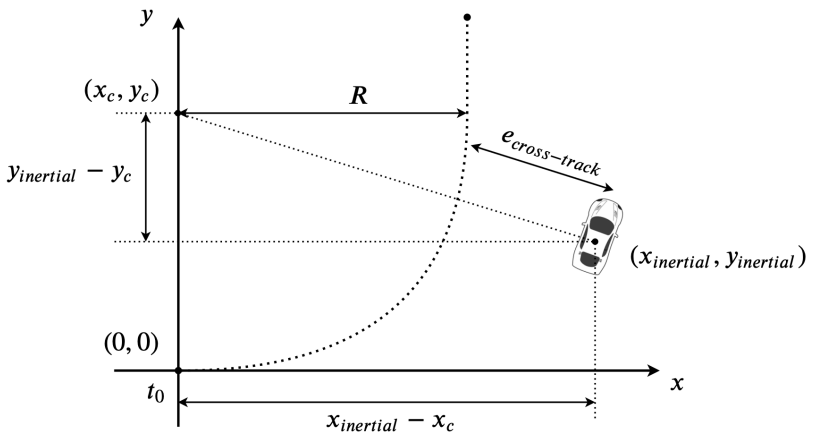

Figure 6-3: Schematic overview of the cross-track error between the position of the vehicle and the reference velocity.

The error of the position is determined by the cross-track error (Figure 6-3). It defines the shortest distance between the location of the vehicle and the reference trajectory. For implementation purposes, two different definitions are used. In the first segment, cross-track error is computed as $\mathbf{e}_{pos,1}$ (6-8). It defines the difference between the desired radius of the corner and the radius that the vehicle is driving with respect to the center of the corner (x_c, y_c). The weight matrix $\mathbf{W}_{pos,1}$ is defined such that this expression only applies to the first segment.

$$\mathbf{e}_{pos,1} = \sqrt{(\mathbf{x}_{inertial} - x_c)^2 + (\mathbf{y}_{inertial} - y_c)^2} - R \tag{6-8}$$

$$\mathbf{W}_{pos,1} = \begin{bmatrix} 1 & 0 & \dots & 0 & 0 & \\ 0 & 1 & \dots & 0 & 0 & \\ \vdots & \vdots & \ddots & \vdots & \vdots & \mathbf{0} \\ 0 & 0 & \dots & 1 & 0 & \\ 0 & 0 & \dots & 0 & 1 & \\ \hline & & \mathbf{0} & & & \mathbf{0} \end{bmatrix}. \tag{6-9}$$

In the second segment, when $\psi + \beta \geq \frac{\pi}{2}$ rad (90°), the vehicle needs to drive in a straight line. The cross-track error in this segment can be described as the lateral deviation from the trajectory. The error $\mathbf{e}_{pos,2}$ is defined as the difference between the inertial position $(x_{inertial})$ and the cornering radius R. The mathematical expression of $\mathbf{e}_{pos,2}$ and the corresponding weight matrix $\mathbf{W}_{pos,2}$ are:

$$\mathbf{e}_{pos,2} = \mathbf{x}_{intertial} - R \tag{6-10}$$

$$\mathbf{W}_{pos,2} = \left[\begin{array}{c:cccc} \mathbf{0} & \multicolumn{4}{c}{\mathbf{0}} \\ \hdashline \multirow{5}{*}{$\mathbf{0}$} & 1 & 0 & \dots & 0 & 0 \\ & 0 & 1 & \dots & 0 & 0 \\ & \vdots & \vdots & \ddots & \vdots & \vdots \\ & 0 & 0 & \dots & 1 & 0 \\ & 0 & 0 & \dots & 0 & 1 \end{array}\right]. \tag{6-11}$$

The cost-function term accounting for the position of the vehicle can then be written as (6-12). To make sure that all terms of the total cost-function are equally important, the individual terms will be scaled based on the expected domain of the error terms. The scaling of the position term is based on an average position error of 0.1 m. With the dimension of the time vector $\mathbf{t} \in \mathbb{R}^{N\times 1}$, the scale factor equals $\frac{1}{0.1\cdot N}$. Here, N is the length of the discrete-time vector.

$$J_{pos} = \frac{1}{0.1\cdot N}\left(\mathbf{e}_{pos,1}^T \mathbf{W}_{pos,1}\mathbf{e}_{pos,1} + \mathbf{e}_{pos,2}^T \mathbf{W}_{pos,2}\mathbf{e}_{pos,2}\right) \tag{6-12}$$

Velocity

The second term in the cost-function is the cornering velocity of the vehicle, which is essential since this was found to be a differentiator between normal and drifting equilibria (Chapter 5). When the desired velocity is not accurately tracked, the vehicle is negotiating the corner at a different equilibrium.

The cornering velocity can be changed through both inputs. The rear longitudinal force is related to the cornering velocity, as it directly changes the longitudinal velocity. Varying the steering angle with a constant throttle input introduces tire slip and therewith friction, which also changes the cornering velocity.

The error between the reference velocity and the actual velocity of the vehicle is denoted by $\mathbf{e}_V$ (6-13). The vehicle should maintain the reference velocity over the full duration of the maneuver, thus during both time segments. Therefore, the weight matrix $\mathbf{W}_V$ is equal to the identity matrix with dimension $\mathbb{R}^{N\times N}$.

$$\mathbf{e}_V = \mathbf{V} - V_{ref} \tag{6-13}$$

$$\mathbf{W}_V = \left[\begin{array}{ccccc:ccccc} 1 & 0 & \dots & 0 & 0 & & & & & \\ 0 & 1 & \dots & 0 & 0 & & & & & \\ \vdots & \vdots & \ddots & \vdots & \vdots & & & \mathbf{0} & & \\ 0 & 0 & \dots & 1 & 0 & & & & & \\ 0 & 0 & \dots & 0 & 1 & & & & & \\ \hdashline & & & & & 1 & 0 & \dots & 0 & 0 \\ & & & & & 0 & 1 & \dots & 0 & 0 \\ & & \mathbf{0} & & & \vdots & \vdots & \ddots & \vdots & \vdots \\ & & & & & 0 & 0 & \dots & 1 & 0 \\ & & & & & 0 & 0 & \dots & 0 & 1 \end{array}\right] \tag{6-14}$$

The average velocity error is estimated to be equal to 0.1 m/s. With an error $\mathbf{e}_V$ of dimension $\mathbb{R}^{N\times 1}$, the scaling of the velocity term equals $0.1 \cdot N$ (6-15). Again, N is the length of the discrete time vector.

$$J_V = \frac{1}{0.1 \cdot N}\left(\mathbf{e}_V^T \mathbf{W}_V \mathbf{e}_V\right) \tag{6-15}$$

Yaw rate

The requirements on the yaw rate only apply to the initial and final conditions. To guarantee that the vehicle is in a stable driving situation at these time instance, the desired yaw rate at the beginning and end of the maneuver is zero.

The steering rate changes the yaw rate since it alters the steering angle and therewith the lateral force of the front tire. As was described in the position section, the rear longitudinal force affects the yaw rate through rear tire force coupling when the tire is saturated.

Since the desired value of the yaw rate at the two-time instances is zero, the vector $\mathbf{e}_r$ is defined as (6-16). The weight matrix $\mathbf{W}_r$ only has nonzero entries at the top left and bottom right positions, corresponding to the yaw error at initial (t_0) and final time (t_f).

$$\mathbf{e}_r = \mathbf{r} \tag{6-16}$$

$$\mathbf{W}_r = \left[\begin{array}{ccccc:ccccc} 1 & 0 & \dots & 0 & 0 & & & & & \\ 0 & 0 & \dots & 0 & 0 & & & & & \\ \vdots & \vdots & \ddots & \vdots & \vdots & & & \mathbf{0} & & \\ 0 & 0 & \dots & 0 & 0 & & & & & \\ 0 & 0 & \dots & 0 & 0 & & & & & \\ \hdashline & & & & & 0 & 0 & \dots & 0 & 0 \\ & & & & & 0 & 0 & \dots & 0 & 0 \\ & & \mathbf{0} & & & \vdots & \vdots & \ddots & \vdots & \vdots \\ & & & & & 0 & 0 & \dots & 0 & 0 \\ & & & & & 0 & 0 & \dots & 0 & 1 \end{array}\right] \tag{6-17}$$

As will be explained in the following section, the model that is used in the optimization consists of integrator-blocks that allow for defining the initial conditions. Therefore, the yaw rate at t_0 can be set equal to zero. The total error $\mathbf{e}_r$ is thus completely determined by the yaw rate at time t_f. In the optimization, the vehicle needs to make a $\frac{\pi}{2}$ rad (90°) corner within a time frame of 1 s. The average yaw rate that will be observed should therefore equals $\frac{\pi}{2}$rad/s (90 °/s). This value is used to scale the cost-function term J_r:

$$J_r = \frac{2}{\pi}\left(\mathbf{e}_r^T \mathbf{w}_r \mathbf{e}_r\right). \tag{6-18}$$

Side-slip rate

Similar to the conditions imposed on the yaw rate, the requirements for the side-slip rate only apply to two-time instances. At the start of the maneuver, the vehicle is expected to be dynamically stable, therefore having zero side-slip rate. The other requirement is that the side-slip rate is zero at the end of the corner, at the inertial position $(x_{inertial}, y_{inertial}) = (R, R)$. This is motivated by the idea that a zero side-slip rate at the end of the corner stimulates steady-state cornering. This would make for a better comparison with the previously obtained equilibria, which are also based on the assumption of steady-state cornering.

The side-slip rate is dependent on the lateral and longitudinal velocity of the vehicle. It is evident that the side-slip rate is controllable through both inputs. The side-slip rate is a function of the longitudinal velocity, the lateral velocity, and their time derivatives. The steering rate can influence the lateral dynamics. The longitudinal can logically alter the longitudinal velocity; however, through force coupling also the lateral velocity.

The side-slip rate error vector $\mathbf{e}_{\dot{\beta}}$ is equal to the discrete model output $\dot{\beta}$. The corresponding weight matrix $\mathbf{W}_{\dot{\beta}}$ only has entries that equal 1 at the first and last time instance of the first segment ($t_0 \leq t \leq t_1$).

$$\mathbf{e}_{\dot{\beta}} = \dot{\beta} \tag{6-19}$$

$$\mathbf{W}_{\dot{\beta}} = \left[\begin{array}{ccccc:c} 1 & 0 & \dots & 0 & 0 & \\ 0 & 0 & \dots & 0 & 0 & \\ \vdots & \vdots & \ddots & \vdots & \vdots & \mathbf{0} \\ 0 & 0 & \dots & 0 & 0 & \\ 0 & 0 & \dots & 0 & 1 & \\ \hdashline & & \mathbf{0} & & & \mathbf{0} \end{array}\right] \tag{6-20}$$

The estimation of the side-slip rate scaling coefficient is set equal to the value that was derived for the yaw rate. This yields the following cost-function term:

$$J_{\dot{\beta}} = \frac{2}{\pi}\left(\mathbf{e}_{\dot{\beta}}^T \mathbf{W}_{\dot{\beta}} \mathbf{e}_{\dot{\beta}}\right). \tag{6-21}$$

General Optimization Problem

The total cost-function is equal to the summation of the scaled individual terms. Given a time vector $\mathbf{t} \in \mathbb{R}^{N\times 1}$, the expressed reads as:

$$J = q_{pos} \cdot J_{pos} + q_V \cdot J_V + q_r \cdot J_r + q_{\dot{\beta}} \cdot J_{\dot{\beta}} \tag{6-22}$$

$$= q_{pos} \cdot \tfrac{1}{0.1\cdot N} \left(\mathbf{e}_{pos,1}^T \mathbf{W}_{pos,1} \mathbf{e}_{pos,1} + \mathbf{e}_{pos,2}^T \mathbf{W}_{pos,2} \mathbf{e}_{pos,2} \right) + \tag{6-23}$$

$$q_V \cdot \tfrac{1}{0.1\cdot N} \left(\mathbf{e}_V^T \mathbf{W}_V \mathbf{e}_V \right) + q_r \cdot \tfrac{2}{\pi} \left(\mathbf{e}_r^T \mathbf{W}_r \mathbf{e}_r \right) + q_{\dot{\beta}} \cdot \tfrac{2}{\pi} \left(\mathbf{e}_{\dot{\beta}}^T \mathbf{W}_{\dot{\beta}} \mathbf{e}_{\dot{\beta}} \right) \tag{6-24}$$

Note that additional weights q appear in the expression. These weights provide the possibility of tuning the cost-function to improve the convergence of the algorithm. The derivation of the weights values is discussed in the following chapters. Based on the cost-function, a multi-objective optimization problem is formulated (6-25). The optimization searches those control inputs $\dot{\delta}$ and $F_{x,R}$ that minimize the cost-function and satisfies the constraints.

$$\begin{aligned}
\min_{\dot{\delta}, F_{x,R}} \quad & J = q_{pos} \cdot \frac{1}{0.1 \cdot N} \left(\mathbf{e}_{pos,1}^T \mathbf{W}_{pos,1} \mathbf{e}_{pos,1} + \mathbf{e}_{pos,2}^T \mathbf{W}_{pos,2} \mathbf{e}_{pos,2} \right) + \\
& \quad q_V \cdot \frac{1}{0.1 \cdot N} \left(\mathbf{e}_V^T \mathbf{W}_V \mathbf{e}_V \right) + q_r \cdot \frac{2}{\pi} \left(\mathbf{e}_r^T \mathbf{W}_r \mathbf{e}_r \right) + q_{\dot{\beta}} \cdot \frac{2}{\pi} \left(\mathbf{e}_{\dot{\beta}}^T \mathbf{W}_{\dot{\beta}} \mathbf{e}_{\dot{\beta}} \right) \\
\text{subject to} \quad & \dot{u} = \frac{1}{m} \left(2F_{x,R} \right) + vr \\
& \dot{v} = \frac{1}{m} \left(2F_{y,F} + 2F_{y,R} \right) - ur \\
& \dot{r} = \frac{1}{I_z} \left(2l_F F_{y,F} - 2l_R F_{y,R} \right) \\
& \dot{u}_0 = 0 \\
& u_0 = 2 \\
& \dot{v}_0 = 0 \\
& v_0 = 0 \\
& \dot{r}_0 = 0 \\
& r_0 = 0 \\
& \left| \dot{\delta} \right| \leq \frac{10 \cdot \pi}{6} \\
& |\delta| \leq \frac{\pi}{6} \\
& \left| F_{x,R} \right| \leq \mu \frac{1}{2} F_{z,R}
\end{aligned} \tag{6-25}$$

The optimization problem is subject to the dynamics of the single-track model. The expression that was derived under the assumption or small steering angles is used (2-21). Furthermore, the initial conditions of the states and their derivatives are included. The final constraints describe the bounds that are defined for the control inputs of the vehicle.

6-3 Optimization Structure

Now that the optimization problem is defined, this section addresses the structure that is used to generate the trajectory. The ultimate goal of the optimization is to find a set of input signals that make the vehicle negotiate the corner in the best way possible. This basically is a dynamic inversion problem. However, since the model is too complex to solve the inversion problem, it is written into a minimization problem. The optimization is subject to a set of constraints. The most important condition is that the dynamics of the single-track model are satisfied. This is achieved through using the vehicle model, that was derived in the previous chapters, to solve a simulation-based optimization. Since the initial conditions of an optimization algorithm can determine the convergence, it is crucial to evaluate the initial conditions. For this issue, one could think of two possible solutions. A global-search algorithm can be used, which evaluates multiple trial points with varying initial conditions. The other option is to choose the initial conditions wisely, such that convergence, whether it is a drift equilibrium or not, is stimulated.

The optimization problem as it is formulated above incorporates the vehicle dynamics in a SIMULINK-model. The cost-function is computed based on the outputs of this model. Applying a global-search algorithm on this simulation-based optimization would have an enormous impact on the computation time. A more elegant approach would be to find an educated guess of the optimal inputs based on a simplified model. Spline optimization is used for this purpose. The literature provides various applications for spline optimization as a path planning method. In aerospace engineering it is used to generate trajectories for quad-rotor helicopters [6, 36], in vehicle engineering there is a study that addresses the suitability for a truck-trailer combination [5]. To summarize, the dynamic trajectory optimization is a two-phase approach (Figure 6-4).

- *Spline optimization*
  The aim of the spline optimization is to initiate the search of the simulation-based optimization. The time domain signals are parameterized. Starting from a set of randomly generated control points ($\mathbf{P}_x, \mathbf{P}_y, \mathbf{P}_\psi, \mathbf{P}_\delta, \mathbf{P}_{F_{x,R}}$), the spline optimization outputs the signals $\dot{\delta}^{init}$ and $F_{x,R}^{init}$. As speed of convergence is considered to be more important than accuracy, the optimization is based on a simplified cost-function and vehicle model. The modifications that are made to (6-25) are described in the next chapter.

- *Simulation-based optimization.*
  The spline optimization is based on a simplified optimization problem. The results will therefore not directly be applicable to the higher fidelity model that was derived in the previous chapter. The purpose of the simulation-based optimization is to refine the signal resulting from the spline optimization until the eventual $\dot{\delta}$ and $F_{x,R}$ are a solution to the original optimization problem (6-25).

The following chapter describe each optimization step in more detail. The spline optimization is discussed in chapter 7, the simulation-based optimization is addressed in chapter 8.

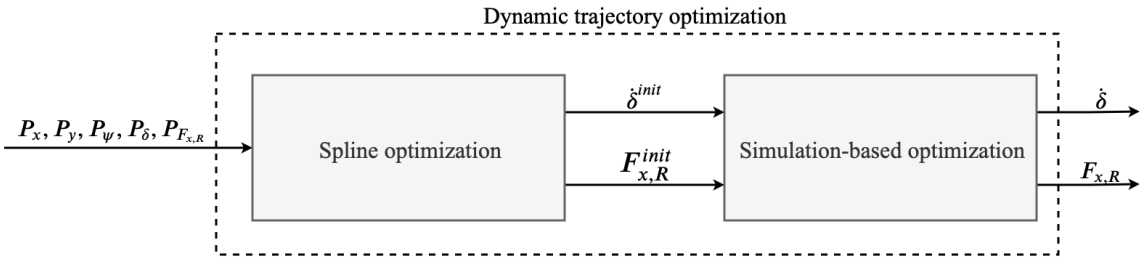

Figure 6-4: Schematic overview of the two phases of the dynamic trajectory optimization.

6-4 Conclusions

This chapter provides a description of the dynamic driving scenario and explains how it is written into an optimization problem. This section provides the conclusions that are drawn.

- The single corner scenario captures the relevant aspects of vehicle dynamics; it consists of transient steady-state motion. Since steady-state cornering is part of the maneuver, it creates the possibility of comparing the dynamic driving scenario with the steady-state cornering equilibria of chapter 5.
- The single corner maneuver can be written into a multi-objective optimization problem by defining a cost-function that consists of error terms accounting for the position, the velocity, the yaw rate, and the side-slip rate. The total cost-function is a weighted sum of the cost-function terms. Depending on the importance of each term, the weights need to be defined.
- To achieve convergence of the trajectory optimization in a reasonable time, a two-phase optimization structure is used. In the first step, a spline parameterization is performed, based on a simplified model and a modified cost-function. The results of this step are then used as initial conditions for a higher fidelity simulation-based optimization. The signals are refined such that the optimization problem of the dynamic driving scenario is solved and the constraints are satisfied.

Chapter 7

Spline Optimization

The structure of the dynamic trajectory optimization is discussed in the previous chapter. The spline optimization is used to obtain initial input signals that result in vehicle motion that already partly matches the desired maneuver. The main purpose of this approach is to reduced the time that the simulation-based optimization requires to converge to the solution in the second phase. This chapter describes how initial input signals can be obtained from the spline optimization.

Section 7-1 explains the working principle of spline optimization. Section 7-2 discusses which signals need to be approximated by a spline in order to describe the motion of the vehicle. The spline optimization is based on a simplified expression of the single-track model. Section 7-3 elaborates on the modifications that are made to the optimization problem that was derived in the previous chapter. The results of the spline optimization are presented in section 7-4. Finally, the conclusions are drawn in section 7-5.

7-1 General Working Principle

A spline is defined as the product of several basis functions and spline coefficients. The main motivation for using splines is that it allows for parameterizing high order signals with a relatively small amount of spline-coefficients. Consider the expression of the spline segment $S_i(\tau)$:

$$S_i(\tau) = \begin{bmatrix} C_1(\tau) & C_2(\tau) & C_3(\tau) & C_4(\tau) & C_5(\tau) & C_6(\tau) \end{bmatrix} \begin{bmatrix} P_{i-2} \\ P_{i-1} \\ P_i \\ P_{i+1} \\ P_{i+2} \\ P_{i+3} \end{bmatrix}. \tag{7-1}$$

The spline segment is defined as the summation of the products of the basis functions $C_k(\tau),\ k \in \{1,\ldots,6\}$ and the control points $P_i,\ i \in \{-2,\ldots,3\}$. As an example, the basis functions of the quintic Bézier-splines are displayed in Figure 7-1. Each function has a unique shape and is a function of τ, which is defined between 0 and 1. The larger the control point, the more dominant the corresponding basis function will be in the summation. Through changing the control points, different higher-order polynomials can be approximated. When all the control points have the same value, the result of the summation $\sum_i^{1:6} C_i(\tau)$ will be a straight line. For unequal control points, the spline segments are the weighted sum of the basic polynomials multiplied by the control points. The goal of the spline optimization is to find the specific combination of control points that result in the spline that match the desired signal.

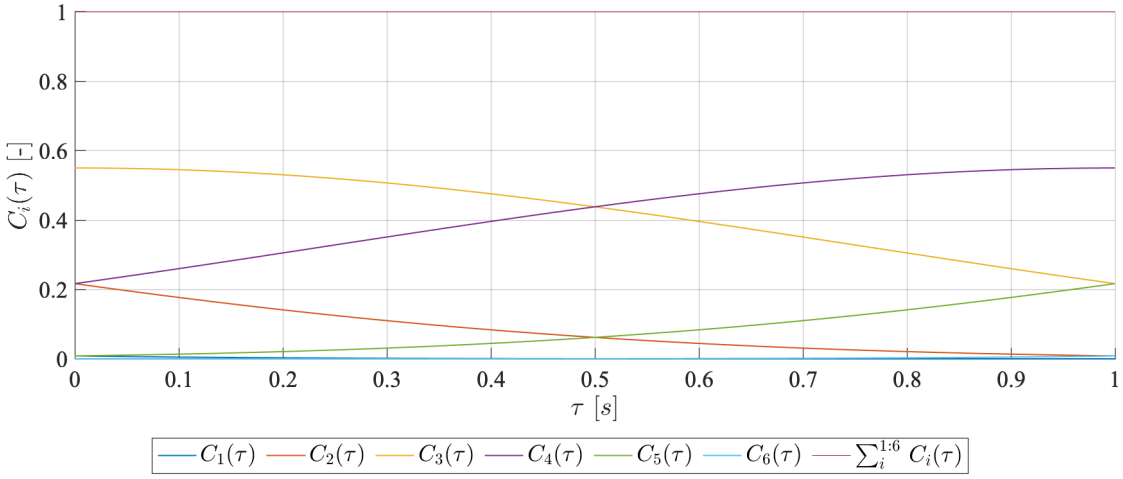

Figure 7-1: Overview of the basis functions of the quintic Bézier spline

Various types of spline definitions are described in the literature. The distinction is made between cubic and quintic splines [31]. The difference between them is the highest order that is present in the basis functions. The basis functions of the cubic splines are third-order polynomials, the functions of the quintic splines are fifth-order. Because of these higher-order terms, quintic spline provides $\mathbb{C}^2$ continuity. This implies that the second derivative of the spline is continuous and smooth. In the scope of the dynamic optimization of this work, achieving continuity is required as discontinuities in the signals would yield unfeasible dynamics. Furthermore, the quintic splines are formed by six basis functions, where the cubic spline only has four. The increased number of basis functions gives more freedom to approximate a trajectory that satisfies the constraints.

An illustrative example of spline optimization is displayed in Figure 7-2. The spline that describes the position consists of four segments $S_i(t)$. It can be seen that the spline does not visit all control points. This is caused by the dependency on the surrounding control points (7-1). Consider, for example, the first segment $S_1(t)$. It is a connection between P_2 and P_3. However, it also depends on the previous two and the following two control points. The continuity of the position, velocity, and acceleration signals is guaranteed by the fact that each consecutive spline segments share five control points with the previous segment. As can be observed in Figure 7-2, both the velocity and the acceleration signals are smooth and

continuous.

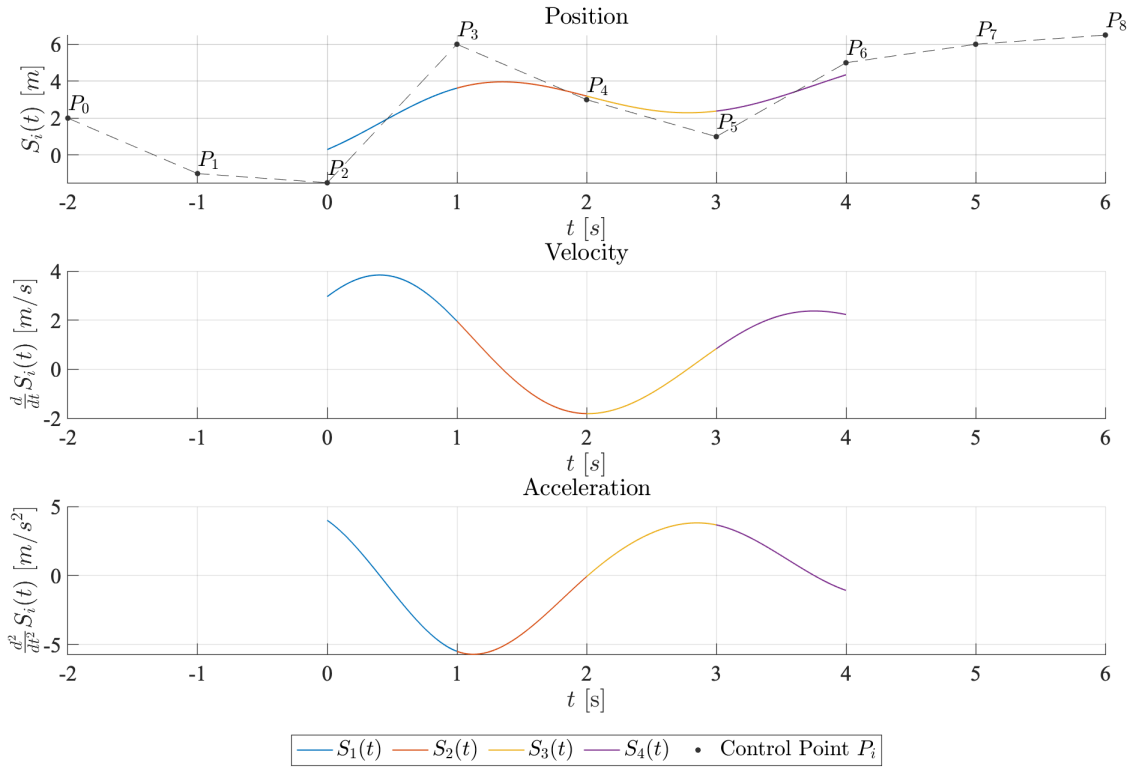

Figure 7-2: Visualization of the $\mathbb{C}^2$ continuity provided by the quintic Bézier spline expression.

Quintic Bézier-splines are used in this work. The definition of a single Bézier spline segment reads as (7-2), the expression is derived from [31].

$$S_i(\tau) = \begin{bmatrix} 1 & \tau & \tau^2 & \tau^3 & \tau^4 & \tau^5 \end{bmatrix} \frac{1}{5!} \begin{bmatrix} 1 & 26 & 66 & 26 & 1 & 0 \\ -5 & -50 & 0 & 50 & 5 & 0 \\ 10 & 20 & -60 & 20 & 10 & 0 \\ -10 & 20 & 0 & -20 & 10 & 0 \\ 5 & -20 & 30 & -20 & 5 & 0 \\ -1 & 5 & -10 & 10 & -5 & 1 \end{bmatrix} \begin{bmatrix} P_i \\ P_{i+1} \\ P_{i+2} \\ P_{i+3} \\ P_{i+4} \\ P_{i+5} \end{bmatrix} \tag{7-2}$$

A typical spline with N segments reads as (7-3). The time interval t is divided in N sub-intervals, where τ varies from 0 to 1.

$$z(t) = \begin{bmatrix} S_{z,1}(\tau) & S_{z,2}(\tau) & \dots & S_{z,N}(\tau) \end{bmatrix} \tag{7-3}$$

$$t = \begin{bmatrix} \tau & 1+\tau & \dots & N+\tau \end{bmatrix} \tag{7-4}$$

$$\tau = \begin{bmatrix} 0 & 0.1 & \dots & 1 \end{bmatrix} \tag{7-5}$$

7-2 Spline Expressions

It has been described how the control points belonging to one or multiple spline segments can parameterize a continuous-time signal. In order to describe the dynamics of the vehicle, five signals need to be expressed as a spline: the position in the inertial coordinate frame ($x_{inertial}$ and $y_{inertial}$), the heading of the vehicle ψ, the steering angle δ and the longitudinal force $F_{x,R}$. All other variables can be written as a function of these signals and the time derivatives. Assuming N segments, the five basis spline are therefore defined as (7-6). In this chapter, the inertial coordinate frame is denoted by x and y. The velocities in the longitudinal and lateral direction are denoted by u and v, respectively.

$$x(t) = \begin{bmatrix} S_{x,1}(\tau) & S_{x,2}(\tau) & ... & S_{x,N}(\tau) \end{bmatrix} \tag{7-6}$$

$$y(t) = \begin{bmatrix} S_{y,1}(\tau) & S_{y,2}(\tau) & ... & S_{y,N}(\tau) \end{bmatrix} \tag{7-7}$$

$$\psi(t) = \begin{bmatrix} S_{\psi,1}(\tau) & S_{\psi,2}(\tau) & ... & S_{\psi,N}(\tau) \end{bmatrix} \tag{7-8}$$

$$\delta(t) = \begin{bmatrix} S_{\delta,1}(\tau) & S_{\delta,2}(\tau) & ... & S_{\delta,N}(\tau) \end{bmatrix} \tag{7-9}$$

$$F_{x,R}(t) = \begin{bmatrix} S_{F_{x,R},1}(\tau) & S_{F_{x,R},2}(\tau) & ... & S_{F_{x,R},N}(\tau) \end{bmatrix} \tag{7-10}$$

The first and second time-derivatives of each spline are computed. For example, the derivatives of the x-direction spline are:

$$\dot{x}(t) = \frac{1}{t_f}\begin{bmatrix} \frac{\mathrm{d}S_{x,1}(\tau)}{\mathrm{d}\tau} & \frac{\mathrm{d}S_{x,2}(\tau)}{\mathrm{d}\tau} & ... & \frac{\mathrm{d}x,S_N(\tau)}{\mathrm{d}\tau} \end{bmatrix}, \tag{7-11}$$

$$\ddot{x}(t) = \frac{1}{t_f}\begin{bmatrix} \frac{\mathrm{d}^2S_{x,1}(\tau)}{\mathrm{d}\tau^2} & \frac{\mathrm{d}^2S_{x,2}(\tau)}{\mathrm{d}\tau^2} & ... & \frac{\mathrm{d}^2x,S_N(\tau)}{\mathrm{d}\tau^2} \end{bmatrix}. \tag{7-12}$$

Note that each spline has a set of unique control points. The trajectory of the vehicle is therefore described by $n_{splines} \cdot (n_P + (N-1))$ control points. Here $n_{splines}$ is the number of basis splines, n_P the number of control points needed to define a single spline segment, and N is the number of segments. The time derivatives are defined by the same control points as the corresponding basis spline, therefore adding no extra control points. For the remainder of this chapter, the short notation for the control points will be used (7-13).

$$\mathbf{P}_x = \begin{bmatrix} P_{x,1} & \cdots & P_{x,(n_p+(N-1))} \end{bmatrix}^T \tag{7-13}$$

$$\mathbf{P}_y = \begin{bmatrix} P_{y,1} & \cdots & P_{y,(n_p+(N-1))} \end{bmatrix}^T \tag{7-14}$$

$$\mathbf{P}_\psi = \begin{bmatrix} P_{\psi,1} & \cdots & P_{\psi,(n_p+(N-1))} \end{bmatrix}^T \tag{7-15}$$

$$\mathbf{P}_\delta = \begin{bmatrix} P_{\delta,1} & \cdots & P_{\delta,(n_p+(N-1))} \end{bmatrix}^T \tag{7-16}$$

$$\mathbf{P}_{Fx,R} = \begin{bmatrix} P_{F_{x,R},1} & \cdots & P_{F_{x,R},(n_p+(N-1))} \end{bmatrix}^T \tag{7-17}$$

The body orientated velocities and accelerations can be expressed as a function of the above-described splines (7-18).

$$
\begin{aligned}
u(t) &= \dot{x}(t)\cos\left(\psi(t)\right) + \dot{y}(t)\sin\left(\psi(t)\right) && \text{(7-18)}\\
\dot{u}(t) &= \tfrac{\mathrm{d}u(t)}{\mathrm{d}t} && \text{(7-19)}\\
v(t) &= -\dot{x}(t)\sin\left(\psi(t)\right) + \dot{y}(t)\cos\left(\psi(t)\right) && \text{(7-20)}\\
\dot{v}(t) &= \tfrac{\mathrm{d}v(t)}{\mathrm{d}t} && \text{(7-21)}
\end{aligned}
$$

7-3 Modified Optimization Problem

The schematic of Figure 7-3 summarizes the goal of the spline optimization. For each set of control points, the spline that results from these points describes a vehicle motion. A cost-function is computed to quantify how closely this motion matches the cornering scenario of chapter 6. The goal of the spline optimization is to find those control points that yield the lowest objective value.

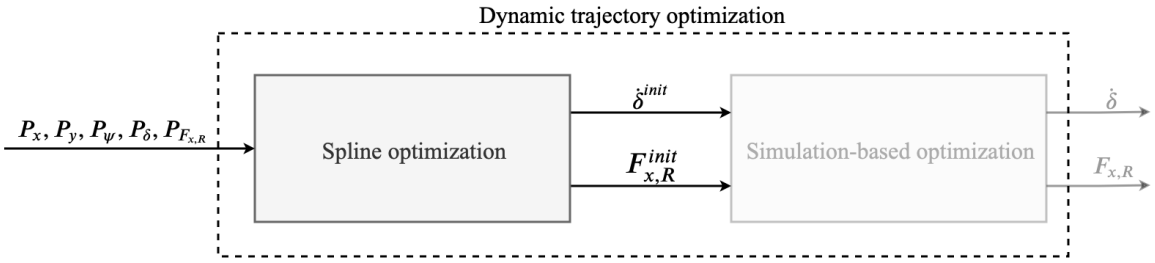

Figure 7-3: Schematic overview of the spline optimization: the initial input signals $\dot{\delta}^{init}$ and $F_{x,R}^{init}$ are parameterized with by a finite number of control points.

The original optimization problem (6-25) can not directly be applied to the spline optimization. In order to reduce the computation time of the spline optimization, the complexity of the single-track model is reduced. It can be argued that this yields a less accurate description of the vehicle dynamics. However, as the resulting signals are further refined in the second optimization phase (Figure 7-3), quick convergence to a solution is considered to be the main priority. Furthermore, the constraints that were defined needs to be written in terms of the splines. The optimization problem that was formulated in (6-25) is modified to account for these changes. The spline optimization can mathematically be formulated as in (7-22).

$$
\begin{aligned}
\min_{\mathbf{P}} \quad & J = q_{pos,spline} \cdot \frac{1}{0.1 \cdot N}\left(\mathbf{e}_{pos,spline}^{T}\mathbf{e}_{pos,spline}\right) + \\
& \qquad q_{V,spline} \cdot \frac{1}{0.1 \cdot N}\left(\mathbf{e}_{V,spline}^{T}\mathbf{e}_{V,spline}\right) \\
& \mathbf{A}_{nl,eq}\left(\mathbf{P}\right) = 0 \\
& \mathbf{A}_{eq}\mathbf{P} = \mathbf{b}_{eq} \\
& \mathbf{A}_{ineq}\mathbf{P} \leq \mathbf{b}_{ineq} \\
& -1\mathrm{e}3 \leq \mathbf{P} \leq 1\mathrm{e}3
\end{aligned}
\qquad \text{(7-22)}
$$

Here, $\mathbf{P} = \begin{bmatrix} \mathbf{P}_x & \mathbf{P}_y & \mathbf{P}_\psi & \mathbf{P}_\delta & \mathbf{P}_{F_{x,R}} \end{bmatrix}^T$ represents the vector containing the control points of the predefined spline (Section 7-2). Furthermore, $\mathbf{e}_{pos,spline}$ and $\mathbf{e}_{V,spline}$ are the cost-function terms, with corresponding weights $q_{pos,spline}$ and $q_{V,spline}$. The dynamics of the vehicle are written into a set of nonlinear equality constraints $\mathbf{A}_{nl,eq}(\mathbf{P}) = 0$. The equality constraints are combined in $\mathbf{A}_{eq}\mathbf{P} = \mathbf{b}_{eq}$. The inequality constraints are denoted by $\mathbf{A}_{ineq}\mathbf{P} \leq \mathbf{b}_{ineq}$. The splines are bounded by defining minimum maximum values of the control points. The following sections elaborate on the structure of the modified optimization problem. First the cost-function is considered, then the constraints are discussed.

Cost-Function

Two important modifications are made with respect to the cost-function (6-25). In order to reduce the complexity, the maneuver is assumed to consist of one segment. The vehicle is not expected to drive in a straight line after $\psi + \beta > \frac{\pi}{2}$ (90°). Instead, the desired motion is a circular trajectory with a constant radius R. Furthermore, the desired conditions on the yaw rate and side-slip rate are not included in the cost-function. As both variables are described by a spline, the desired value at any time step can be formulated as an equality constraint. Therefore, the remaining cost-function terms are the position and the velocity of the vehicle.

The position error $\mathbf{e}_{pos,spline}$ is defined as the cross-track error (Figure 6-3) (7-23). Note that the no weight matrix $\mathbf{W}$ is included since the cost-function is not split into two segments.

$$\mathbf{e}_{pos,spline} = \sqrt{(x(t) - x_c)^2 + (y(t) - y_c)^2} - R_{ref}. \tag{7-23}$$

Similar to the cost-function term in the previous chapter, $\mathbf{e}_{V,spline}$ denotes the difference between the cornering velocity and the reference velocity (7-24). Again, no weight matrix is required.

$$\mathbf{e}_{V,spline} = \sqrt{u(t)^2 + v(t)^2} - V_{ref}. \tag{7-24}$$

The modified cost-function is defined as the weighted sum of the two terms (7-25). The weights are denoted by $q_{pos,spline}$ and $q_{V,spline}$. Following the approach that was presented in the previous chapter, both terms are scaled by $0.1 \cdot N$. Here N is the length of the discrete-time vector.

$$J = q_{pos,spline} \cdot \frac{1}{0.1 \cdot N} \left(\mathbf{e}_{pos,spline}^T \mathbf{e}_{pos,spline} \right) + q_{V,spline} \cdot \frac{1}{0.1 \cdot N} \left(\mathbf{e}_{V,spline}^T \mathbf{e}_{V,spline} \right) \tag{7-25}$$

The cost-function is evaluated over a discrete time domain. When the time vector is denoted by $\mathbf{t} \in \mathbb{R}^{N \times 1}$, both $\mathbf{e}_{pos,spline}$ and $\mathbf{e}_{V,spline}$ are vectors with dimension $\mathbb{R}^{N \times 1}$. The cost-function J is a function of the control points of each splines.

Nonlinear constraints

The nonlinear constraints account for the variables that are a nonlinear function of the splines. The state equations of the single-track model are rewritten into (7-26). The concept of writing system dynamics into spline constraints has been presented in [9, 23]. Note that the steering angle is not included in the constraints. It is assumed that δ is very small such that $\cos(\delta) \approx 1$. The justification for using this assumption, and the corresponding errors, is

previously addressed in chapter 5. Note that instead of $r(t)$, the yaw rate is denoted by $\dot{\psi}(t)$. The notation is more intuitive in this context since it is the time derivative of the $\psi(t)$ spline.

$$z_1(t) = -\dot{u}(t) + \tfrac{1}{m}\left(2 \cdot F_{x,R}(t)\right) + v(t) \cdot \dot{\psi}(t) \tag{7-26}$$
$$z_2(t) = -\dot{v}(t) + \tfrac{1}{m}\left(2 \cdot F_{y,F}(t) + 2 \cdot F_{y,R}(t)\right) - u(t) \cdot \dot{\psi}(t) \tag{7-27}$$
$$z_3(t) = -\ddot{\psi}(t) + \tfrac{1}{I}\left(2 \cdot l_R \cdot F_{y,F}(t) + 2 \cdot l_F \cdot F_{y,R}(t)\right) \tag{7-28}$$

The tire forces are described by the linear tire model (7-29). The tire model coefficients $C_{y,F}$, $C_{y,R}$, result from the tire identification. In addition to the Dugoff tire model, the identification steps are also performed for the linear tire model.

$$F_{y,F}(t) = C_{y,F} \cdot \alpha_F(t) \tag{7-29}$$
$$F_{y,R}(t) = C_{y,R} \cdot \alpha_R(t) \tag{7-30}$$

The lateral slip angles at the front and the rear tire are defined as:

$$\alpha_F(t) = \delta - \tfrac{v(t)+l_F \cdot \dot{\psi}(t)}{u(t)}, \tag{7-31}$$
$$\alpha_R(t) = -\tfrac{v(t)-l_R \cdot \dot{\psi}(t)}{u(t)}. \tag{7-32}$$

In addition to the state equations, the reference cornering velocity is included in the nonlinear constraints matrix $\mathbf{A}_{nl,eq}(\mathbf{P})$ (7-33).

$$\mathbf{A}_{nl,eq}(\mathbf{P}) = \begin{bmatrix} z_1(t) & z_2(t) & z_3(t) & \left(\sqrt{u(t)^2 + v(t)^2} - V_{ref}\right) \end{bmatrix} \tag{7-33}$$

Equality constraints
The equality constraint matrix $\mathbf{A}_{eq}\mathbf{P}$ contains all the conditions that apply to a single spline function. The initial position expressed in the inertial reference frame, the initial value of the heading and the initial steering angle are included. Additionally, the longitudinal force of the rear tire should initially be zero.

$$\mathbf{A}_{eq}\mathbf{P} = \mathbf{b}_{eq} \tag{7-34}$$

$$\mathbf{A}_{eq}\mathbf{P} = \begin{bmatrix} x(0) & y(0) & \psi(0) & \delta(0) & F_{x,R}(0) \end{bmatrix}^T \tag{7-35}$$
$$\mathbf{b}_{eq} = \begin{bmatrix} 0 & 0 & 0 & 0 & 0 \end{bmatrix}^T \tag{7-36}$$

Inequality constraints
The inequality constraints allow for defining physical boundaries. The location of the vehicle

is restricted to -3 m and 3 m for both the x and y direction. The maximum absolute value of the yaw rate is set equal to π rad/s, which allows the vehicle to rotate 180°/s. The steering limits are $\frac{\pi}{6}$ rad (30°). The longitudinal force $F_{x,R}$ is bounded by the physical limits of the normal force that act on the rear tire, equal to 2.37 N.

$$\begin{aligned} -3 &\leq x(t) \leq 3 && \text{(7-37)}\\ -3 &\leq y(t) \leq 3 && \text{(7-38)}\\ -\pi &\leq \dot{\psi}(t) \leq \pi && \text{(7-39)}\\ -\frac{\pi}{6} &\leq \delta(t) \leq \frac{\pi}{6} && \text{(7-40)}\\ -2.37 &\leq F_{x,R}(t) \leq 2.37 && \text{(7-41)} \end{aligned}$$

The boundaries are written into the inequality constraint matrix $\mathbf{A}_{ineq}\mathbf{P}$.

$$\mathbf{A}_{ineq}\mathbf{P} \leq \mathbf{b}_{ineq} \tag{7-42}$$

$$\mathbf{A}_{ineq}\mathbf{P} = \begin{bmatrix} -x(t) & x(t) & -y(t) & y(t) & -\dot{\psi}(t) & \dot{\psi}(t) & -\delta(t) & \delta(t) & -F_{x,R}(t) & F_{x,R}(t) \end{bmatrix}^T \tag{7-43}$$

$$\mathbf{b}_{ineq} = \begin{bmatrix} 3 & 3 & 3 & 3 & \pi & \pi & \frac{\pi}{6} & \frac{\pi}{6} & 2.37 & 2.37 \end{bmatrix}^T \tag{7-44}$$

Bounds
The bounds of the splines apply to the control points since these are optimized. The optimization is solved with a global search algorithm (Appendix E) which evaluates multiple initial control points. Any trial point that has at least one initial control point that exceeds the bound will not be evaluated. It could be possible that a trial point that initially violates the bounds can converge to a local optimum within the bounds. However, evaluating a wider variety of trial points comes at the cost of increased computation time. Defining the bounds is, therefore, a trade-off between optimality and computation time. In an iterative process, the optimization is performed with varying bounds. Each time the time domain response of the optimization result and computation time are assessed. The best solution to this trade-off is found to be the bound having a value equal to 1e3.

7-4 Results

To provide the inputs to the simulation-based optimization, the spline optimization is performed for a circular trajectory with reference radius $R = 1$ m. In the optimization, only a single spline segment is considered to keep the computational load as low as possible. The desired velocity is $V_{ref} = 2$ m/s. To further reduce the complexity of the two-phase optimization approach, only a single set of initial input signals is computed. Although the simulation-based optimization is performed under varying cornering velocities, the initial signals resulting from this single spline optimization are used. Computing a specific set of initial signals for each

optimization scenario can potentially improve convergence. However, this is out of the scope of this work.

The initial control points of the spline are randomly generated values that lie between the predefined bounds. The spline optimization is performed with a global search method. A detailed description of this algorithm is presented in appendix E. The objective function is evaluated at the time steps of the discrete-time signal $t \in [0 : 0.05 : 1]$. The weights on the position ($q_{pos,spline}$) and the velocity term ($q_{V,spline}$ are equal to 1e3. The resulting vehicle maneuver is displayed in Figure 7-4.

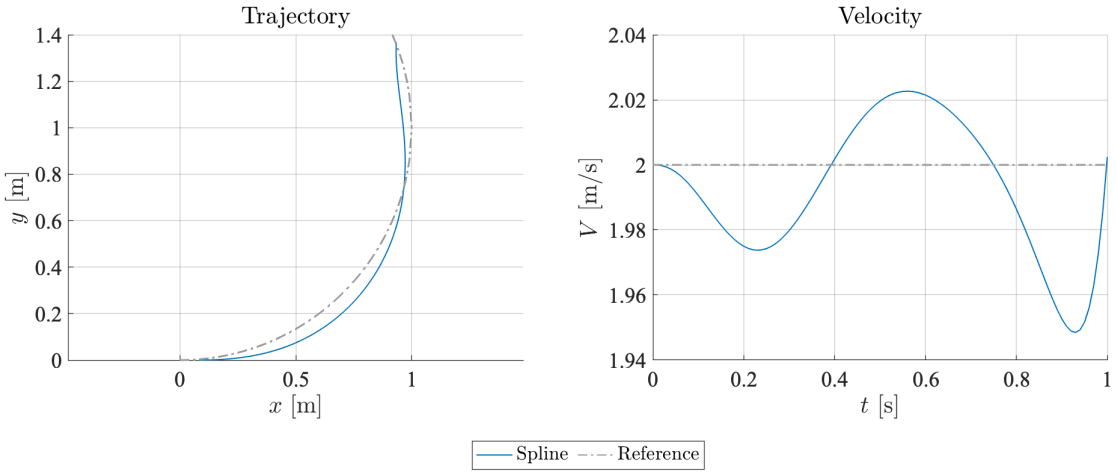

Figure 7-4: Overview of the maneuver resulting from the spline optimization.

Deviations in both the trajectory and the velocity are observed. Instead of traveling along the circular trajectory, the resulting motion of the vehicle can be described as a single corner followed by a straight line. It is expected that this is a result of the fact that only a single spline segment is considered. Supposing that the vehicle drives a perfect circle, the position (and therewith the velocity and acceleration) in either the longitudinal or lateral direction will be a sinusoidal signal. The expression of the acceleration spline (7-12) is a third-order polynomial. Therefore, multiple spline segments are required to approximate a sinusoidal signal. An increased number of spline segments could improve the optimization results. However, this is not included in this work.

The control inputs of the vehicle, the steering angle δ and the rear tire longitudinal force $F_{x,R}$, are depicted in Figure 7-5. The steering angle is observed to stay between the defined limits, which is an indication that the inequality constraints are satisfied. The rear tire longitudinal force is negative for the majority of the trajectory. This is a direct result of the assumption that the steering angle is small, implying $\cos(\delta) \approx 1$. When the vehicle steers into the corner, the lateral slip angle of the tires increase. Lateral tire forces are generated, and the lateral velocity increases. As the lateral tire forces do not influence the longitudinal dynamics (7-26), the longitudinal velocity u remains constant. The cornering velocity is defined as $V = \sqrt{u^2 + v^2}$, thus negative $F_{x,R}$ is applied to track the reference velocity.

When the assumption of small steering angles is released, the dynamics of the single-track model reads as (7-45). Note that the front tire lateral force appears in the expression of the longitudinal acceleration.

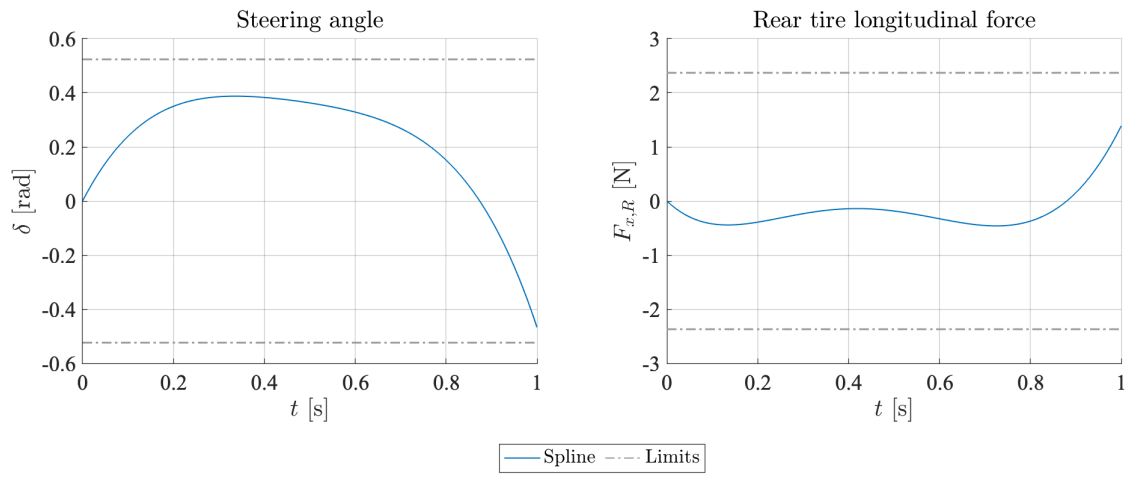

Figure 7-5: Overview of the control inputs resulting from the spline optimization.

$$\dot{u}(t) = \frac{1}{m}\left(2 \cdot F_{x,R}(t) - 2 \cdot F_{y,F} \cdot \sin\delta(t)\right) + v(t) \cdot \dot{\psi}(t), \tag{7-45}$$

$$\dot{v}(t) = \frac{1}{m}\left(2 \cdot F_{y,F}(t) \cdot \cos\delta(t) + 2 \cdot F_{y,R}(t)\right) - u(t) \cdot \dot{\psi}(t), \tag{7-46}$$

$$\ddot{\psi}(t) = \frac{1}{I}\left(2 \cdot l_R \cdot F_{y,F}(t) \cdot \cos\delta(t) + 2 \cdot l_F \cdot F_{y,R}(t)\right). \tag{7-47}$$

Based on these equations, the longitudinal velocity u will decrease when the vehicle enters the corner. As a result of the non-zero steering angle, the front tire lateral force has a negative component in the longitudinal direction. Due to the increased slip angles of the tire, the cornering velocity is expected to decrease. In order to track the reference velocity, a positive $F_{x,R}$ needs to be applied. At $t = 0.3$ s, the steering angle is approximately 0.4 rad (Figure 7-5). Therefore, the negative longitudinal component of $F_{y,R}$ is equal to 38.9% ($\sin(0.4)$) of that force. The linear tire model is used in this optimization, so tire saturation and force coupling are not incorperated in the model. The result of the spline optimization is expected not to change significantly. However, it is important to assess the effect on the simulation-based optimization.

The dynamics of the vehicle were written into nonlinear constraints (7-26). To verify whether the constraints are satisfied, the splines of the longitudinal velocity, the lateral velocity, and the yaw acceleration are displayed in Figure 7-6. In addition, the signals that the splines should equal, according to (7-26), are plotted. If the constraints are satisfied, the two signals are a perfect match. Any error between the signals indicates that the nonlinear constraints are not satisfied. This means that the resulting vehicle motion violates the dynamics of the single-track model at each time step.

The match between the splines and the corresponding constraints is expressed in terms of the Variance Accounted For (VAF) and Root Mean Squared Error (RMSE) (Table 7-1). For the spline that describes the longitudinal acceleration, the VAF is too low to state that the spline optimization is an accurate description of the single-track model.

Based on the analysis of the nonlinear constraints, it is concluded that the spline optimization is unsuccessful in generating a trajectory that is physically feasible at each time step. Although

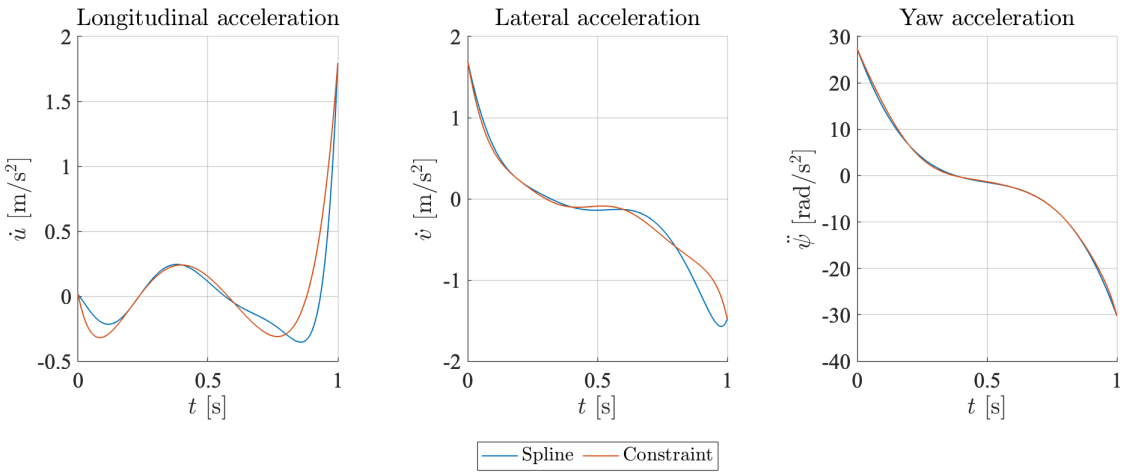

Figure 7-6: Overview of the state derivative (expressed in splines) and the corresponding constraints.

Table 7-1: Assessment of the fit between the spline signals and the constraints that describe the dynamics of the single-track model, based on the VAF and the RMSE

Spline	VAF	RMSE
$\dot{u}$	82.2148%	0.1630 m/s^2
$\dot{v}$	94.1379%	0.1460 m/s^2
$\ddot{\psi}$	99.9219%	0.3656 rad/s^2

the results resemble the desired maneuver, the signals need further refinement to satisfy the dynamics of the single-track model. This is currently achieved through the model-based optimization, as discussed in chapter 8. Further improving the spline optimization could also be an option. The number of segments could be optimized, or a more advanced tire model could be implemented. Both options increase the complexity of the optimization. Motivated by the idea that the results are only used as an initialization of the simulation-based optimization, any modifications to the spline optimization are considered to be potential subjects for further research.

7-5 Conclusions

The purpose of this chapter is to assess how initial input signals can be obtained from spline optimization. The following conclusions can be drawn:

- The splines are a parameterization of the time domain signals. Five splines ($x_{inertial}$, $y_{inertial}$, ψ, δ, $F_{x,R}$) are sufficient to describe the motion of a moving vehicle. The dynamics of the single-track model can be expressed as a function of these splines. The state derivatives are written into nonlinear constraints of the optimization problem.
- To improve the speed of convergence, the original optimization problem is simplified.

The maneuver is considered to consist of a single segment, which reduces the complexity of the cost-function. Furthermore, the linear model is used to describe the tire forces.

- Although the vehicle motion that results from the spline optimization resembles the desired trajectory, the dynamics are unfeasible at some time steps. The nonlinear constraints are not zero, indicating that the dynamics of the single-track are violated. However, the results are considered to be suitable for the purpose of initializing the simulation-based optimization.
- The initial conditions of the simulation-based optimization are obtained from a single spline optimization. In this scenario the radius is 1 m and the reference velocity is 2 m/s. This specific initialization is used for all simulation-based optimization scenarios.

Chapter 8

Simulation-Based Optimization

The previous chapters described the dynamic cornering scenario and the methodology for obtaining the initial input signals. In this chapter, the simulation-based optimization is discussed. This chapter studies whether the characteristics of drifting obtained in the steady-state analysis (Chapter 5) also become apparent in the dynamic driving scenario. The optimization is performed for a set of different cornering velocities and under varying friction conditions. The purpose is to match a subset of the previously obtained cornering equilibria in terms of dynamics.

Section 8-1 starts with a verification as initialization of the simulation-based optimization. The objective function of the optimization problem is the weighted sum of four terms. Based on the sensitivity analysis that is presented section 8-2, the values of the weights are determined. The results of the optimization are presented in section 8-3. Section 8-4 contains a discussion about the optimization results. The conclusions are listed in section 8-5.

8-1 Verification of the Spline Initialization

The spline optimization is used to initialize the search of the second optimization step (Figure 8-1). In order to justify the use of the spline optimization, it is compared with initial conditions that correspond to a vehicle that drives in a straight line. The optimization problem (6-25) is solved for both initial conditions. The results are compared based on the objective function, and the computational load of the optimization (Table 8-1).

The initial input signals resulting from the spline optimization are found to converge to a lower objective function. This comes with a longer computation time since the algorithm needs more function evaluations to yield the results. The objective function is considered to carry the biggest importance. Although this is only a comparison based on a single scenario, it is assumed that the spline optimization provides initial input signals that are closed to the output signals resulting from the simulation-based optimization. It is expected that the spline initialization improves the convergence of the second optimization.

Table 8-1: Performance of the simulation-based optimization for two scenarios: initial conditions provided by the spline optimization and initial conditions corresponding to driving in a straight line.

Metric	Straight line	Spline
Objective function	0.0487	0.0192
Number of function evaluations	385	594
Computation time	310.96 s	479.86 s

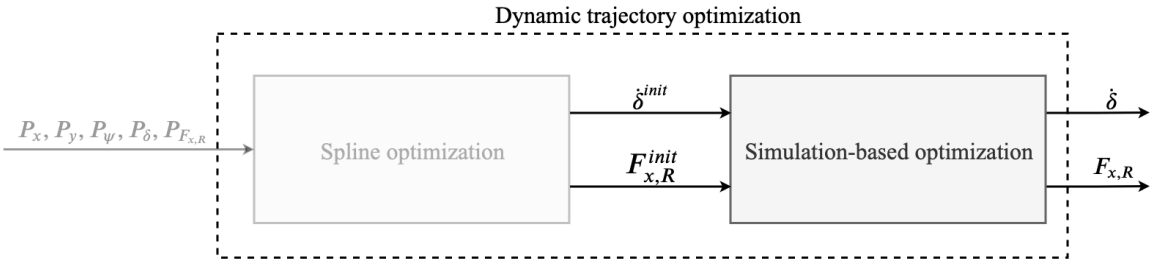

Figure 8-1: Schematic overview of the simulation-based optimization: the initial input signals are refined such that $\dot{\delta}$ and $F_{x,R}$ solve the dynamic trajectory optimization.

8-2 Weight Sensitivity Analysis

The cost-function of the optimization problem was a weighted summation of cost-function terms. This section presents a weight sensitivity analysis that is used to determine the values of the weights. Although various approaches can be applied, this work sets out to determine the weights for each cost-function term individually. The order in which the terms are evaluated is based on the relevance concerning the desired motion. In each step, the best possible weight for a specific cost-function term is selected. The renewed expression of the cost-function is then used to analyze the following term.

The most important term is the position since accurately following the trajectory makes it easier to compare the dynamics with the obtained steady-state equilibria. When considering a corner with a certain radius, one of the differences between normal and drift equilibria is the cornering velocity. For this reason, the velocity is the second most important. The yaw rate and the side-slip rate are about equally important. As the yaw rate is closely related to a stable driving situation, that term is preferred over the side-slip rate.

The first step of the sensitivity analysis is, therefore, to determine the value of the weight q_{pos}. The weight is varied in value, and the resulting cost-function term values are compared. With $q_{pos} = \{1, 10, 100\}$, the cost-function used in this step is displayed in (8-1). The weights are increased on the logarithmic scale to obtain an indication of the ideal order of magnitude of the weights. Further refinement of the weight values could yield better result but is out of the scope of this research.

$$J = q_{pos} \cdot J_{pos} + J_V + J_r + J_{\dot{\beta}} \tag{8-1}$$

The resulting cost-function values are listed in Table 8-2. It is concluded that the tracking

of the trajectory can be improved by increasing the weight of J_{pos}. For $q_{pos} = 10$, both the velocity and yaw rate term decrease as well. When the largest weight is applied, the tracking error is reduced by 93.30%. This comes at the cost of the other terms. Based on the idea that decreasing J_{pos} is the main priority, it is decided that $q_{pos} = 100$ is set as the weight of the position cost-function term. This is motivated by the observation that J_r and $J_{\dot{\beta}}$ can still be considered significantly small. Besides, the cost-function term of the velocity can be decreased in the next step of the sensitivity analysis.

Table 8-2: Comparison of cost-function terms for varying weight q_{pos}.

Weight	J_{pos}	$\Delta\%$	J_V	$\Delta\%$	J_r	$\Delta\%$	$J_{\dot{\beta}}$	$\Delta\%$
$q_{pos} = 1$	0.0113	[−]	0.0073	[−]	0.0003	[−]	0.0000	[−]
$q_{pos} = 10$	0.0032	−71.70	0.0029	−60.48	0.0000	−97.26	0.0000	66.15
$q_{pos} = 100$	0.0008	−93.30	0.0464	533.99	0.0005	69.03	0.0003	1149.04

The second step of the analysis is to determine the weight q_V that is applied to the velocity cost-function term. The previously derived weight for J_{pos} is included, resulting in the following cost-function.

$$J = 100 \cdot J_{pos} + q_V \cdot J_V + J_r + J_{\dot{\beta}} \tag{8-2}$$

Table 8-3 shows the results of the varying weight q_V. Although the velocity cost-function term is successfully decreased, it is observed that both J_{pos} and $J_{\dot{\beta}}$ suffer from increasing the weight. To decrease J_V as much as possible while minimizing the change of J_{pos}, it is decided that $q_V = 10$ is the best trade-off. The additional benefit of choosing this weight over $q_V = 100$ is that the yaw rate term does not increase.

Table 8-3: Comparison of cost-function terms for varying weight q_V.

J_{pos}	$\Delta\%$	**Weight**	J_V	$\Delta\%$	J_r	$\Delta\%$	$J_{\dot{\beta}}$	$\Delta\%$
0.0008	[−]	$q_V = 1$	0.0464	[−]	0.0005	[−]	0.0003	[−]
0.0026	243.06	$q_V = 10$	0.0086	−81.56	0.0000	−98.31	0.0116	3550.24
0.0034	344.82	$q_V = 100$	0.0002	−99.55	0.0020	286.97	0.0077	2305.90

In the third step of the sensitivity analysis, the weight of the yaw rate terms is varied. The cost-function then becomes:

$$J = 100 \cdot J_{pos} + 10 \cdot J_V + q_r \cdot J_r + J_{\dot{\beta}} \tag{8-3}$$

From the results (Table 8-4) it is found that the weight $q_r = 10$ has a positive effect on all the cost-function terms except for the term $J_{\dot{\beta}}$. Further increasing the weight q_r yields worse results for the position and velocity terms, which is undesired given the fact that these terms have the highest priority. It is decided to select $q_r = 10$.

As a final step, the weight that is applied to the term that accounts for the side-slip rate is determined. At this point the weighted cost-function reads as:

Table 8-4: Comparison of cost-function terms for varying weight q_r.

J_{pos}	$\Delta\%$	J_V	$\Delta\%$	**Weight**	J_r	$\Delta\%$	$J_{\dot{\beta}}$	$\Delta\%$
0.0026	[−]	0.0086	[−]	$q_r = 1$	0.0000	[−]	0.0116	[−]
0.0013	−49.33	0.0020	−76.33	$q_r = 10$	0.0000	−82.93	0.0233	100.50
0.0074	185.37	0.0309	260.05	$q_r = 100$	0.0000	452.37	0.0048	−69.06

$$J = 100 \cdot J_{pos} + 10 \cdot J_V + 10 \cdot J_r + q_{\dot{\beta}} \cdot J_{\dot{\beta}} \tag{8-4}$$

Unsatisfactory results are obtained for every weight $q_{\dot{\beta}}$ (Table 8-5). $J_{\dot{\beta}}$ is the only term that decreases, at the cost of the other terms. Given the fact that $J_{\dot{\beta}}$ has the lowest priority, it is decided not to increase the weight of this term.

Table 8-5: Comparison of cost-function terms for varying weight $q_{\dot{\beta}}$.

J_{pos}	$\Delta\%$	J_V	$\Delta\%$	J_r	$\Delta\%$	**Weight**	$J_{\dot{\beta}}$	$\Delta\%$
0.0013	[−]	0.0020	[−]	0.0000	[−]	$q_{\dot{\beta}} = 1$	0.0233	[−]
0.0019	41.15	0.0030	45.93	0.0000	768.83	$q_{\dot{\beta}} = 10$	0.0000	−99.98
0.0017	28.47	0.0030	45.83	0.0000	300.10	$q_{\dot{\beta}} = 100$	0.0000	−99.93

Based on the presented results and the described priority of each cost-function term, the sensitivity analysis concludes that the final cost-function can be expressed as:

$$J = 100 \cdot J_{pos} + 10 \cdot J_V + 10 \cdot J_r + J_{\dot{\beta}} \tag{8-5}$$

8-3 Results of the Dynamic Trajectory Optimization

At this point, the optimization problem (6-25) is formulated, and the weights of the cost-function are determined. In order to compare the results of the dynamic trajectory optimization with the steady-state equilibria, the optimization is solved under varying conditions. It has previously been concluded that drifting equilibria exist near the saturation limits of the tire. Two types of experiments are designed to bring the vehicle close to the friction limits. First, the trajectory optimization is performed for a variety of reference velocities. As the velocity is gradually increased, drifting is expected to become part of the vehicle motion. Another set of optimizations are performed in which the friction coefficient is decreased. The purpose of this analysis is to study what advantages the drift motion offers on low friction surfaces.

8-3-1 Variation of the Cornering Velocity

The optimization is performed for a range of velocities. The motivation for selecting the specific range lies in the equilibrium analysis of chapter 5. When narrowing the scope to an

1 m radius corner, the velocities of the obtained equilibria are between 0.1 and 2.4 m/s. By choosing the velocity range to be $\{1.6, 1.8, 2.0, 2.2, 2.4\}$, both stable and unstable equilibria should be part of the optimization results (Figure 8-2).

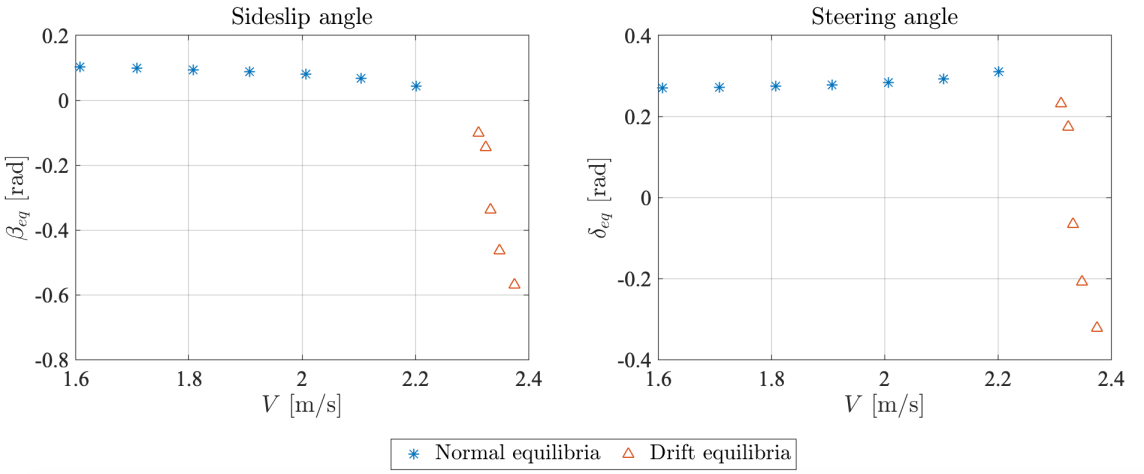

Figure 8-2: Cornering equilibria that are obtained for an 1m radius corner and a cornering velocity between 1.6 and 2.4 m/s.

Based on the fact that both normal and drift equilibria are within this range, it is expected that the optimization will yield different types of vehicle motion, depending on the cornering velocity. For velocities higher than 2.2 m/s it is expected that drift equilibria will be observed. These will be characterized by negative side-slip angles and rear tire saturation. For some equilibria also a negative steering angle will be observed.

Table 8-6 presents an overview of the cost-function terms under the different cornering velocities. It is concluded that position and velocity are tracked for all scenarios, except for $V = 2.4$ m/s. Furthermore, the optimization is capable of finding solutions that bring the yaw rate and side-slip rate close to zero. Only for the scenario in which $V = 1.8$ m/s, the term $J_{\dot{\beta}}$ is significantly larger.

Table 8-6: Overview of the cost-function terms that result from the simulation-based optimization under varying cornering velocities.

V	J_{pos}	J_V	J_r	$J_{\dot{\beta}}$
1.6	0.3728 e-3	0.2368 e-3	0.0036 e-3	0.0983 e-3
1.8	0.0014	0.0036	0.0029	0.2830
2.0	0.0013	0.0020	0.0000	0.0233
2.2	0.0051	0.0471	0.0002	0.0047
2.4	0.0084	0.2463	0.0000	0.0002

The values presented in Table 8-6 only provide a limited view of the optimization results. The time-domain responses of the vehicle dynamics help to deepen the understanding of the effect that the cornering velocity has on the maneuverability. In order to maintain the readability of the chapter, only the vital graphs will be discussed. A complete overview of the optimization results can be found in appendix F.

The optimized trajectories are displayed in the left graph of Figure 8-3. Based on the cornering velocity, the distance that the vehicle can travel within the fixed time frame differs. It is relevant to consider that although the cornering velocities vary, the simulation time remains constant. This effect can be observed from the trajectory plots. Where the vehicle just completes the corner for $V = 1.6$ m/s, the vehicle travels for almost another meter after the corner for $V = 2.4$ m/s. In the ideal situation, the simulation times would be scaled. In this case, either the length of the discrete-time vector or the time between two consecutive data points would change, therewith influencing the value of the objective function. In order to make a comparison based on the terms of the objective function, the simulation time is kept constant. A possible implication could be that the trade-off between following the trajectory and minimizing the yaw rate becomes apparent when the cornering velocity is lower. It is, however, assumed that this does not fundamentally change the outcome of this research since especially the higher velocities are interesting when analyzing in the drift motion.

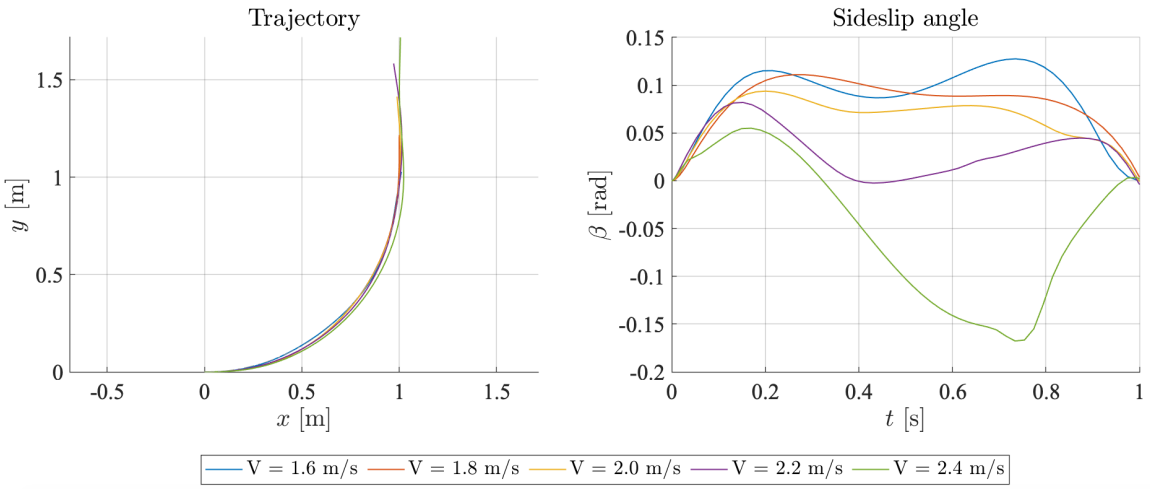

Figure 8-3: Time domain responses of the trajectory and sideslip angle resulting from the trajectory optimization under varying cornering velocities.

The side-slip angle during the maneuver is shown in the right graph of Figure 8-3. It is observed that as the velocity increases, the side-slip angle becomes negative during the maneuver. This corresponds to the conclusions that were drawn in chapter 5. The drift motion allows for negotiating the corner in the scenarios where the cornering velocity is highest.

The input signals are displayed in Figure 8-3. Since the initial steering angle and yaw rate are equal to zero, there is inevitably an initial trajectory tracking error (left graph of Figure 8-3). The error is corrected by the negative longitudinal force on the rear wheel, and the increased the steering angle (right graph of Figure 8-3). As was previously observed in section 7-4, the rear longitudinal tire force is negative in some scenarios. It is caused by the assumption of small steering angles. The implications of this assumption on the result are addressed in section 8-4.

As the cornering velocity increases, the steering angle also become bigger. In case of the highest velocity ($V = 2.4$ m/s), the steering limits is reached. This observation is expected when considering the system dynamics (2-21). According to the expression of the single-track model, higher velocities will yield higher tire forces. In the Dugoff tire model, higher slip

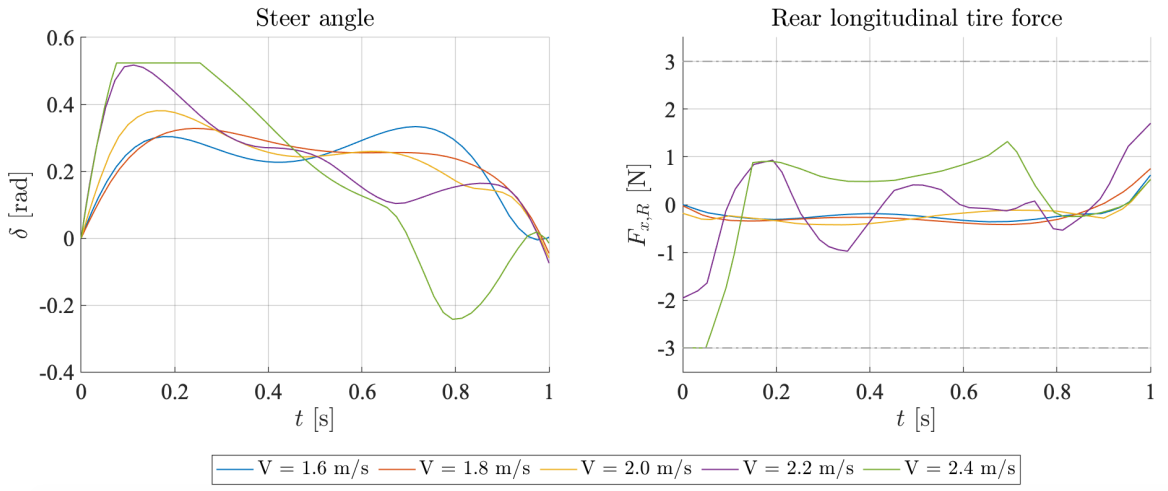

Figure 8-4: Time domain responses of the steering angle and throttle inputs resulting from the trajectory optimization under varying cornering velocities.

angles result in higher tire forces. The steering angle is directly related to the slip angle of the front tires. Therefore, the steering limits will be reached when the cornering velocity of the vehicle is increased.

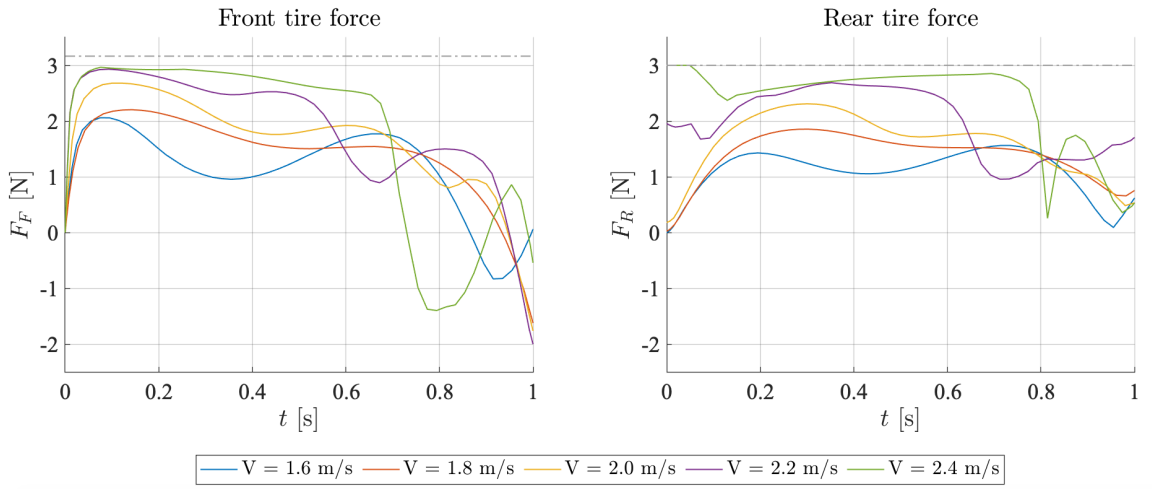

Figure 8-5: Time domain responses of the front and rear resultant tire forces resulting from the trajectory optimization under varying cornering velocities.

The relation between cornering velocity and tire forces can also be deduced from Figure 8-5. As the velocity increases, the tire forces grow in magnitude until the saturation limits are reached. In this saturation region, an further increase in tire forces can only be achieved through larger slip angles, eventually yielding the drift motion.

8-3-2 Variation of the Friction Coefficient

In the expression of the Dugoff tire model, the tire force that can be generated is depending on the normal force acting on the tire and the friction coefficient. It is therefore expected that when μ is decreased while keeping the cornering velocity constant, the tire will reach the saturation limits in an earlier stadium. In this analysis, the cornering velocity is constant ($V = 2$ m/s) and the friction coefficient is varied. The identified friction coefficient μ_{iden} is selected as the nominal case, which is then gradually decreased to simulate loose surfaces: $\mu = \{\mu_{iden}, 0.75 \cdot \mu_{iden}, 0.5 \cdot \mu_{iden}\}$.

The cost-function terms resulting from the optimization under varying μ are combined in Table 8-7. Based on the presented values, it is concluded that lowering the friction coefficient has the most substantial impact on the ability to track the trajectory and the velocity. Both J_{pos} and J_V increase significantly when less friction is available.

Table 8-7: Overview of the cost-function terms that result from the simulation-based optimization under varying friction conditions.

μ	J_{pos}	J_V	J_r	$J_{\dot{\beta}}$
μ_{iden}	0.0013	0.0020	0.0000	0.0233
$0.75 \cdot \mu_{iden}$	0.0089	0.0451	0.0150	0.0743
$0.5 \cdot \mu_{iden}$	0.1882	1.3648	0.0017	0.0255

The same conclusions are drawn from the figure containing the trajectories (Figure 8-6). Where the path can be tracked under normal conditions ($\mu = \mu_{iden}$), the vehicle can not negotiate the corner for lower friction conditions. As a result, the cornering radius of the vehicle's trajectory increases. From the right graph of Figure 8-6, it is observed that the side-slip angle becomes negative during the low friction scenarios. Low friction conditions decrease the amount of force that can be generated. In order to generate the tire forces that are required to track the reference trajectory, large lateral slip angles need to be achieved. The drifting motion can facilitate these large slip angles.

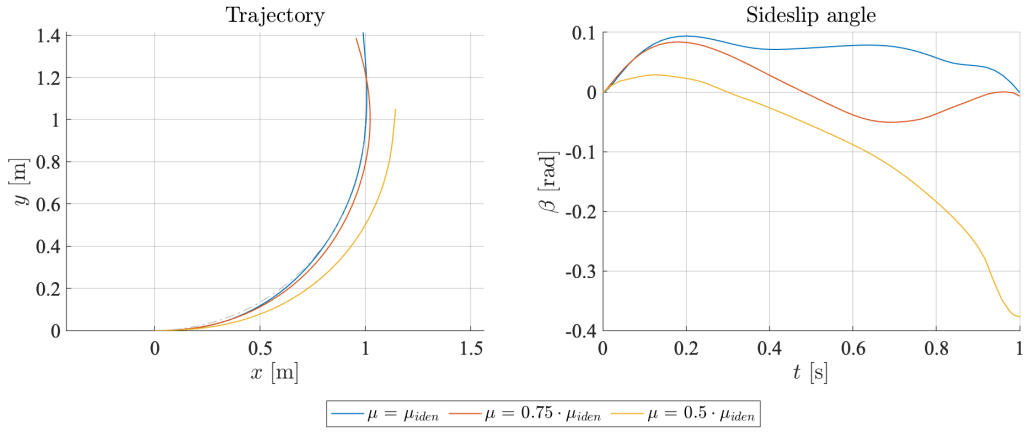

Figure 8-6: Time domain responses of the trajectory and sideslip angle resulting from the trajectory optimization under varying friction coefficients.

The steering angle that is required to negotiate the corner also increases, indicating that lower tire forces are generated for the same slip angles (Figure 8-7). As the steering angle remains positive, it is concluded that only under-steer drift equilibria are obtained. The term under-steer is used to describe the situation in which the vehicle is maneuvering with a negative side-slip angle β but with a positive steering angle δ. Only for the scenario with the lower friction, negative steering angles are present at the end of the maneuver (after $t = 0.7$ s). Although it could be argued that the motion of the vehicle at this point is similar to drifting, it was expected that this behavior becomes apparent during the corner. Section 8-4 elaborates on this topic.

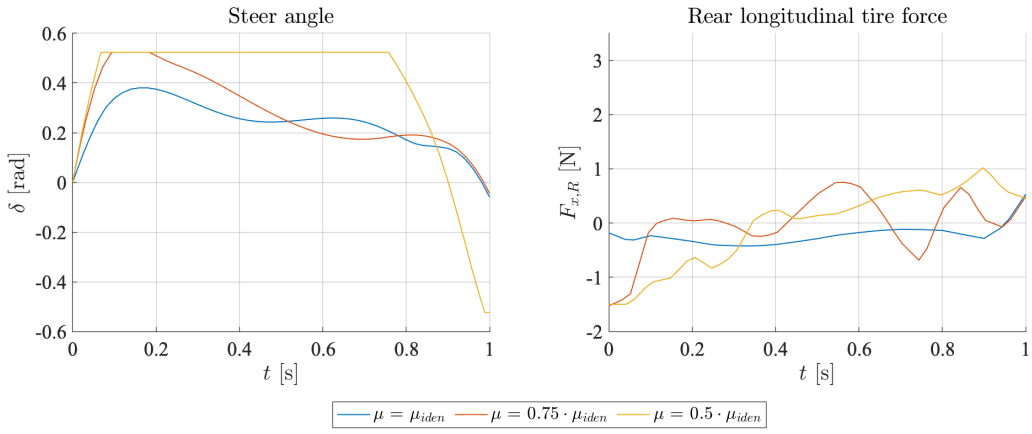

Figure 8-7: Time domain responses of the steering angle and throttle inputs resulting from the trajectory optimization under varying friction coefficients.

The resultant tire forces corresponding to the friction variation simulations math the expectations (Figure 8-8). Due to the decreased μ, the saturation limits of the tire becomes lower. As a result, the tires are saturated during cornering for the scenario in which $\mu = 0.5$.

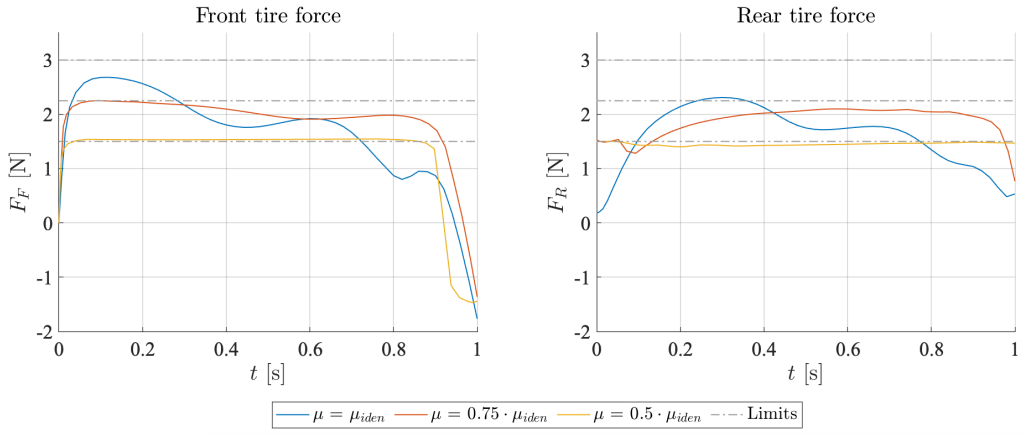

Figure 8-8: Time domain responses of the front and rear resultant tire forces resulting from the trajectory optimization under varying friction coefficients.

8-4 Discussion of the Optimization Results

Although drifting equilibria were obtained in the results, no counter-steer drift equilibria were observed. Even for the highest reference velocity, only under-steer behavior is observed. Figure 8-9 shows the time domain signals of the cornering velocities. It is observed that the reference velocity can be tracked accurately up to $V = 2$ m/s. For higher reference velocities (the green and the purple line), a steep decrease in velocity is present around $t = 0.1$ s. It is assumed that the fact that the cornering velocity is too low is the underlying cause for the absence of counter-steering drift equilibria. This is supported by the observation that counter-steering equilibria only exist for cornering velocities above 2.3 m/s (right graph of Figure 8-2). Three possible causes for the inaccurate tracking of the velocity are discussed in this section.

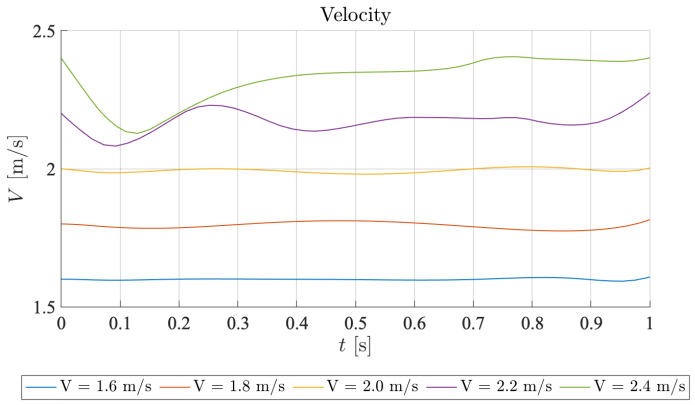

Figure 8-9: Time domain responses of the cornering velocity resulting from the trajectory optimization under varying velocities.

Assumption of small steering angles

In the optimization results, the rear longitudinal force input is found to be negative during the maneuver. In the previous chapter is was explained that this caused by the assumption of small steering angles. When the cornering scenario of $V = 2.4$ m/s is considered, it is observed that the steering angle reaches the maximum angle of $\delta = \frac{\pi}{6}$ rad (30°) (Figure 8-4). Although it is motivated that $\cos\frac{\pi}{6} = 0.86$ only introduces a 14% error, $\sin\frac{\pi}{6} = 0.5$ yields an error of 50%. This implies that the longitudinal component of the front lateral tire force is equal to half the total force. From Figure 8-5 it is observed that the front tire force at this time ($t = 0.2$ s) is approximately 3 N. When the assumption of small steering angles is released (2-18), the longitudinal component ($F_{y,F}\sin\delta$) would equal -1.5 N. If this was to be compensated with $F_{x,R}$, it would almost certainly yield saturation of the rear tire. This is motivated by the observation that the rear tire is already close to the saturation limits (Figure 8-5).

To verify whether the optimization results would change when the assumption of small steering angles is released, the optimization is performed with (2-18) as the expression of the single-track model. The highest velocity scenario $V = 2.4$ m/s is optimized with and without the small steering angle assumption. This velocity is selected since counter-steering equilibria correspond to the highest equilibrium velocities. The results are included in appendix F. The main findings are discussed below.

When the assumption is released, positive values are obtained for the input $F_{x,R}$. Counter-steering drift equilibria, however, are not observed. The results of the optimization do not improve in terms of the cost-function terms(Table F-2). Although the assumption was released to improve the tracking of the velocity, the error becomes bigger (Figure F-7). As a result, the slip angles of the tires and therewith the tire forces decrease. The tires are concluded not to be closer to the friction limits. Smaller side-slip angles are obtained because the velocity is lower.

It must be stated that the cost-function weights are determined based on the assumption of small steering angles. It can be possible that adjusted weights improve the optimization results. This step is not included in this research. With the currently derived weights, it is expected that the assumption of small steering angles is not preventing the optimization from converging to counter-steering drift equilibria.

Cost-function
Another possibility is that the derived cost-function is limiting the convergence. In Table 8-2 it became apparent that increasing the weight of the J_{pos} had a negative effect on the velocity error. As was observed from Figure 8-4, the combination of braking and maximum steering is applied to reduce the error with respect to the reference path. The cost-function terms of the position and velocity are conflicting at this point in the maneuver. Furthermore, the constraints of a zero initial and final yaw rate could be a limiting factor. When a vehicle is negotiating a corner, the yaw rate can physically not be zero. The desire to have zero yaw rate at the beginning and the end of the maneuver can, therefore, be conflicting with the objective of tracking the cornering velocity.

To test whether the statements are true, the optimization scenario of $V_{ref} = 2.4$m/s is performed with two modified cost-functions. The complete comparison of the time domain responded is added in appendix F-5. The main findings are listed below.

- Reduced weight of J_{pos}
  Reducing the weight q_{pos} from 100 to 10 improves tracking of the reference velocity. This comes at the cost of the trajectory tracking. The vehicle is traveling at a wider radius, which requires lower tire forces. As a result, no counter-steering equilibria but only under-steer motion is observed.

- Reduced weight of J_r
  The weight q_r is reduced from 10 to 1, resulting in slightly better tracking of the velocity. Again, this comes at the cost of the trajectory tracking. The motion of the vehicle can be characterized as under-steer

Based on the observations that are stated above, it is assumed that the structure of the cost-function is probably not causing the unexpected optimization results.

Initial conditions
Another explanation could be that the initial conditions provided by the spline optimization limit the solution space of the model-based optimization. The current form of spline optimization uses simplified versions of the vehicle and tire models. The results of the spline optimization did not consist of tire saturation or negative side-slip angles. It would be interesting to study whether different initial conditions could improve the convergence of the

model-based optimization. This is considered to be out of the scope of this work but would be a valuable topic for further research.

8-5 Conclusions

The goal of this chapter is to study whether the characteristics of the drift motion also become apparent in a dynamic driving scenario. Starting from the spline parameterization, the dynamic trajectory optimization is performed using a simulation-based approach. The optimization problem is solved for varying cornering velocities and friction coefficients. Overall, the following conclusions are drawn.

- The results of the trajectory optimization show that the vehicle successfully negotiates the corner while satisfying the posed optimization constraints. It can be concluded that the cost-function terms derived in chapter 6 are suitable for the single corner optimization purpose. Furthermore, different types of vehicle motion are observed. Maneuvers with positive and negative side-slip angles are obtained, indicating that the simulation-based optimization can accurately describe the vehicle dynamics, also at the limits of friction.
- The saturation limits of the tires can be lowered by either increasing the cornering velocity or decreasing the friction coefficient. This causes the vehicle to reach the friction limits in an earlier stage. In order to generate the required tire forces to negotiate the corner, higher slip angles and therewith a negative side-slip angle and a large steering angle are observed. These findings correspond to the conclusions of the steady-state equilibrium analysis. The resemblance is considered to be a verification of the optimization results.
- In the dynamic driving scenario, the drift motion is found to enable the vehicle to reach higher cornering velocities. Furthermore, the drift motion comes with large slip angles which allow for the generation of higher tire forces when the vehicle is driving on low friction surfaces.
- Although the optimization yields maneuvers consisting of drifting, no counter-steer motions ($\beta < 0$, $\delta<0$) are obtained in the first segment of the maneuver. It is assumed that the initial conditions of the model-based optimization limit the convergence towards these solutions. The over-steer equilibria were previously observed to yield the highest steady-state yaw rate. It is expected that an optimization algorithm capable of including over-steer motion will be able to improve the trajectory optimization further.

Chapter 9

Conclusions

In this chapter, the answers to the research questions posed in the introduction are provided. Each section restates the question, followed by the findings of this research.

9-1 Modelling Requirements

- *What are the modeling requirements to describe the drift maneuver accurately?*

The tire model should have the ability to account for force coupling, which makes the directional tire forces dependent on each other. Additionally, the tire model should include the phenomenon of tire saturation. During a drift, the lateral force of the front wheel can be controlled by changing the steering angle. This is not possible for the rear wheels. When the tire is at or near the saturation limit, however, varying the longitudinal force of the tire through the throttle also changes the lateral force generated at the rear wheel. In this way, the yaw dynamics of the vehicle can be controlled. It can, therefore, be assumed that any tire model that includes both force coupling and tire saturation can describe the drift motion. Concerning the vehicle model, the only requirement is that the tire forces dictate the motion. Dynamic vehicle models are, therefore, superior over kinematic models.

In the field of modeling, the possibilities are limited by the computational load of the model. High fidelity models tend to increase computation time, making them less suitable for optimization purposes. For the scope of this thesis, the combination of a single-track model with Dugoff tire was considered to be the best solution to the trade-off between model fidelity and computational load.

9-2 The Drift Motion under Steady-State Conditions

- *What are the advantages of drift equilibria compared to normal driving under the assumption of steady-state conditions*

The analysis of the system equilibria has shown that differences exist between normal driving and drifting. An equilibrium is considered to be a drift motion if the side-slip angle is negative. When all the equilibria for a specific cornering radius are compared, it is observed that drifting corresponds to higher cornering velocities. As a result, the yaw rate is higher. In terms of tire dynamics, the tires are operating closer to, or at, the saturation limits.

The study of the phase portraits revealed that in terms of stability, normal driving and drifting are fundamentally different. Where normal driving is found to be a stable equilibrium, drifts are found to be unstable saddle points. Without any form of control, small deviations from the equilibrium result in an unstable system.

Computation of the controllability matrices has identified that both types of cornering are controllable. In addition to the binary statement of the controllability matrix, an approach based on eigenvalues the Controllability Grammians is presented. Although the approach provides limited information, it allows to conclude on the amount of input energy that is required to control the system in the direction of the eigenvectors. It is observed that for the drift equilibria, the ratio of the eigenvalues is smaller compared to normal equilibria. This indicates that for normal equilibria, there is a main direction of response; other directions can be subjected to robustness issues. It is concluded that the drift motion has the potential to increase the controllability (and the corresponding robustness) of the vehicle motion.

9-3 The Drift Motion in a Dynamic Driving Scenario

- *What are the advantages of the drift motion in a dynamic driving scenario, when the assumption of steady-state cornering conditions is released?*

The multi-objective trajectory optimization is found to yield similar observations as the steady-state analysis. When the tires are pushed towards the saturation limits, negative side-slip angles become apparent in the optimization result. Drifting is observed to allow for higher cornering velocities and therewith higher yaw rates. During a drift, the slip angles of the tire are bigger than during normal driving. When the maximum tire force that can be generated is lower due to low friction, increased slip angles are required to achieve lateral tire forces that are sufficient to negotiate the corner. In this case, the drift motion increases the maneuverability as it facilitates larger slip angles.

It must be noted that the optimization only considers a single corner, under the assumption of various simplifications. Despite the narrow scope of this analysis, the optimization results certainly add to the understanding of the effect drifting has on vehicle maneuverability. When the vehicle is near the limits of friction, either due to a high velocity or due to low friction, large side-slip motion contributes to generating higher tire forces then are possible during low side-slip maneuvers. The tire forces directly determine the vehicle dynamics. The drift motion is, therefore, is concluded to have the ability to increase the operating envelope of the vehicle.

9-4 Main conclusions

This research bridges the gap between the steady-state analysis and a more realistic dynamic driving scenario. A detailed description of the steps towards a multi-objective trajectory optimization is provided. Notwithstanding the encountered limitations of the method, the author is confident that the method presented in this work can contribute to further research on deepening the understanding of drifting and the potential application in autonomous vehicles. The presented work can function as the basis on which future studies can continue in the investigation on how to exploit the full operating envelope of autonomous vehicles.

Chapter 10

Recommendations

This chapter identifies the areas that are interesting for further research. It elaborates on the potential improvements that are expected to yield valuable insights in addition to the results that were presented in the previous chapters.

1. *Vary friction coefficient over the corner segment.* In the current optimization scenario, the friction is assumed to be constant. Since it was concluded that the drift motion is related to the tires reaching the saturation limit, it would be interesting to study how the vehicle reacts to changes in friction. The corner could be divided into two segments, starting on high friction asphalt followed by a mid-corner transition to low friction gravel.

2. *Increase the model fidelity.* The model that is derived in this work consists of multiple simplifications. Increasing the model complexity makes the results of the optimization more accurate compared to reality. The assumption of steering angles has been discussed in the previous chapters. Performing the optimization without this assumption yields a more accurate description of the required throttle input. Motor dynamics could be included, replacing the longitudinal force as input with motor torque. Instead of the single-track model, a double-track model could be implemented. The effect of load transfer could model different saturation limits for each tire.

3. *Change the corner configuration.* Currently, a fixed radius corner with a radius of 1 meter is optimized. There is room for further research to determine the effect of an increased corner radius. The maneuver as it is formulated in this work is a combination of transient and steady-state motion. The cornering segment in which the vehicle can achieve steady-state cornering is relatively small compared to the entire trajectory. The length of the segments directly depends on the cornering radius, which determines the circumference and therewith the length of the trajectory. Another interesting concept would be to vary the cornering radius over the trajectory. In this way, clothoid trajectories can be simulated.

4. *Improve the initial conditions provided by the spline optimization condition.* In this work, the same initial conditions resulting from a single spline optimization are used for all optimization scenarios. The cornering velocity and friction coefficient are not varied in the spline optimization. Additionally, the spline optimization used the linear tire model to reduce the model complexity. This is decided since the spline optimization was found not to satisfy the dynamics incorporated in the nonlinear constraints. Another improvement could be made by optimizing the number of spline segments that are used to parameterize the continuous-time signals. Future research is required to establish if these modifications allow for exploring a larger portion of the operating envelope than is possible with the approach discussed in this work.

5. *Solve the optimization on a device with a bigger computational power.* Designing the optimization was a constant trade-off between accuracy and computational time. Having a device with more computation power allows increasing the complexity of the model. Furthermore, the discrete-time steps can be decreased, which is expected to be especially beneficial to the spline optimization.

6. *Deeper analysis of the Controllability Grammian eigenvectors.* The analysis based on the Controllability Grammian focused on the ratio between the eigenvalues. It would be valuable to include the direction of the corresponding eigenvectors in terms of the system states. Such an approach could yield insights into the states that could be controlled at each equilibria, and how much input energy is required to do so. Supported by the unstable nature of the drift motion, it is expected that especially the side-slip angle could be controlled with less input energy when the vehicle is already sliding to a certain degree.

7. *Refinement of weight sensitivity analysis* In the weight sensitivity analysis, the value of the weights increase exponentially. It can be interesting to refine the weight sensitivity and study whether smaller adjustments to the weights yields improvement in terms of the cost function terms. Furthermore, the weights analysis only considers one cornering velocity. Tuning the cost-function weights for specific cornering velocities could potentially improve the convergence of the optimization.

Appendix A

BARC Structure

This appendix provides an overview of the components that are installed on the Berkeley Autonomous Race Car (BARC). This test platform is developed at Berkeley University of California. More information on the BARC project can be found on the Github. The schematic overview of the scaled vehicle is presented in Figure A-1. The numbers correspond with the overview of the electronics architecture, shown in Figure A-2

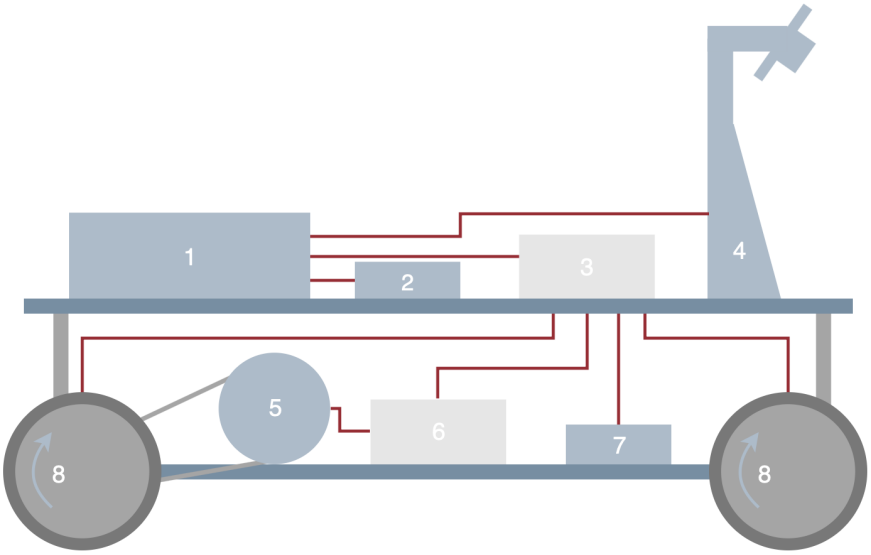

Figure A-1: Schematic overview of individual components that form the BARC.

The BARC is equipped with a set of sensors and actuators (Figure A-2). The operating system of the scaled vehicle is installed on the Odroid, which can communicate with a remote computer through the use of a WiFi router. The Odroid directly receives the measurement signals from the Internal Measuring Unit (IMU) and the camera. The latter component is installed on the vehicle, however, not used in this work. Measurement of the other sensors,

the wheel encoders, are sent via the Arduino. That same Arduino is used to send the control inputs to the Electronic Control Unit (ECU) and the steering servo.

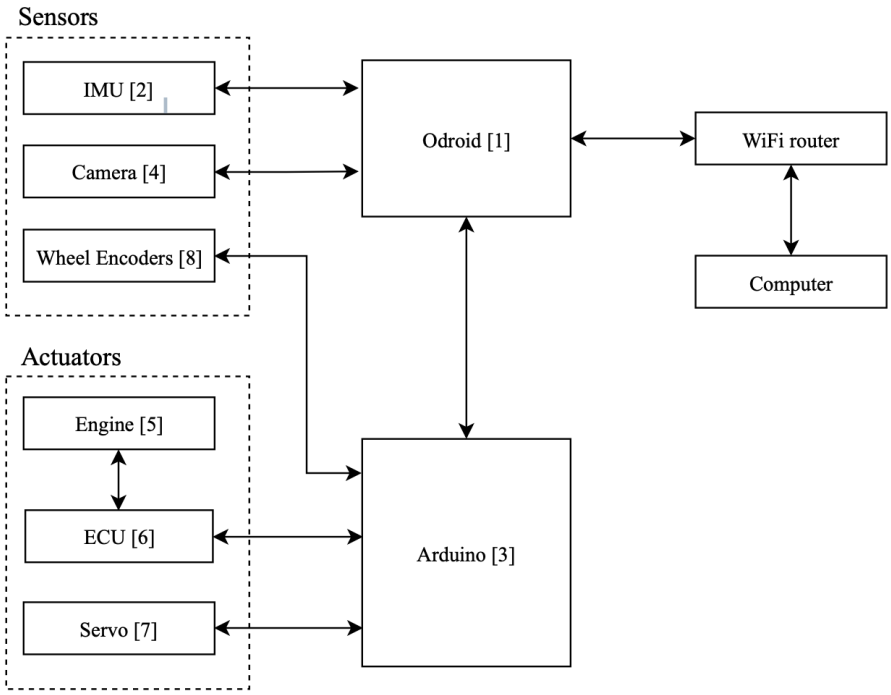

Figure A-2: Schematic overview of the electronics of the BARC.

For more detailed descriptions about the components, an overview of the components and the corresponding link to the web-page of the manufacturer is provided (Table A-1).

Table A-1: List of components and the corresponding links to the manufacturer web-pages.

#	Component	Link
1	Odroid	http://ameridroid.com/products/odroid-xu4
2	IMU	http://ameridroid.com/products/myahrs
3	Arduino	https://store.arduino.cc/arduino-nano
4	Camera	https://www.amazon.com/ELP-Driver-Camera-Module
5	Engine	https://hobbyking.com/nl_nl/rz-4-v2-kit.html
6	ECU	https://hobbyking.com/nl_nl/rz-4-v2-kit.html
7	Steering servo	http://www.rchobbyestore.co.uk/servo
8	Wheel encoders	https://www.sparkfun.com/products/9312

Appendix B

BARC Measurements

The process of parameter identification is discussed in chapter 4. It was mentioned that both the wheel diameter and the mass moment of inertia were calculated based on measurements. This appendix provides an overview of the measurements that were used for this purpose. Furthermore, a static steering identification is performed in addition to the dynamic identification. The methodology and results are presented in section B-3.

B-1 Wheel Diameter

Accurately measuring the wheel diameter is crucial for the model identification. Any mismatch will yield incorrect longitudinal velocity data. Therefore, the wheel diameters are measured three times, and the average of these values are used.

Table B-1: Measurements of wheel diameters, expressed in [mm]

	Front Left	**Front Right**	**Rear Left**	**Rear Right**
1	67.24	66.88	66.95	66.84
2	66.99	66.88	66.82	66.78
3	67.02	66.91	66.91	66.83
Average	67.08	66.89	66.89	66.82

B-2 Mass Moment of Inertia

The mass moment of inertia is calculated based on the method that was presented in [17]. The vehicle is suspended by two wires and slightly rotated. The motion can be approximated by the dynamics of the bifilar pendulum (Figure B-1).

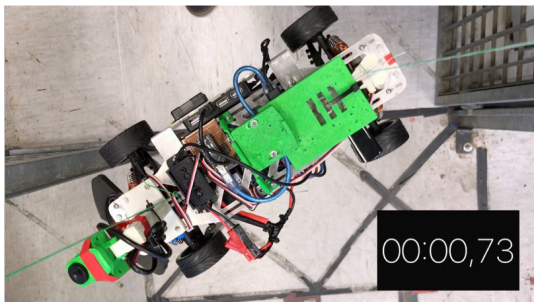

(a) Most left position

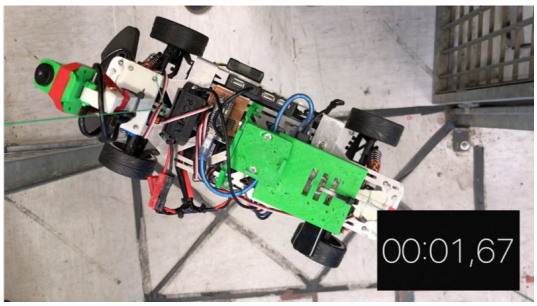

(b) Most right position

Figure B-1: Examples of two video frames in which the vehicle (suspended by wires) reaches the maximum angle of rotation.

Every time the vehicle reaches the outer position of the rotation, the rotational velocity will be zero. Measuring the time between two of these time instance allows to determine the frequency of the oscillation. An overview of the measurements is presented in Table B-2.

In this table, the time at the outer left position is denoted by t_{left}, for the right side, the symbol t_{right} is used. From the measurements, it is computed that the average time between the maximum angles of rotation equals $\Delta t = 0.95$ s. This yields a frequency of oscillation equal to $\omega_n = 3.29$ Hz. The resulting frequency is used in chapter 4 to compute the mass moment of inertia.

Table B-2: Time instances, expressed in [s], at which the rotational velocity of the vehicle is zero.

	$\mathbf{t_{left}}$	$\mathbf{t_{right}}$	$\mathbf{\Delta t}$
1	0.73	1.67	0.94
2	2.65	3.61	0.96
3	4.57	5.51	0.94
4	6.50	7.46	0.96
5	8.44	9.42	0.98
6	10.37	11.32	0.95
7	12.28	13.23	0.95
8	14.20	15.21	1.01
9	16.18	17.12	0.94
10	18.13	19.08	0.95
11	20.05	21.00	0.95
12	21.98	22.91	0.93
Average	-	-	0.955

B-3 Static Steering Identification

In order to verify the dynamic identification result, a static (zero velocity) experiment was performed. A sinusoidal signal was sent to the servo, and the steering angle resulting from

this input was captured with video recording. The steering angle is recovered from the video frame using a protractor, which center is aligning with the steering point of the wheel. The alignment of the wheel is slightly toe-out, which means that both tires face to the outside of the vehicle. As a result, different angles are obtained from the left and right wheel for a specific steering angle. The average of the two angles is used as an estimation of the total δ. A timer is added to allow for determining the time instances of the frames.

First of all, the maximum steering angles are studied. The input signal of the steering servo has an amplitude which is significantly large to guarantee that the servo will reach the boundaries. In this case, more steering input no longer yields a larger steering angle; the steering is saturated. Studying the video frames at which the steering enters and leave the saturation regions, the maximum steering angles are found to be equal to 0.42 rad (24°) for steering left and -0.30 rad ($-17°$) for steering right Figure B-2. It must be noted that due to the angular movement of the tire, the vehicle was moving slightly. As a result, the alignment of the camera changed. The accuracy of this approach is, therefore, limited.

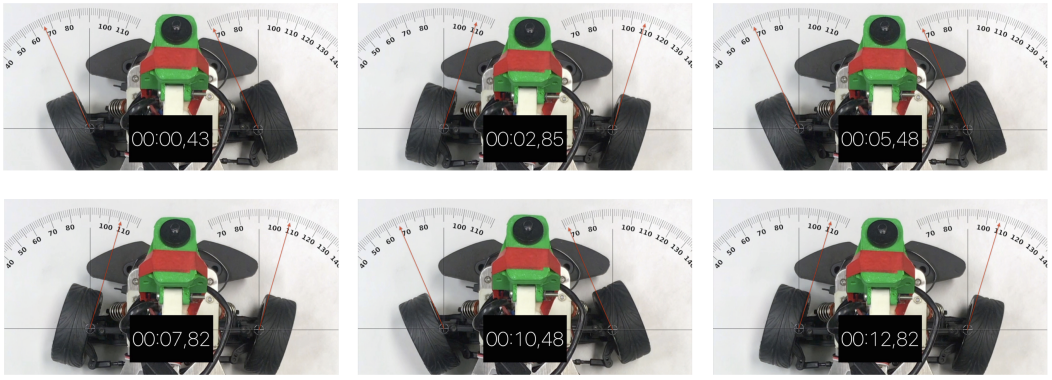

Figure B-2: Video frames of the time instance where the steering wheel enters and leaves the saturated region.

To obtain the servo input values corresponding to the steering limits, the time instances at which the steering mechanism enters and leaves the saturation region are plotted together with the steering input (Figure B-3). The dashed red line represents the neutral steering input for which the steering angle is zero, 90.88. The steering boundaries for both sides are indicated by the grey dashed line. Although a sinusoidal signal was sent to the Arduino, the signal that reaches the servo shows similarities with a trapezoidal signal. This is caused by the internal servo dynamics. The Arduino translates the signal such that the servo output is sinusoidal. It is found that the servo input that corresponds to the left and right saturation are 132 and 43, respectively. Additionally, it can be observed that the time of the video frames that correspond with entering and leaving the steering saturation are not exactly on the boundary lines. This is due to play in the steering mechanism, causing steering delay, which will be discussed later on.

The saturation regions are therewith found. In order to identify the input-output relationship of the servo, the steering angles at intermediate inputs are studied. The range between the neutral steering point and the saturation limits is explored in discrete steps. For steering to the right the inputs $u_{servo} = \{80, 70, 60, 50\}$ are considered (Figure B-5). For the opposite side, the inputs are $u_{servo} = \{100, 110, 120\}$ (Figure B-4). These data points, together with

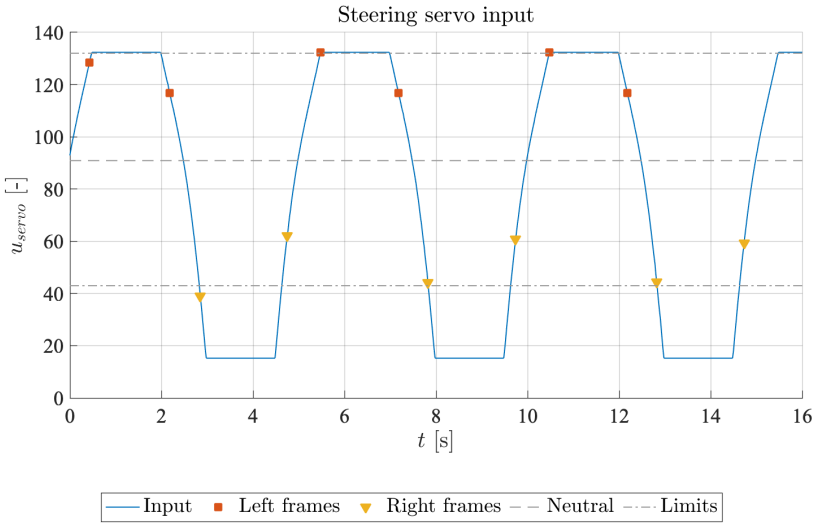

Figure B-3: Sinusoidal input signal that is applied to the steering servo in the static experiment. The dots represent the time instances where the steering enters and leave the saturated region.

the saturation regions, are used for the static steering identification.

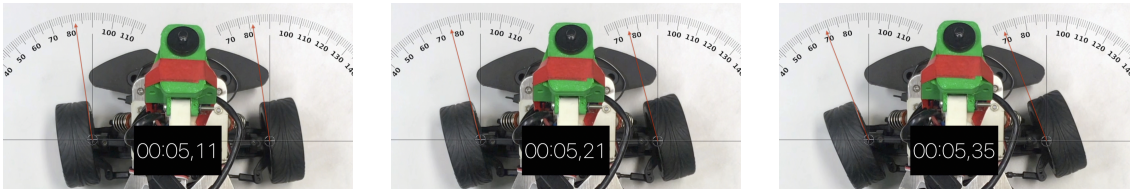

(a) 100 **(b)** 110 **(c)** 120

Figure B-4: Sequence of video frames that correspond to steering towards left steering limit.

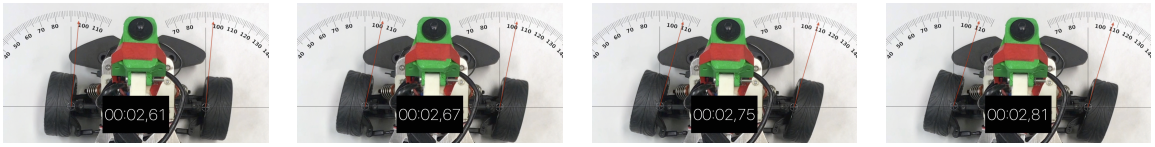

(a) 80 **(b)** 70 **(c)** 60 **(d)** 50

Figure B-5: Sequence of video frames that correspond to steering towards right steering limit.

The new steering identification is now obtained by finding the coefficients c_1, c_2, c_3 and c_4 of (B-1). The estimated steering angle based on the static method is denoted by $\hat{\delta}_s$ The results are displayed in Figure B-6.

$$\hat{\delta}_{s,left} = \min\left(c_1, c_2, (u_{servo} - 90.88)\right) \tag{B-1}$$

$$\hat{\delta}_{s,right} = \max\left(c_3, c_4, (u_{servo} - 90.88)\right) \tag{B-2}$$

The resulting fit is displayed in Figure B-6. Although higher maximum steering angles are

found, the usability of the steering fit is questionable. Under dynamic load, the acting tire forces will affect the steering angle. This phenomenon does influence the vehicle dynamics, and this is something that needs to be included in the model. Therefore the dynamic steering model is used in the thesis.

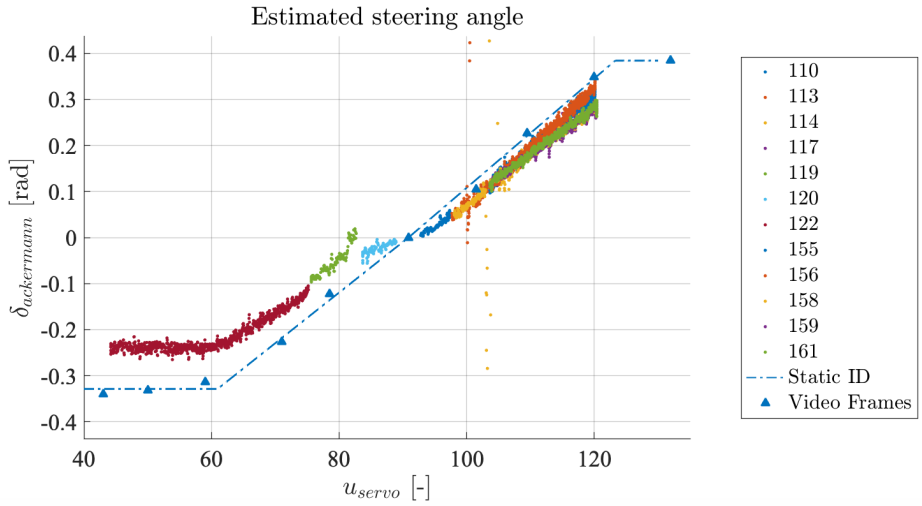

Figure B-6: Input-output relationship resulting resulting from the static steering identification. The blue triangles correspond to the video frames.

Appendix C

Input Dependency of the Cost-Function

The model-based optimization was discussed in chapter 6. It is briefly addressed how the two model inputs, the steering rate $\dot{\delta}$ and the rear longitudinal force $F_{x,R}$ influence the cost-function terms. This appendix contains an extensive explanation based on the system dynamics. The fact that the system consists of a nonlinear tire model makes it more complicated to express input-output relationships. This appendix sets out to describe the dependency as accurate as possible.

The cost-function of 6 consists of four different terms.

- The position of the vehicle, expressed in inertial coordinates $x_{inertial}$ and $y_{inertial}$
- The velocity along the trajectory V
- The yaw rate $\dot{\psi}$ (r)
- The rate of the side-slip angle $\dot{\beta}$

Note that the position of the vehicle in the inertial coordinate frame is considered. The identified vehicle and tire model, however, are based on the body orientate reference frame. The first step in understanding the relationship between the control inputs and the cost function terms is, therefore, to perform the state transformation from inertial to body-orientated reference frame (C-1).

$$u = \dot{x}_{inertial}\cos(\psi) - \dot{y}_{inertial}\sin(\psi) \tag{C-1}$$
$$v = \dot{y}_{inertial}\cos(\psi) + \dot{y}_{inertial}\sin(\psi) \tag{C-2}$$

The longitudinal and lateral dynamics are described as:

$$ma_x = \sum F_x, \tag{C-3}$$
$$m\left(\dot{u} - v\dot{\psi}\right) = F_{y,F}\sin(\delta) + F_{x,R}, \tag{C-4}$$
$$\dot{u} = \tfrac{1}{m}\left(F_{y,F}\sin(\delta) + F_{x,R}\right) + v\dot{\psi}, \tag{C-5}$$

$$ma_y = \sum F_y, \tag{C-6}$$
$$m\left(\dot{v} - u\dot{\psi}\right) = F_{y,F}cos(\delta) + F_{y,R}, \tag{C-7}$$
$$\dot{v} = \tfrac{1}{m}\left(F_{y,F}cos(\delta) + F_{y,R}\right) + u\dot{\psi}. \tag{C-8}$$

Based on the longitudinal (u) and lateral velocity (v) of the vehicle, the dynamics of the yaw rate and the side-slip angle can be expressed (C-9).

$$\beta = \arctan\left(\tfrac{v}{u}\right) \tag{C-9}$$

The yaw rate is depending on the tire forces and the steering angle:

$$I_z\ddot{\psi} = \sum M_z, \tag{C-10}$$
$$\ddot{\psi} = \tfrac{1}{I_z}\left(l_F F_{y,F}\cos(\delta) - l_R F_{y,R}\right). \tag{C-11}$$

The expression of the lateral tire forces that are used in the model-based simulations read as:

$$F_{y,F} = C_{\alpha_F}\tan(\alpha_F)\, f(\zeta), \tag{C-12}$$
$$F_{y,R} = C_{\alpha_R}\tan(\alpha_R)\, f(\zeta). \tag{C-13}$$

Here, $f(\zeta)$ is the nonlinear component that accounts for the tire saturation (C-14).

$$f(\zeta_i) = \begin{cases} \zeta_i(2-\zeta_i) & \text{if } \zeta_i < 1 \\ 1 & \text{else} \end{cases} \qquad i = \{F, R\} \tag{C-14}$$
$$\zeta_i = \eta e_\mu \mu F_{z,i} \frac{1}{2\sqrt{\left(C_{\alpha,i}\tan(\alpha_i)\right)^2}} \qquad i = \{F, R\} \tag{C-15}$$

For the front wheels, η will always be zero as only the rear wheels are driven. For the rear wheels, η is defined as:

$$\eta = \frac{\sqrt{\left(e_\mu \mu F_{z,R}\right)^2 - F_{x,R}^2}}{e_\mu \mu F_{z,R}}. \tag{C-16}$$

The lateral slip angles of the tires are:

$$\alpha_F = \delta + \arctan\left(\frac{V_{wheel,y}}{V_{wheel,x}}\right), \tag{C-17}$$

$$\alpha_R = \arctan\left(\frac{V_{wheel,y}}{V_{wheel,x}}\right). \tag{C-18}$$

Since the track-width of the bicycle model is zero, the longitudinal velocities of the front and rear tire equal the velocity of the body u. The lateral velocities, however, depend on the yaw rate (C-19).

$$V_{wheel,F,y} = v + l_F\dot{\psi} \tag{C-19}$$

$$V_{wheel,R,y} = v - l_R\dot{\psi} \tag{C-20}$$

With all the relevant variables expressed in the presented equations, it can be analyzed which of the inputs can affect each of the cost-function terms. The lateral slip angles of the tire depend on the steering angle and through the wheel velocities on the longitudinal velocity, the lateral velocity, and the yaw rate. In combination with the definitions of the wheel velocities, the original expression (C-17) can be summarized as:

$$\alpha_F = f_{\alpha_F}\left(\delta, V_{wheel,F,x}, V_{wheel,F,y}\right) = f_{\alpha_F}\left(\delta, u, v, \dot{\psi}\right) = f_{\alpha_F}\left(\delta, \dot{x}, \dot{y}, \dot{\psi}, \psi\right), \tag{C-21}$$

$$\alpha_R = f_{\alpha_R}\left(V_{wheel,R,x}, V_{wheel,R,y}\right) = f_{\alpha_R}\left(u, v, \dot{\psi}\right) = f_{\alpha_R}\left(\dot{x}, \dot{y}, \dot{\psi}, \psi\right). \tag{C-22}$$

Continuing this way of reasoning, the next formulas that are rewritten are those of the tire forces. In addition to the lateral slip angles, extra parameters are introduced through $f(\zeta)$ (C-14). Through the force coupling term η, the dependency on the longitudinal tire force appears. However, since longitudinal dynamics are considered to be out of the scope, this force coupling effect only applies to the rear tires. This yields the following expressions of the lateral tire forces:

$$F_{y,F} = f_{F_{y,F}}\left(\alpha_F, \zeta_F\right) = f_{F_{y,F}}\left(\alpha_F, \eta_F\right) = f_{F_{y,F}}\left(\delta, \dot{x}, \dot{y}, \dot{\psi}, \psi\right), \tag{C-23}$$

$$F_{y,R} = f_{F_{y,R}}\left(\alpha_R, \zeta_R\right) = f_{F_{y,R}}\left(\alpha_R, \eta_R\right) = f_{F_{y,R}}\left(F_{x,R}, \dot{x}, \dot{y}, \dot{\psi}, \psi\right). \tag{C-24}$$

Referring to the original inputs, it can be observed that the front and rear lateral tire force can be controlled using the steering and throttle inputs respectively. With the renewed expression of the tire force, it is possible to conclude on the relationship between the inputs and the cost-function term.

Yaw rate

The yaw rate is obvious since it depends directly on the tire forces. The yaw dynamics

provided an expression for the yaw acceleration, which provides information on how the yaw rate changes. The tire forces (C-23) are substituted in the yaw dynamics (C-10).

$$\ddot{\psi} = \quad f_{\ddot{\psi}}\left(\delta, F_{y,F}, F_{y,R}\right) = f_{\ddot{\psi}}\left(\delta, F_{x,R}, \dot{x}, \dot{y}, \dot{\psi}, \psi\right) \tag{C-25}$$

The first observation is that the yaw acceleration depends on each of the control inputs since both the steering angle (δ) and the rear longitudinal tire force ($F_{x,R}$) appear in $f_{\ddot{\psi}}$. Furthermore, the yaw dynamics depend on the velocities in the inertial reference frame. The cost-functions of the position (J_{pos}) and the yaw rate ($J_{\dot{\psi}}$) are thus to some degree dependent on each other.

Position

The transformation between the inertial and body-orientated reference frames showed that the velocities in one reference frame depend on the velocity in the other frame, together with the yaw angle. Consider the expression of the longitudinal ((C-3)) and lateral ((C-6)) dynamics. With the previously derived dependencies, the formulas can be written into:

$$\dot{u} = \quad f_u\left(\delta, F_{x,R}, F_{y,F}, v, \dot{\psi}\right) = f_u\left(\delta, F_{x,R}, \dot{x}, \dot{y}, \dot{\psi}, \psi\right) \tag{C-26}$$

$$\dot{v} = \quad f_v\left(\delta, F_{y,F}, F_{y,R}, u, \dot{\psi}\right) = f_v\left(\delta, F_{x,R}, \dot{x}, \dot{y}, \dot{\psi}, \psi\right) \tag{C-27}$$

Under the assumption that the acceleration of a vehicle determines the velocity, and the velocity then determines the position, it is concluded that the parameters that can change the acceleration will also be the parameters that change the position. Combining this idea with the observation that the transformation from the body-orientated reference from to the inertial frame only add the yaw angle ψ allows to conclude the dependency of the position cost-function term. It is concluded that both the steering rate and the rear longitudinal force can influence the position of the vehicle.

Velocity

The cornering velocity is defined as the $V = \sqrt{u^2 + v^2}$. Since the dependencies of both the longitudinal and lateral accelerations, and therewith the velocities, are already known, it is concluded that both inputs can change the cornering velocity. This is derived under the assumption that u and v depend on the same variables as $\dot{u}$ and $\dot{v}$.

$$V = \quad f_V\left(u, v\right) = f_u\left(\delta, F_{x,R}, , \dot{x}, \dot{y}, \dot{\psi}, \psi\right) \tag{C-28}$$

$$\tag{C-29}$$

Side slip rate

The side-slip angle only depends on the longitudinal and lateral velocity (C-9). The side-slip rate, therefore, depends on the velocities and their time derivatives in the body-orientated frame. Following the same reasoning as was applied in the previous section, it can be concluded that the steering and throttle commands can influence the side-slip rate.

$$\dot{\beta} = \quad f_{\dot{\beta}}\left(u, v, \dot{u}, \dot{v}\right) = f_u\left(\delta, F_{x,R}, , \dot{x}, \dot{y}, \dot{\psi}, \psi\right) \tag{C-30}$$

Appendix D

Sequential Quadratic Programming Algorithm

This appendix provides a detailed description of the Sequential Quadratic Programming (SQP) algorithm that is used in the trajectory optimization. The method is discussed in [14, 15]. The algorithm is a nonlinear programming method that converges to the solution in a number of iterations. At each iteration, an approximation of the Hessian matrix of the Lagrangian function is made, which is used to form a quadratic programming sub-problem. The solution to this problem is used in a line search to obtain the new iterate. Before the individual steps of the algorithm is discussed, first the definition of the Lagrangian function is explained.

D-1 Lagrangian Function

Since the SQP algorithm approximates the Lagrangian function, this section will provide an overview of the definition and the way it is used in optimization strategies. Consider the classical constrained optimization problem that is written as

$$\min f(x) \tag{D-1}$$

$$\text{subject to} \quad \begin{cases} c(x) \leq 0 \\ c_{eq} = 0 \\ Ax \leq 0 \\ A_{eq}x = b_{eq} \\ LB \leq x \leq UB. \end{cases} \tag{D-2}$$

Here $c(x)$ represent the nonlinear inequality constraint, $c_{eq}(x)$ the nonlinear equality constraints. The linear inequality and equality are described by $Ax \leq 0$ and $A_{eq}x = b_{eq}$ respectively. Finally, LB and UB correspond to the lower and upper bounds.

A common approach to finding a local minimum or maximum for such a problem is to apply the method of Lagrange multipliers. The general concept revolves around restructuring the constrained problem in such a way that stationary point can be obtained from analyzing where the derivative of the function is zero.

According to the Lagrange multiplier theorem, any stationary points where the constraints are satisfied can be written as a linear combination of the gradient of the constraints and the Lagrangian multipliers. Consider the following Lagrangian function.

$$\mathcal{L} = f(x) - \sum_{i=1}^{m} \lambda_i g_i(x) \tag{D-3}$$

In this expression λ_i is the i-th Lagrange multiplier and $g_i(x)$ denotes the i-th constraint. In order to find the stationary points where also the constraints are satisfied, the following conditions should hold:

$$\nabla \mathcal{L}(x, \lambda) = \nabla f(x) - \sum_{i=1}^{m} \lambda_i \nabla g_i(x) = \quad 0 \tag{D-4}$$

$$g_i(x) = \quad 0 \tag{D-5}$$

It is important to note that the stationary points resulting from the Lagrangian multipliers method can only be considered to be a local minimum or maximum.

D-2 Algorithm Description

The introduction already stated that the SQP consists of multiple steps that are performed each iteration. A detailed description of each step is provided in this section.

Update of the Hessian matrix
The Hessian of the Lagrangian function is approximated by computing the quasi-Newton approximation.

$$H_{k+1} = H_k + \frac{q_k q_k^T}{q_k^T q_k} - \frac{H_k s_k s_k^T H_k^T}{s_k^T H_k s_k} \tag{D-6}$$

$$s_k = x_{k+1} - x_k \tag{D-7}$$

$$q_k = \left(\nabla f(x_{k+1}) + \textstyle\sum_{i=1}^{m} \lambda_i \cdot \nabla g_i(x_{k+1})\right) - \left(\nabla f(x_k) + \textstyle\sum_{i=1}^{m} \lambda_i \cdot \nabla g_i(x_k)\right) \tag{D-8}$$

Here, s_k is the difference between two iterates and q_k is the change in Lagrangian functions.

Solution to the Quadratic Programming problem
Based on the update Hessian, a new Quadratic Programming sub-problem is formulated.

$$\min q(d) = \frac{1}{2} d^T H_k d + c^T d \tag{D-9}$$

$$A_i d = b_i, \qquad i = 1, \cdots, m_c \tag{D-10}$$

$$A_i d \leq b_i, \qquad i = m_c, \cdots, m \tag{D-11}$$

To find a solution to the sub-problem, first a feasible point d is searched. Then, an iterative sequence of feasible points is calculated that converges to the solution of the sub-problem.

Line search
The solution d_k, obtained in the previous, is used in a line search to generate the new iterate x_{k+1}.

$$x_{k+1} = x_k + \alpha_k d_k \tag{D-12}$$

The parameters α_k represents the step length, which is determined based on the decrease of a merit function, defined by [18, 28].

Appendix E

Global Search Algorithm

This appendix discusses the algorithm that is used to find the best solution to the spline optimization problem. A global search method is implemented, which solves the constrained optimization various times.

E-1 Types of Global Search Algorithms

The result that is obtained from an optimization depends strongly on the initial values of the optimization parameters. One option to overcome this limitation is to think of a method to choose the initial values. However, the result of the optimization is then directly limited by the initial values that are selected. Another option is to use a global search algorithm, which does multiple trial runs and select the best result as the final solution to the optimization problem. The fact that the global search algorithm performs multiple runs, with different initial values, is appealing since this increase the chance that the algorithm finds the best solution. The optimality only applies to all the trial points that are investigated by the algorithm. It is, therefore, possible that there exist solutions that could yield slightly better results.

Various global search algorithms are available. However, the majority of them can be divided into two categories. The first type is the multi-start approach, where a set of initial optimization variables is computed, referred to as trial points. The optimization is run for each trial point, and afterward, the best results in terms of objective function and constraints are selected to be the global solution. The other type of global search algorithm differs from the multi-start approach in the sense that not all trial points are evaluated. The initial conditions are compared to each other to reduce the number of trial points that are run, to minimize the computation time of the algorithm. The latter type of global search algorithms is used to solve the spline optimization. The working principle of the algorithm will be discussed int his section.

E-2 Working Principle

The global search method is described by four phases [35]. It works with the concept of basins, areas in the solution-space in which the states converge to a local optimum. Through analysis of different trial points, the space is divided into various basins. The center of each basis represents the corresponding local optimum. It could be imaged as a funnel. When it is known that a specific trial point falls into one of the defined basis (the funnel), it will end up in the same local optimum that was already obtained. There, the trial point does not need to be evaluated. This way, a large number of trial points can efficiently be evaluated without ending up in the same optimum multiple times. The four phases of the algorithm are summarized below.

1. Initialization
   The algorithm runs the constrained optimization for the initial values provided by the user. The first run gets a score that is defined by the final objective function and a term that accounts for any violation of the constraints.

   A set of trial points is found using scatter search [16]. For each trial point, the objective function is computed, and the highest one is selected to be the stage 1 starting point. The optimization is run for this point. The two runs performed so far, the initial conditions and the first trial point, are used to define the location and radius of the basins of attraction.

   The basins of attraction are considered to be spherical. Two basins are formed; one belonging to the initial run and one to the first trial point run. The radius of each basin is equal to the distance between the initial and final optimization variable values. Additionally, two counters are defined. The first equal the number of consecutive trial points that lie within the basin, the second is the number of trial points that have objective function higher than the threshold.

2. Stage 1
   With the basins and counters defined, all the remaining trial points are evaluated. After each run, the basins and counters are updated.

3. Stage 2
   In stage 2, the remaining trial points, equal to the total number of trial points minus the stage 1 points, are considered. Of these points, those that satisfy the following conditions are run:

   - The trial point does not lie within one of the existing basins
   - The initial objective function evaluation is smaller than the current threshold
   - The trial point satisfies the bounds and inequality constraints that are provided to the optimization algorithm

   When a trial point is run, the basin is only updated when the final result, after convergence, is different from previously obtained optima.

If the trial point does not run, the counters of the basin, in which the trial point is located, are updated. If the counter reaches the maximum value, the radius of the basin is reduced.

4. Formulation of the global solution
   The optima, belonging to each basin, are ordered smallest to largest based on the objective function. The smallest one is selected to be the results of the global search.

E-3 Tuning the Algorithm

The two-stage structure of the optimization algorithm provides the possibility to tune the algorithm. The user can define the number of trial points that are evaluated in both stages. Stage 1 evaluates all trial points. In stage 2, however, only those trial points that satisfy the conditions of the bounds and inequality are evaluated. The number of stage 1 trials is reduced, from the default number 2e2 to 1e1. The total number of trial points is set equal to 1e4. This way, the majority of trial points are evaluated based on bounds and inequality constraint. These modifications increase the time efficiency of the global search optimization.

Another fundamental aspect of the global search method is the formulation of the basins of convergence and the reduction of their radii during the evaluation of the trial points. The variables that determine the speed of the radius reduction are therefore, interesting parameters to study. It is decided that this is not within the scope of this thesis.

Appendix F

Simulation-Based Optimization Results

This appendix consists of the results of the trajectory optimization. The results are presented based on the analyses that are discussed in chapter 6.

Variation of the Cornering Velocity
To make a comparison with the steady-state cornering equilibria, the velocity at which the corner is negotiated is varied. The set $V = \{1.6,\ 1.8,\ 2.0,\ 2.2,\ 2.4\}$ is considered. The signals that describe the vehicle dynamics are displayed in Figure F-1. The lateral slip angles and tire forces are depicted in Figure F-2.

Variation of the Friction Coefficient
In order to simulate different types of surface, the optimization is performed with varying friction coefficient. The starting point is the identified friction coefficient μ_{iden}, which is then gradually decreased. An overview of the vehicle and tire dynamics are displayed in Figure F-3 and Figure F-4, respectively.

Variation of the Cost-Function
In chapter 8 it is discussed that no counter-steering drift maneuver are observed. The hypothesis is formulated that the cost-function weights, as derived in section 6-2, prevent the algorithm from converging to the counter-steer equilibria. In order to test the hypothesis, the optimization is performed with slightly modified cost-functions. Three scenarios are considered:

- *Normal weights*
  This is the cost-function that was derived in section 6-2.
- *Reduced yaw rate weight*
  The weight q_r that is applied to the yaw rate cost-function term J_r is reduced from 10 to 1. The resulting cost-function reads as $J = 100 \cdot J_{pos} + 10 \cdot J_V + J_r + J_{\dot{\beta}}$.

- Reduced position weight
  The weight q_{pos}, which corresponds to the position cost-function term J_{pos}, is reduced from 100 to 10. This yields $J = 10 \cdot J_{pos} + 10 \cdot J_V + 10 \cdot J_r + J_{\dot{\beta}}$.

The resulting vehicle dynamics are displayed in Figure F-5, the corresponding tire dynamics can be found in Figure F-6. A comparison of the cost-function terms is presented in Table F-1.

Assessing the effect of the small steering angle assumption
The scenario in which the reference velocity is $V_{ref} = 2.4$ m/s is solved with and without the assumption of small steering angles. The aim of the analysis is to verify the assumption and to study whether it limits the convergence of the algorithm towards counter-steering equilibria.

The resulting vehicle dynamics are displayed in Figure F-7, the corresponding tire dynamics can be found in Figure F-8. A comparison of the cost-function terms is presented in Table F-10.

F-1 Variation of the Cornering Velocity - Vehicle Dynamics

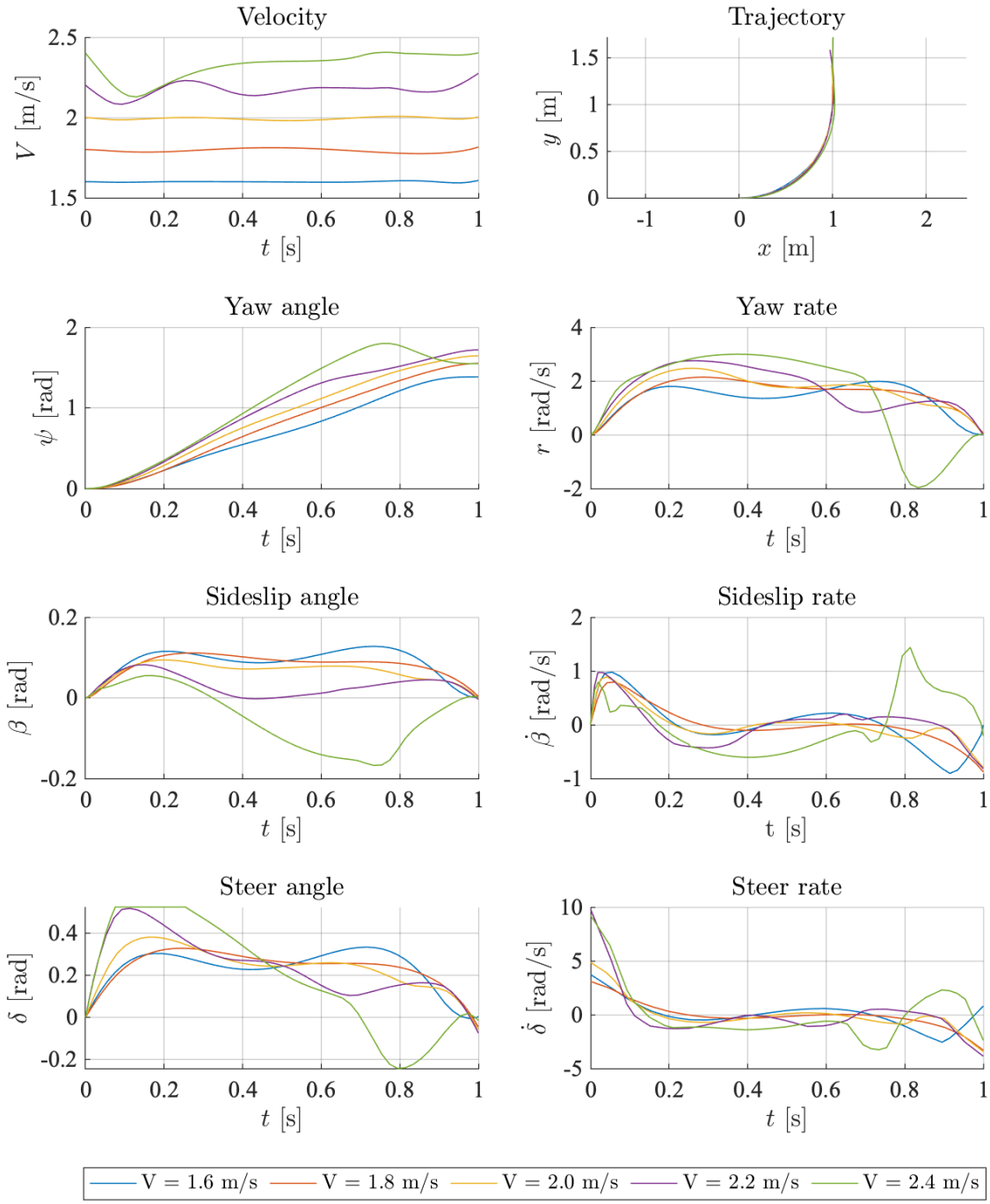

Figure F-1: Overview of the time domain responses describing the vehicle dynamics resulting from the trajectory optimization under varying cornering velocities.

F-2 Variation of the Cornering Velocity - Tire Dynamics

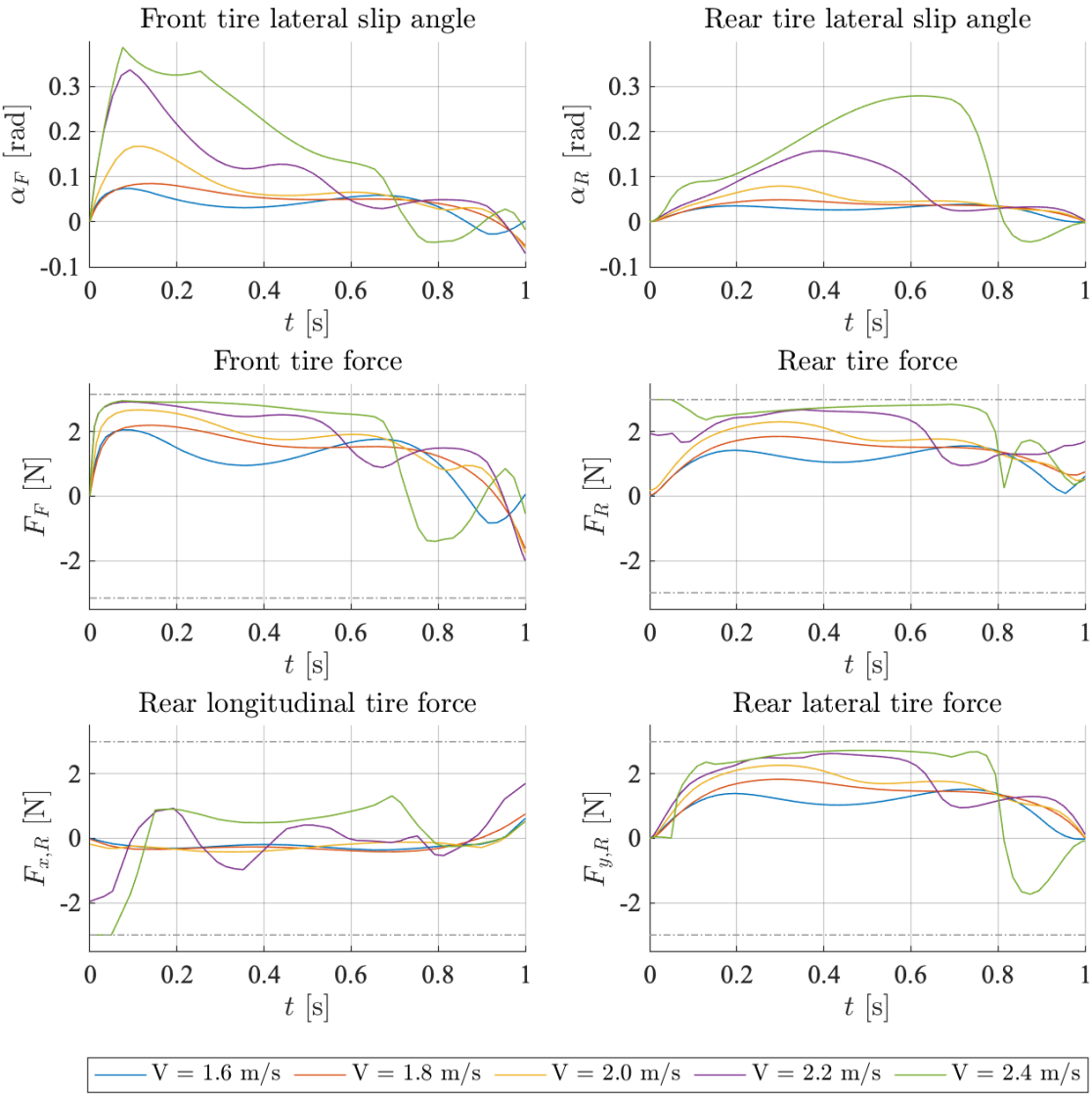

Figure F-2: Overview of the time domain responses describing the tire dynamics resulting from the trajectory optimization under varying cornering velocities.

F-3 Variation of the Friction Coefficient - Vehicle Dynamics

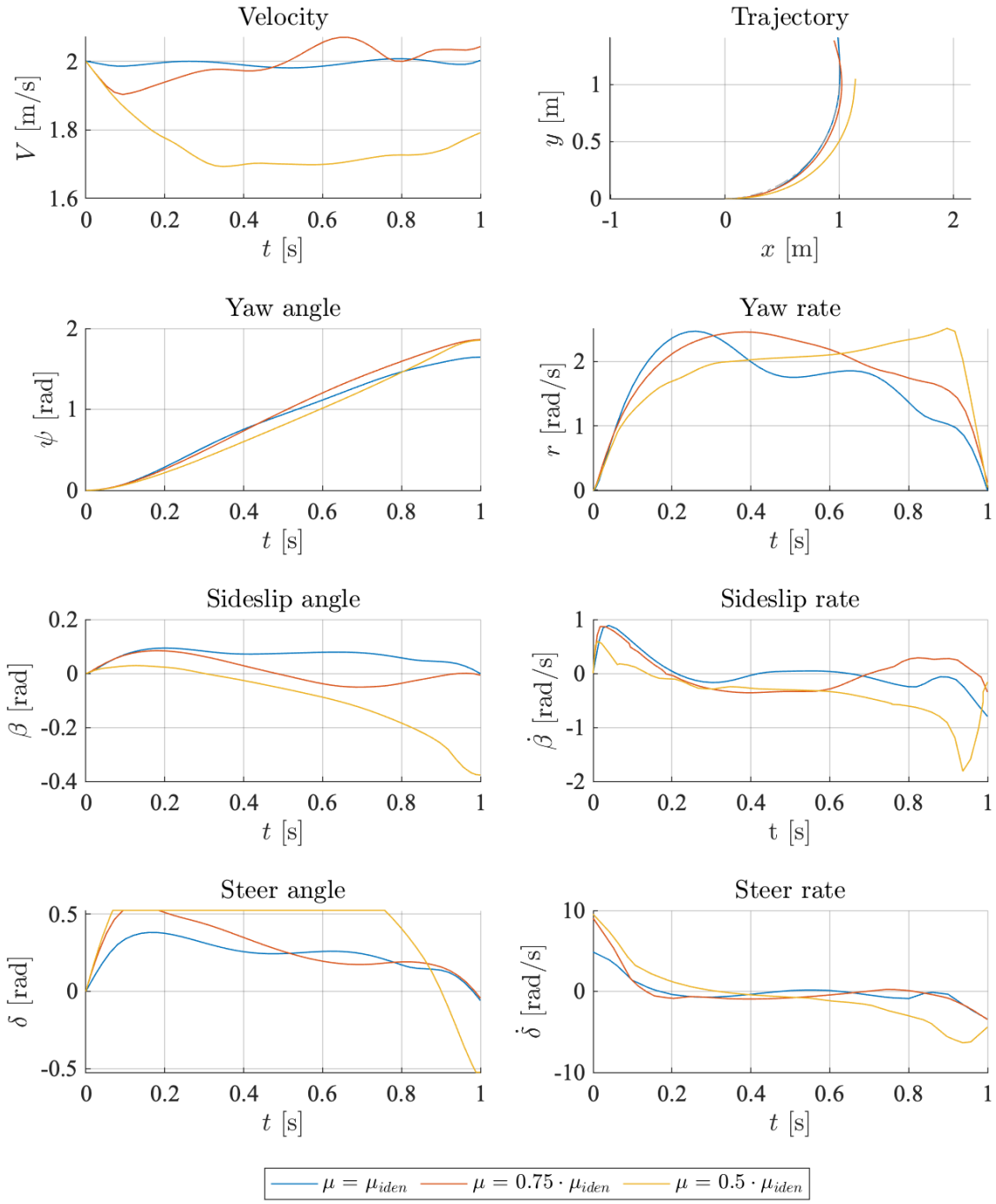

Figure F-3: Overview of the time domain responses describing the vehicle dynamics resulting from the trajectory optimization under varying friction coefficients.

F-4 Variation of the Friction Coefficient - Tire Dynamics

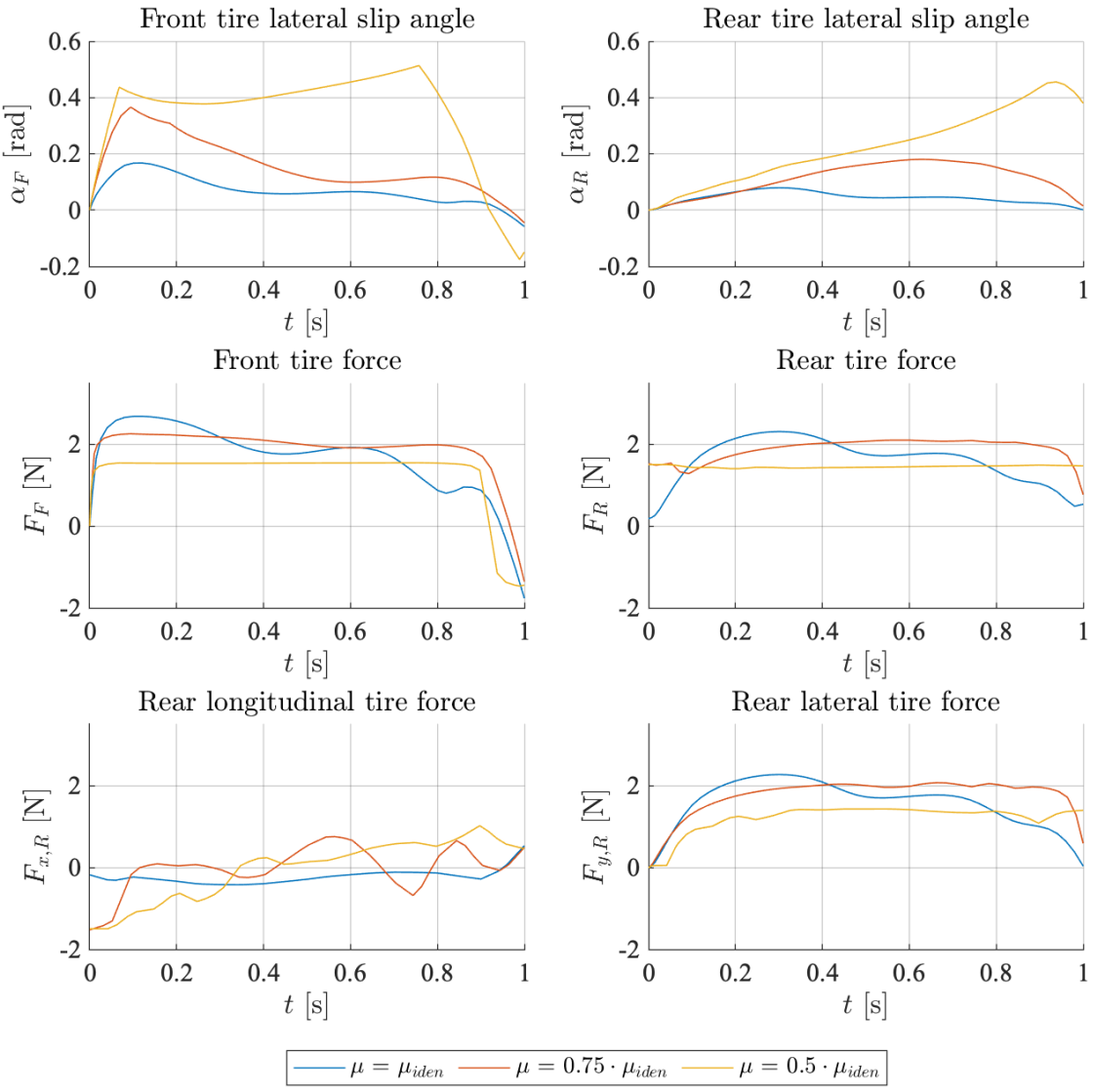

Figure F-4: Overview of the time domain responses describing the tire dynamics resulting from the trajectory optimization under varying friction coefficients.

F-5 Variation of the Cost-Function - Vehicle Dynamics

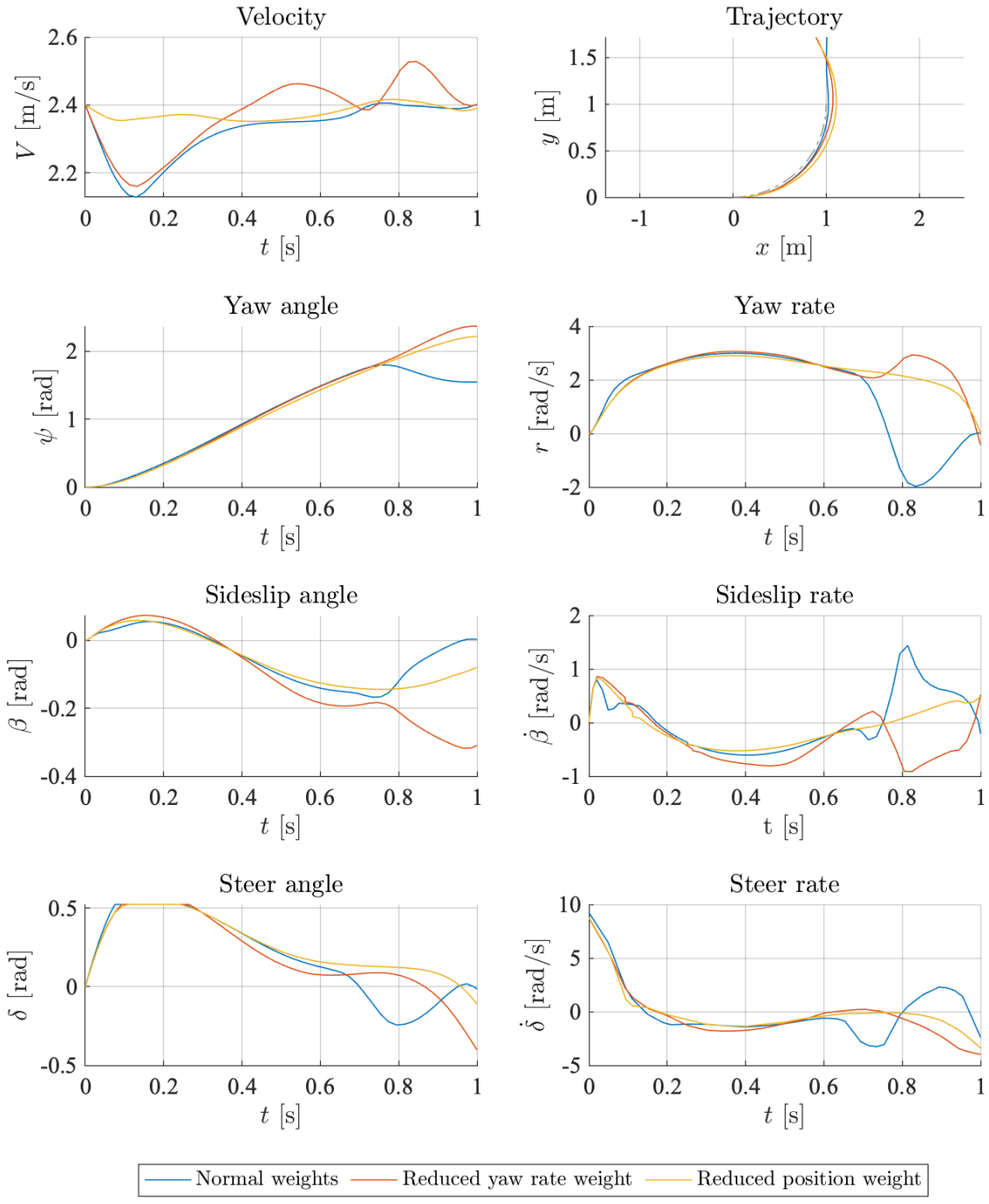

Figure F-5: Overview of the time domain responses describing the vehicle dynamics resulting from the trajectory optimization under varying cost-function weights.

F-6 Variation of the Cost-Function - Tire Dynamics

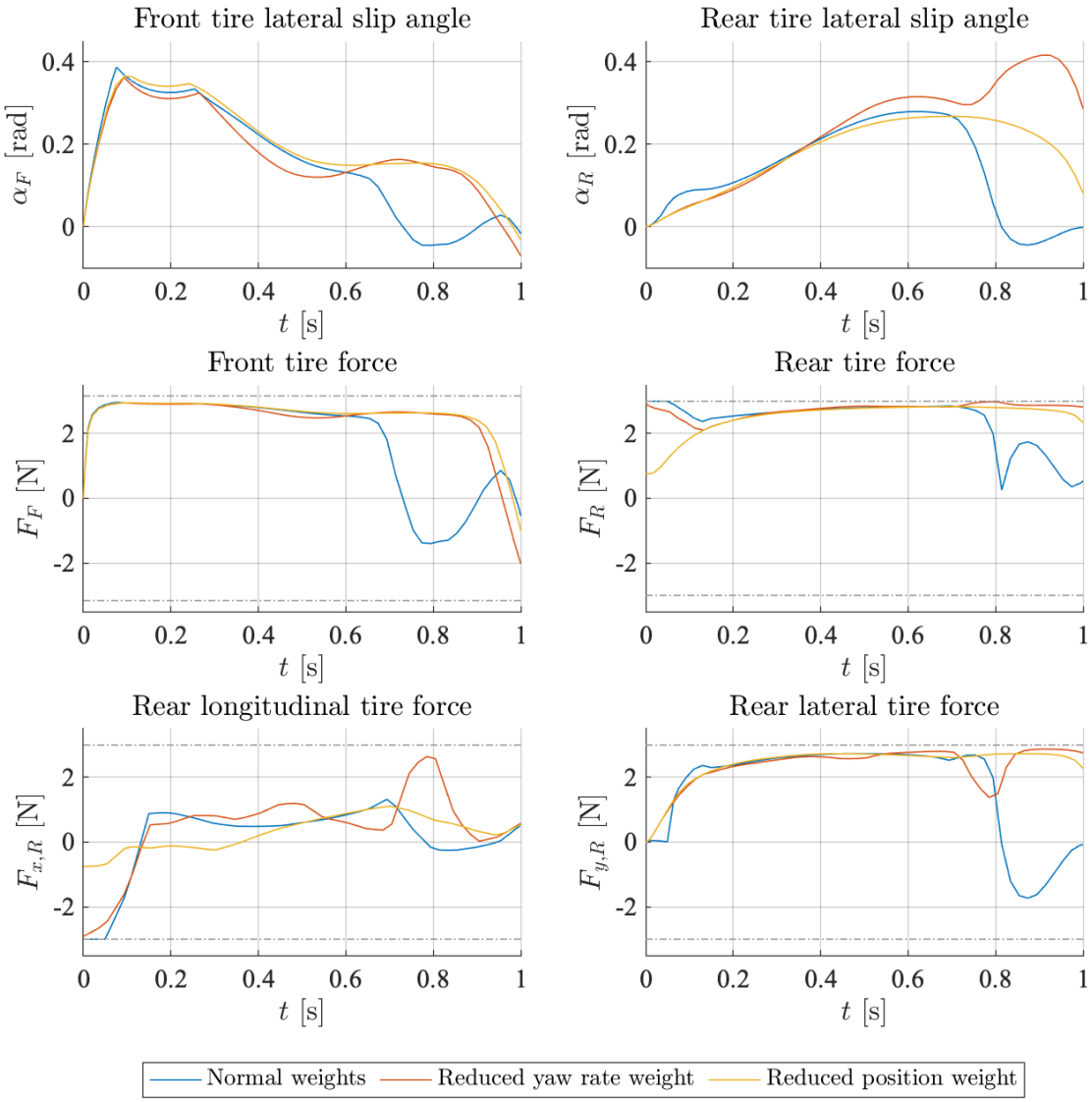

Figure F-6: Overview of the time domain responses describing the tire dynamics resulting from the trajectory optimization under varying cost-function weights.

F-7 Variation of the Cost-Function - Cost-Function Terms

Table F-1: Cost-function terms resulting from the model-based optimization with modified cost-functions.

Cost-Function structure	$\mathbf{J_{pos}}$	$\mathbf{J_V}$	$\mathbf{J}_r$	$\mathbf{J}_{\dot{\beta}}$
Normal weights	0.0084	0.2463	0.0000	0.0002
Reduced yaw rate weight	0.0489	0.2206	0.1802	0.0010
Reduced position weight	0.1068	0.0196	0.0006	0.0011

F-8 Verification of the Small Steering Assumption - Vehicle Dynamics

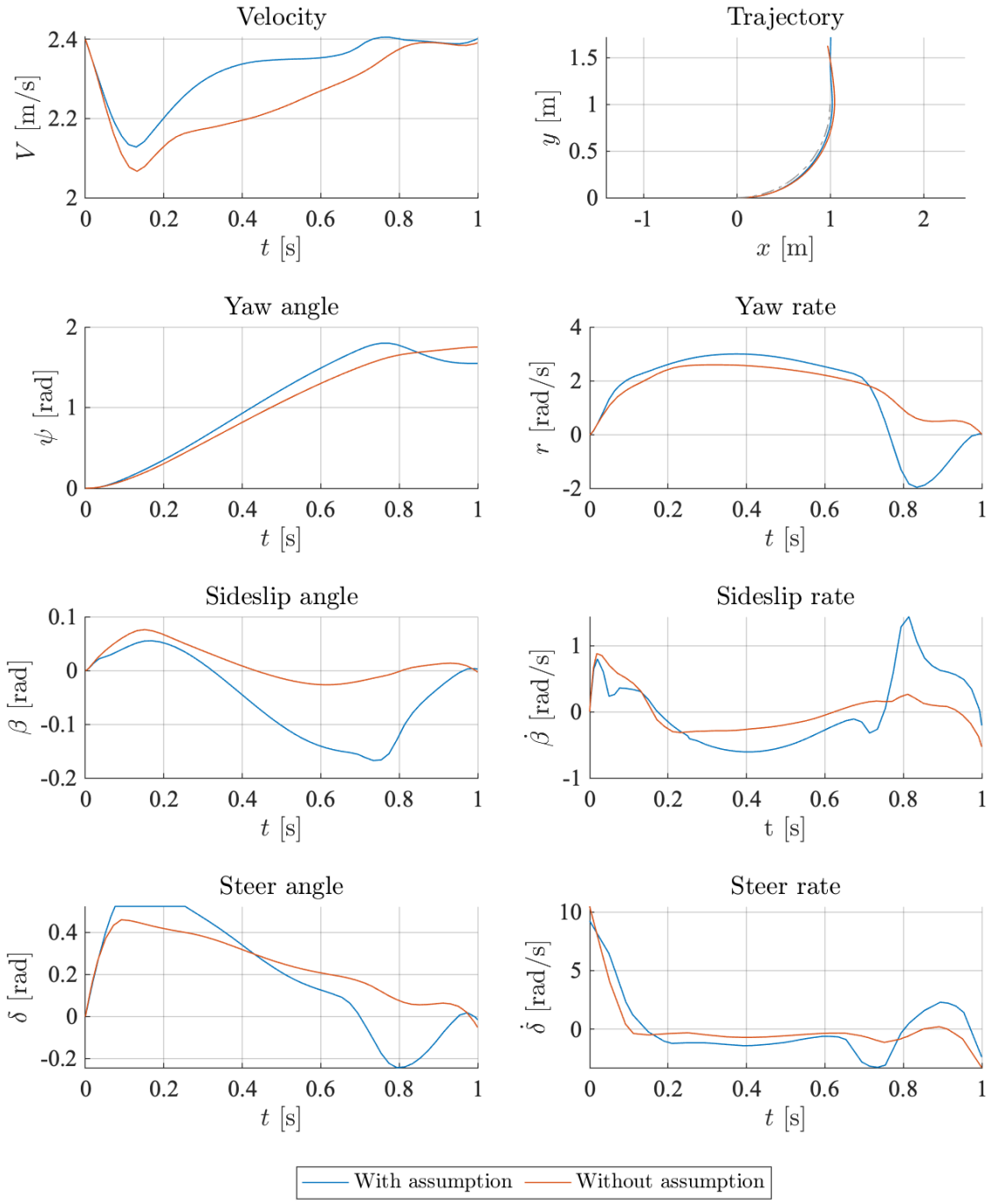

Figure F-7: Overview of the time domain responses describing the vehicle dynamics resulting from the trajectory optimization with and without the assumption of small steer angles.

F-9 Verification of the Small Steering Assumption - Tire Dynamics

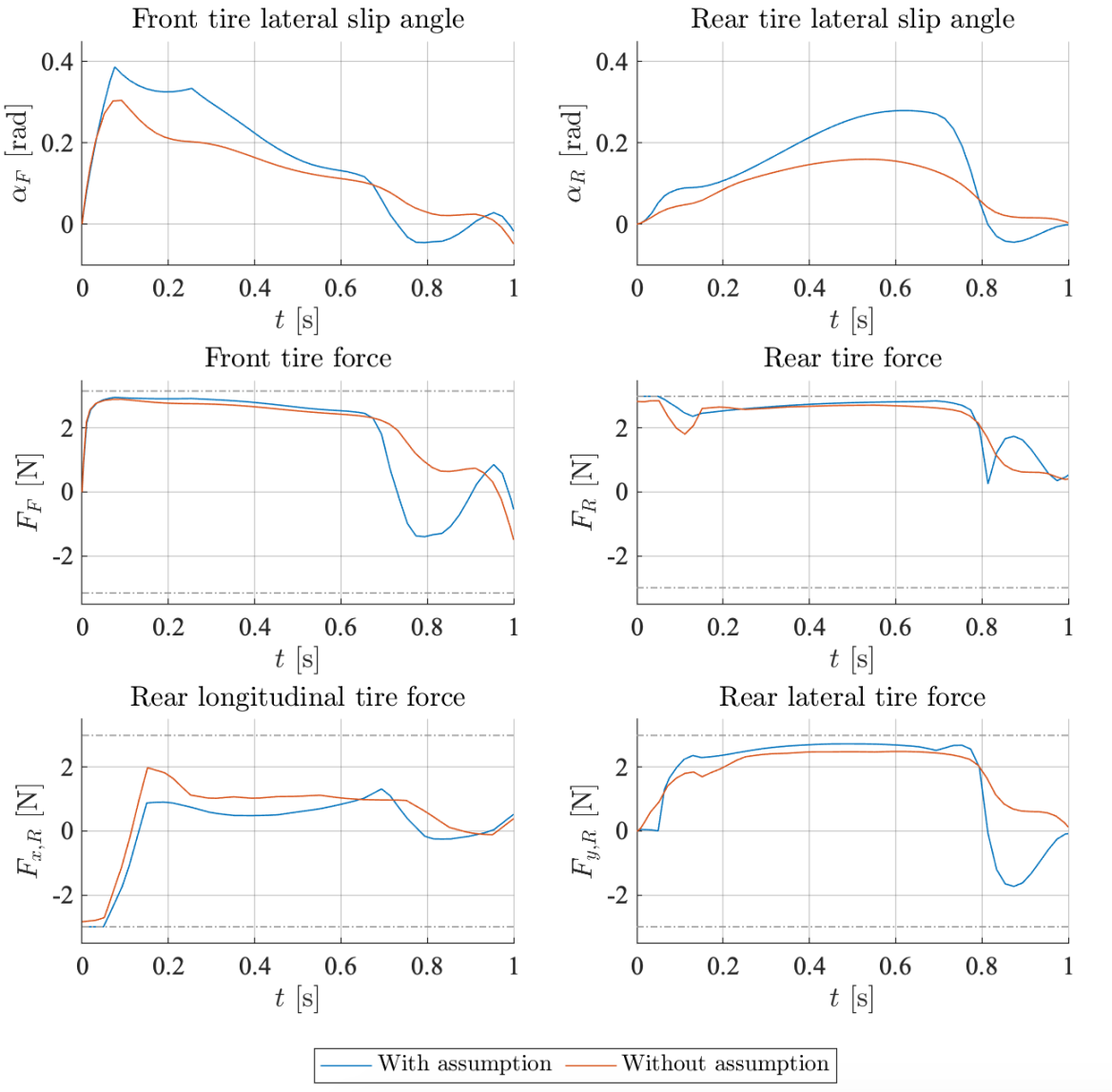

Figure F-8: Overview of the time domain responses describing the tire dynamics resulting from the trajectory optimization with and without the assumption of small steer angles.

F-10 Verification of the Small Steering Assumption - Cost-Function Terms

Table F-2: Cost-function terms resulting from the model-based optimization with and without the assumption of small steer angles.

Scenario	$\mathbf{J_{pos}}$	$\mathbf{J_V}$	$\mathbf{J}_r$	$\mathbf{J}_{\dot{\beta}}$
With assumption	0.0084	0.2463	0.0000	0.0002
Without assumption	0.0237	0.6229	0.0000	0.0239

Bibliography

[1] M. Abe. *Vehicle Handling Dynamics; Theory and Application*. Elsevier Ltd, Kanagawa, second edition, 2015.

[2] M. Acosta. Research on Multi-Actuated Agile Electric Vehicles : A Drift-based approach to Last-Moment Accident Avoidance Manoeuvres on Loose. Technical report, Coventry University, 2017.

[3] M. Acosta, S. Kanarachos, and M. Blundell. Vehicle agile maneuvering: From rally drivers to a finite state machine approach. *2016 IEEE Symposium Series on Computational Intelligence, SSCI 2016*, (December), 2017.

[4] M. Acosta, S. Kanarachos, and M. E. Fitzpatrick. A Hybrid Hierarchical Rally Driver Model for Autonomous Vehicle Agile Maneuvering on Loose Surfaces. In *Proceedings of the 14th International Conference on Informatics in Control, Automation and Robotics*, pages 216–225. SCITEPRESS - Science and Technology Publications, 2017.

[5] A. Al Jawahiri. *Spline-based Trajectory Generation for Autonomous Truck-Trailer Vehicles in Low Speed Highway Scenarios*. PhD thesis, Delft University of Technology, 2018.

[6] A. Babaei and A. Karimi. Optimal Trajectory-Planning of UAVs via B-Splines and Disjunctive Programming. pages 1–12, jul 2018.

[7] A. Bhoraskar and P. Sakthivel. A review and a comparison of Dugoff and modified Dugoff formula with Magic formula. In *2017 International Conference on Nascent Technologies in Engineering (ICNTE)*, number 1, pages 1–4. IEEE, jan 2017.

[8] M. Bian, L. Chen, Y. Luo, and K. Li. A Dynamic Model for Tire/Road Friction Estimation under Combined Longitudinal/Lateral Slip Situation. (2016), 2014.

[9] Y. Bouktir, M. Haddad, and T. Chettibi. Trajectory planning for a quadrotor helicopter. *2008 Mediterranean Conference on Control and Automation - Conference Proceedings, MED'08*, pages 1258–1263, 2008.

[10] H. Dugoff, P. S. Fancher, and L. Segel. Tire perfomance characteristics affecting vehicle response to steering and braking control inputs: final report. *Highway Safety Research Institute,University of Michigan*, 460, 1969.

[11] H. Dugoff, P. S. Fancher, and L. Segel. An Analysis of Tire Traction Properties and Their Influence on Vehicle Dynamic Performance. feb 1970.

[12] J. Edelmann and M. Plöchl. Handling characteristics and stability of the steady-state powerslide motion of an automobile. *Regular and Chaotic Dynamics*, 14(6):682–692, dec 2009.

[13] A. Erke. Effects of electronic stability control (ESC) on accidents: A review of empirical evidence. *Accident Analysis and Prevention*, 40(1):167–173, 2008.

[14] R. Fletcher. *Practical Methods of Optimization*. 2000.

[15] P. E. Gill, W. Murray, and M. H. Wright. *Practical Optimization*. 1997.

[16] F. Glover. A template for scatter search and path relinking. *Lecture Notes in Computer Science (including subseries Lecture Notes in Artificial Intelligence and Lecture Notes in Bioinformatics)*, 1363(February 1998):3–51, 1998.

[17] J. Gonzales, F. Zhang, K. Li, and F. Borrelli. Autonomous Drifting with Onboard Sensors. *Advanced Vehicle Control AVEC'16*, pages 3–8, 2016.

[18] S. Han. A Globally Convergent Method for Nonlinear Programming. *Journal of Global Optimization*, 8(2):189–199, 1996.

[19] R. Y. Hindiyeh and J. Christian Gerdes. A Controller Framework for Autonomous Drifting: Design, Stability, and Experimental Validation. *Journal of Dynamic Systems, Measurement, and Control*, 136(5):1–9, jul 2014.

[20] R. Y. Hindiyeh and J. C. Gerdes. Equilibrium Analysis of Drifting Vehicles for Control Design. In *Proceedings of the ASME 2009 Dynamic Systems and Control Conference*, pages 181–188. ASME, 2009.

[21] R. Lenain, M. Deremetz, J. B. Braconnier, B. Thuilot, and V. Rousseau. Robust sideslip angles observer for accurate off-road path tracking control. *Advanced Robotics*, 31(9):453–467, 2017.

[22] R. Lenain, B. Thuilot, C. Cariou, N. Bouton, and M. Berducat. Off-road mobile robots control: An accurate and stable adaptive approach. *2nd International Conference on Communications Computing and Control Applications, CCCA 2012*, pages 1–6, 2012.

[23] M. B. Milam. Real-time optimal trajectory generation for constrained dynamical systems. 2003:161, 2003.

[24] R. M. Murray, Z. Li, and S. S. Sastry. *A Mathematical Introduction to Robotic Manipulation*, volume 29. 1994.

[25] S. K. Nagar and S. K. Singh. An algorithmic approach for system decomposition and balanced realized model reduction. *Journal of the Franklin Institute*, 341(7):615–630, 2004.

[26] P. Nguyen and E. Case. Tire Friction Models and their Effect on Simulated Vehicle Dynamics. *Proceedings of a Symposium on Commercial Vehicle Braking and Handling*, 5(7):245–312, 1975.

[27] H. Pacejka. *Tyre and Vehicle Dynamics*. Elsevier Ltd, Delft, third edition, 2012.

[28] M. J. D. Powell. A fast algorithm for nonlinearly constrained optimization calculations. pages 144–157, 1978.

[29] R. Rajamani. *Vehicle Dynamics and Control*. Springer, second edition, 2012.

[30] SAE International. Taxonomy and Definitions for Terms Related to Driving Automation Systems for On-Road Motor Vehicles, 2014.

[31] C. Sprunk. Planning motion trajectories for mobile robots using splines. *University of Freiburg*, (October), 2008.

[32] E. Stella, C. L. Ladera, and G. Donoso. A very accurate method to approximate discontinuous functions with a finite number of discontinuities. pages 1–27, jan 2016.

[33] J. Svendenius. *Tire Modeling and Friction Estimation*. PhD thesis, Lund University, 2007.

[34] D. Tavernini, M. Massaro, E. Velenis, D. I. Katzourakis, and R. Lot. Minimum time cornering: The effect of road surface and car transmission layout. *Vehicle System Dynamics*, 51(10):1533–1547, 2013.

[35] Z. Ugray, L. Lasdon, J. Plummer, F. Glover, J. Kelly, and R. Marti. Scatter search and local NLP solvers: A multistart framework for global optimization. *INFORMS Journal on Computing*, 19(3):328–340, 2007.

[36] V. Usenko, L. von Stumberg, A. Pangercic, and D. Cremers. Real-time trajectory replanning for MAVs using uniform B-splines and a 3D circular buffer. In *2017 IEEE/RSJ International Conference on Intelligent Robots and Systems (IROS)*, pages 215–222. IEEE, sep 2017.

[37] R. Van Beelen. *Adaptive Observer for Automated Emergency Maneuvers Ruben van Beelen*. PhD thesis, Delft University of Technology.

[38] E. Velenis, D. Katzourakis, E. Frazzoli, P. Tsiotras, and R. Happee. Steady-state drifting stabilization of RWD vehicles. *Control Engineering Practice*, 19(11):1363–1376, nov 2011.

[39] E. Velenis and P. Tsiotras. Dynamic Tire Friction Models for Combined Longitudinal and Lateral Vehicle Motion. *Vehicle System Dynamics*, 43(1):3–29, 2003.

[40] E. Velenis and P. Tsiotras. Minimum Time vs Maximum Exit Velocity Path Optimization During Cornering. In *Proceedings of the IEEE International Symposium on Industrial Electronics, 2005. ISIE 2005.*, volume I, pages 355–360. IEEE, 2005.

[41] WHO. Global Status Report on Road Safety. Technical report, World Health Organization, Geneva, 2018.

[42] C. Wit and P. Tsiotras. Dynamic tire friction models for vehicle traction control. *Proceedings of the 38th IEEE Conference on Decision and Control (Cat. No.99CH36304)*, 4(December):3746–3751, 1999.

[43] K. Zhou, G. Salomon, and E. Wu. A new balanced realization and model reduction method for unstable systems. *IFAC Proceedings Volumes*, 32(2):1696–1701, 1999.

Glossary

List of Acronyms

SAE	Society of Automotive Engineers
ESC	Electronic Stability Control
COG	Center of Gravity
BARC	Berkeley Autonomous Race Car
RWD	Rear Wheel Drive
ESP	Electronic Stability Program
ADAS	Advanced Driver Assitance System
ABS	Anti-Lock Brakes
ESP	Electronic Stability Program
ACC	Active Cruise Control
IMU	Internal Measuring Unit
ECU	Electronic Control Unit
MCS	Motion Capture System
VAF	Variance Accounted For
RMSE	Root Mean Squared Error
SQP	Sequential Quadratic Programming

List of Symbols

α	Lateral slip angle
β	Side-slip angle
δ	Steering angle
$\dot{\psi},\ r$	Yaw rate
λ	Longitudinal wheel slip ratio
λ_i	i-th eigenvalue of the Controllability Grammian
λ_i	i-th eigenvector of the Controllability Grammian
μ	Friction coefficient
ω_x	Angular velocity around x-axis
ω_y	Angular velocity around y-axis
ω_z	Angular velocity around z-axis
ω_{wheel}	Angular wheel velocity
ϕ	Roll angle
ψ	Heading angle
τ	Spline time variable
$\mathbf{A}_{eq}$	Equality constraints matrix of the spline optimization
$\mathbf{A}_{ineq}$	Inequality constraints matrix of the spline optimization
$\mathbf{A}_{nleq}$	Nonlinear equality constraints matrix of the spline optimization
$\mathbf{e}_{\dot{\beta}}$	Error vector of the side-slip rate
$\mathbf{e}_{pos,spline}$	Error vector of the position in the spline optimization
$\mathbf{e}_{pos}$	Error vector of the position
$\mathbf{e}_r$	Error vector of the yaw rate
$\mathbf{e}_{V,spline}$	Error vector of the velocity in the spline optimization
$\mathbf{e}_V$	Error vector of the velocity
$\mathbf{P}_\delta$	Vector containing the spline control points of the steering angle
$\mathbf{P}_\psi$	Vector containing the spline control points of the heading angle
$\mathbf{P}_{F_{x,R}}$	Vector containing the spline control points of the rear longitudinal tire force
$\mathbf{P}_x$	Vector containing the spline control points of the inertial x location
$\mathbf{P}_y$	Vector containing the spline control points of the inertial y location
$\mathbf{W}_{\dot{\beta}}$	Weight of the side-slip rate error
$\mathbf{W}_{pos}$	Weight matrix of the position error
$\mathbf{W}_r$	Weight matrix of the yaw rate error
$\mathbf{W}_V$	Weight matrix of the velocity error
θ	Pitch angle
a_x	Longitudinal acceleration
a_y	Lateral acceleration
$C_k(\tau)$	k-th spline control point
C_α	Lateral tire stiffness

C_λ	Longitudinal tire stiffness
e_μ	Coefficient accounting for increased friction
$e_{coupled}$	Coefficient accounting for decreased coupling effect
F_x	Longitudinal tire force
F_y	Lateral tire force
F_z	Normal tire load
I_z	Mass moment of inertia
J	Cost-function
$J_{\dot{\beta}}$	Cost-function term of the side-slip rate
J_{pos}	Cost-function term of the position
J_r	Cost-function term of the yaw rate
J_V	Cost-function term of the velocity
L	Wheel base
l_F	Distance between the front axle and the Center of Gravity (COG)
l_R	Distance between the rear axle and the COG
m	Vehicle mass
M_z	Moment around the COG
P_i	i-th spline control point
$q_{\dot{\beta}}$	Weight on the side-slip rate cost-function term
q_{pos}	Weight on the position cost-function term
q_r	Weight on the yaw rate cost-function term
q_V	Weight on the velocity cost-function term
R	Cornering radius
r_{wheel}	Wheel radius
V	Cornering velocity
$V_x,\ u$	Longitudinal velocity
$V_y,\ v$	Lateral velocity
V_{enc}	Velocity obtained from wheel encoder
x	Longitudinal axis of the body-orientated reference frame
$x_{inertial}$	Horizontal axis of the inertial reference frame
y	Lateral axis of the body-orientated reference frame
$y_{inertial}$	Vertical axis of the inertial reference frame

Index